HYPERVELOCITY DISSOCIATING FLOW OVER A SPHERICALLY BLUNTED CONE

Thesis by
Kenji Togami

In Partial Fulfillment of the Requirements
for the Degree of
Aeronautical Engineer

California Institute of Technology
Pasadena, California

1993
(Submitted May 27, 1993)

To my wife and parents.

Acknowledgment

First of all, I want to express my best gratitude to my research advisor, Professor Hans G. Hornung, with his insight, encouragement and direction throughout the whole process of this work. Professor Bradford Sturtevant helped through his technical suggestions. Dr. Graham Candler of the University of Minnesota provided us the computation program, the know-how of the program and advice. Joe Haggerty and Larry Frazier helped me with the model fabrication with their patience and the sense of humor.

For the experiments in large facility, like T5, the help of the other members of the team is necessary. I would like to thank all T5 team members, Jacques Belanger, Eric Cummings, Patrick Germain, Bernard Rousset, Simon Sanderson and Bahram Valiferdowsi. Especially, I really appreciated Chih-Yung Wen for his advice for instrumentation and for discussions of experimental data.

My friends, office mates and the other fellow graduate students in GALCIT contributed very much and made this work more enjoyable.

My wife, Naoko, mentally encouraged me throughout this work. Without her hearty assistance and encouragement, this work could not be accomplished.

In the last, I would like to thank all my colleagues in Mitsubishi Heavy Industries in Japan who gave me very precious opportunity to do this work.

HYPERVELOCITY DISSOCIATING FLOW OVER A SPHERICALLY BLUNTED CONE

Kenji Togami
California Institute of Technology, 1993.

Recently several hypersonic vehicles are being developed in several countries. For the design of these vehicles, understanding the flow physics is necessary. Recently, the free piston driver for large shock tunnels became practical and it enables us to simulate the hypervelocity flow in the ground based facilities. Also the computing resources have grown dramatically and it enables us to compute the hypervelocity flow which is chemically and thermally nonequilibrium in a reasonable computation time. In this thesis the combined approach of experiment and computation has been applied to the hypervelocity flow on a spherically blunted cone.

The experiments are conducted in the newly developed free piston shock tunnel called T5 at the Graduate Aeronautical Laboratories, California Institute of Technology. Three kinds of the gases, nitrogen, air and carbon dioxide are used. The flow fields are computed by a CFD code using the two temperature model by Park. Since the flow field in the experiments is visualized with the differential interferogram, the computed density field is used to generate the differential interferogram. It can be concluded that the two temperature model CFD code can reproduce the basic flow feature such as the inflection point in the shock wave.

Heat transfer at the stagnation point is then examined. It correlates well with the equation by Fay and Riddell. Subsequently, the after body heat flux can be predicted by Lees' theory very well. The heat flux on after body is well correlated with Stanton number and local Reynolds number for each gas but the difference between the gases are significant. This is partly because the recombination plays a more important role in the after body flow. The results of the experiments and the computations points to the

necessity of other correlation parameters for the after body heat transfer in hypervelocity flows.

Then the difference between the shock tunnel experiment and actual flight was examined. The most dominant factor is the difference of free stream temperature. One method to estimate the heat flux in actual flight from experimental data was proposed and this method compensates the difference of the temperature. The result shows very good agreement with numerical computational results.

TABLE OF CONTENTS

LIST OF FIGURES

LIST OF TABLES

NOMENCLATURE

Roman Symbols

C	Coefficient for reaction constants in IDG, see eq. (2.9).
C_f	Coefficient for forward reaction constants.
c	Specific heat of the thermocouples.
c_s	Mass concentration of species s.
e	Electromotive force of the thermocouple.
D_{12}	Binary diffusion coefficient.
E	Total energy.
E_V	Vibrational-electronic excitation energy.
F	Flux in conservative equation (4.5) in x-direction , see also eq. (4.7).
F	Intensity function of object beam in interferogram, see eq. (4.21).
G	Flux in conservative equation (4.5) in y-direction , see also eq. (4.8).
h	Enthalpy.
h_0	Stagnation enthalpy.
$h_{0,i}$	Heat of formation of species s.
k	Boltzmann constant.
k	Thermal conductivity of the thermocouples, see eq. (3.2).
Le	Lewis number.
M	Mach number.
M	Collision partner, see eq. (4.10) to (4.12).
m	Mass of atom.
N_{AV}	Avogadro number.
N_s	Number density of species s.
n	Index of normal direction to the surface, see eq. (4.13).
n	Refractive index.
n_0	Reference refractive index.
p	Pressure.
p_e	Electron pressure.
Pr	Prandtl number.
$\dot{q}$	Heat flux.
$\dot{q}_w$	Heat flux on the wall.

q_j	Translational -rotational heat conduction flux in j-direction.
$q_{v\text{-}e,j}$	Vibrational-electronic excitation heat conduction flux in j-direction.
Q	Integrated heat input.
r	Nose radius of blunted cone.
Re	Reynolds number.
St	Stanton number.
s	Distance from the stagnation point along surface.
t	Time.
T	Temperature.
u	Velocity.
u_{sj}	Velocity of species s in j-direction.
u_0	Velocity before normal shock.
v_{sj}	Diffusion velocity of species s in j-direction.
V	Volume of gas.
$\dot{w}_s$	Mass generation of chemical species s.
W	Source term vector.
x_j	Spatial coordinate in j direction.
Z_s	Charge number of species s.

Greek Symbols

α	Degree of dissociation.
δ	Dirac's delta function, see eq. (4.2).
γ_{eff}	Effective ratio of specific heat in shock layer.
γ_∞	Ratio of specific heat in free stream.
ϕ	Phase shift of object beam, see eq. (3.15).
κ	Thermal conductivity of the gas.
κ_s	Gladstone-Dale constant for chemical species s.
ρ	Density.
ρ	Averaged density of the thermocouples, see eq. (3.2).
ρ_d	Characteristic density for dissociation.
ρ_s	Density of chemical species s.
ρ_0	Density before normal shock.
η	Approximate exponent of temperature for reaction rates.
ηf	Exponent of temperature for reaction rates.

θ	Angle between free stream and radius vector from center of curvature of nose.
θc	Cone semiapex angle.
θd	Characteristic temperature of dissociation.
κ_s	Gladstone-Dale constant of species s in eq. (3.12).
λ	Wave length of beam.
μ	Viscosity.
τ	Stress tensor.

Subscript

d	Characteristic value for dissociation.
e	Value at the outer edge of boundary layer.
e	Value for electron, see eq. (4.2).
s	Value of chemical species s.
V	Value of vibrational and electronic excitation, see eq. (4.4).
w	Value at the wall.
0	Stagnation Value.
∞	Free stream condition.

CHAPTER 1

INTRODUCTION

1.1 Introduction

The term "hypervelocity" used in this thesis has a different definition from "hypersonic." The latter word means only that the velocity of flow is several times higher than the speed of sound. But the former word implies that not only the velocity is high compared to the speed of sound but also the stagnation enthalpy is high enough to produce chemical reactions, i.e., dissociation, and/or the excitation of the vibrational mode of gas molecules.

Recently, the R&D activities for the vehicles which cruise in the hypervelocity regime, such as NASP in the United States, HOPE (H-II Orbiting PlanE) in Japan and HERMES in Europe have become very active. Since these vehicles cruise in the hypervelocity regime, the research for hypervelocity flow is recognized to be important. Since all these vehicles have a part of blunted conical shape, the research of hypervelocity over blunted cone flow is essential for these projects.

The work presented in this thesis tries to examine some of the physics of the hypervelocity chemical nonequilibrium flow on the blunted cone.

1.2 Motivations and Scope

When the hypervelocity flow stagnates at the nose of the body, the temperature at the shock wave becomes high enough to produce gas dissociation and/or to excite the vibrational mode of gas molecules. In addition to this, the characteristic time scale of chemical reaction and that of flow become of the same order of magnitude. It implies that the flow becomes nonequilibrium. This nonequilibrium phenomenon happens in the

stagnation region and it can be clearly understood that the aerothermodynamic characteristics at the stagnation point strongly depend on this phenomenon. But it should be pointed out that this phenomenon has an influence on the after body characteristics such as heat flux distribution and pressure distribution. Because the flow particle near the body surface goes through the stagnation region and properties of the fluid particle (e.g., composition, ratio of specific heat) are not conservative any more i.e., it depends on the trajectory of the particle.

There are two approaches to examine the physics of hypervelocity flow. One is experimental approach and the other is computational approach. Since hypervelocity flow is very difficult to be produced in the ground testing facility before, most of the previous work was done in the so-called "cold" hypersonic wind tunnel. However, the practical use of a free piston shock tunnel like T5 enables us to do experiments in this regime. And the recent dramatic development of computer resources also makes it possible to compute hypervelocity flow around axisymmetric blunted body in reasonable computation time. A big merit of the computational approach is its ability to provide us with much detailed information of the flow physics that is not accessible by the experimental approach but, of course, the computational results should be carefully validated with experimental data. Therefore, the combination of experimental and computational work can be a very powerful tool for the study of the physics of the hypervelocity flow and for extending the previous researches.

There are two major topics presented in this thesis. One is to study the heat flux characteristics both at the stagnation point and on the after body. The real gas effects on the stagnation point heat flux are very closely related to the dissociation reaction, because the dissociation reaction rate is much higher than the recombination reaction rate. In this region, binary scaling with Stanton number is considered to work very well. But on the after body, the effect of the recombination reaction cannot be ignored. Therefore, it is very interesting and important to find a criterion for the binary scaling of the heat

flux study. The other subject of this thesis is the examination of the flow feature of real gas blunted cone flow e.g., shock shape, density profile and pressure distribution by using both experimental and computational flow visualization . For the study of these subjects, a spherically blunted cone was used because it can eliminate the end effect of the model. Therefore this can be considered as the natural extension of the work by Macrossan (1990). These two subjects have been studied by many researchers in perfect gas or "cold hypersonics" before and some experiments have also been done in the real gas conditions. Therefore, this thesis was intended to provide new data in the real gas condition to this subject by using a newly developed facility and computational study.

1.3 Previous Works

Many experimental studies of blunt body hypersonic flow have been done since the 1950s because blunt body is the most widely used shape for hypersonic vehicle to reduce the aerodynamic heating. Some of these works which were relevant to this thesis will be overviewed in this section.

There are two categories of flow in blunt body flow, one is spherical flow and the other is conical flow. One significant feature of the blunted cone flow is the existence of adjustment phenomenon from the spherical flow to the conical flow. Giese and Bergdolt (1953) studied this kind of flow for truncated cone by quantitative interferometric study. According to their result, the gas compressed at the bow shock flows with changing its direction and expanding. After turning the corner of the truncated cone, the gas over-expands and is finally "recompressed" to adjust to conical flow. Traugott (1962) examined the criterion for the existence of over-expansion for the perfect gas by using integral method computations. Traugott explained the reason of the shock inflection with the pressure distribution. Because of the wave from this recompression, the spherical shock wave changes its shape from convex to concave and converges to a conical shock. Nagamatsu et al. (1960) and Gai et al. (1984) pointed out the existence of an inflection

point in the shock shape in the real gas experiment. Nagamatsu et al.(1960) summarized the result from the ordinary reflected shock tunnel. He used sphere and blunted cone as model shapes. He discussed the shock shape and the pressure distribution for various total temperatures. He also mentioned the existence of the shock inflection point in the blunted cone flow. But the total temperature and the density were not high enough to produce chemical nonequilibrium phenomena because of the limitation of the facility. Therefore the difference between nearly perfect gas flow and chemically reacting flow was not so significant. Hornung (1972 and 1976) studied the flow feature of blunted body flow in dissociating gas. Hornung proposed a new correlation between reaction parameter and shock detachment distance. And he also mentioned the dominance of the dissociating reaction over the recombination reaction near the stagnation point. From the practical point of view, this phenomenon is closely related to the pressure distribution, especially to the location of the center of pressure. The shift of the center of pressure in real gas flow is well known from the experience of the space shuttle orbiter flights. Stalker (1989) proposed an approximate method to evaluate this shift by using ideal dissociating gas. Flow feature at after body of blunted body is discussed by Macrossan and Stalker (1987) (see also Macrossan (1990)). They chose a blunted flat plate for their model.

Many works about aerodynamic heating in hypersonics have been also done because this is one of the major problems for the hypersonic cruise. For the stagnation point heat transfer, Fay and Riddell (1958) summarized the correlation for symmetric diatomic dissociating gas. This is the most well-known correlation for the stagnation point heat transfer in the hypersonic dissociating gas. Lees (1956) outlined the theoretical study of the laminar heat transfer of the blunted cone and sphere in hypersonic speed based on the self-similar solution of hypersonic boundary layers. In the 1980's, Koppenwallner (1984) summarized the several sets of the stagnation point heat transfer data over the hemisphere-cylinder in high Mach number flows. He also provided the heat

flux distribution downstream of the stagnation point. For the heat transfer on after body flow, Muylaert et al. (1992) summarized the data from ground testing, computation and flight experiment. They also mentioned a scaling law of heat transfer at stagnation point and after body.

CHAPTER 2

THEORETICAL STUDY

2.1 Introduction

Lighthill (1957) proposed a simplified model for the study of dynamics of dissociating symmetric diatomic gas that is known as ideal dissociating gas (IDG). In this chapter, the outline of this model is summarized. Two heat flux correlations will be presented, one proposed by Lees (1956) and the other by Fay and Riddell (1958). These theoretical models will be used in the later chapters for correlating the experimental results.

2.2 Law of Mass Action for Equilibrium IDG

For simplicity, let us consider following dissociation-recombination reaction

$$A_2 + M \leftrightarrow 2A + M. \tag{2.1}$$

M is a collision partner that is not changed in the reaction and it may be A_2 or A. According to Lighthill, the law of mass action for the chemical reaction (2.1) can be written to a good approximation as

$$\frac{\alpha^2}{1-\alpha} = \frac{\rho_d}{\rho} e^{-\frac{\Theta_d}{T}} . \tag{2.2}$$

For nitrogen in the temperature range from 1000 K to 7000 K, ρ_d is approximately 130 g/cm^3.

2.3 Nonequilibrium Model for IDG

When the state of the gas is not in equilibrium, the reaction rate, $\frac{d\alpha}{dt}$, is needed in order to obtain flow conditions. Since the reaction is represented by (2.1), the reaction rate can be expressed as

$$\frac{d\alpha}{dt} = \left(\frac{d\alpha}{dt}\right)_d + \left(\frac{d\alpha}{dt}\right)_r, \tag{2.3}$$

where first term is the contribution from the forward reaction (dissociation) and the second term from recombination. From the results of kinetic theory by using hard-sphere model, the reaction rate for dissociation can be written as

$$\left(\frac{d\alpha}{dt}\right)_d = C_f T^{\eta_f} e^{-\theta_d/T} (1-\alpha) \frac{n_M}{V N_{AV}}. \tag{2.4}$$

If the flow is in equilibrium, dα/dt is zero. Therefore, in equilibrium flow, the reaction rate for recombination is

$$\left(\frac{d\alpha}{dt}\right)_{r,eq} = -\left(\frac{d\alpha}{dt}\right)_{d,eq} = -C_f T^{\eta_f} e^{-\theta_d/T} (1-\alpha) \frac{n_M}{V N_{AV}}. \tag{2.5}$$

Substituting eq. (2.2) into eq. (2.5)

$$\left(\frac{d\alpha}{dt}\right)_{r,eq} = -\alpha^2 C_f T^{\eta_f} \frac{\rho}{\rho_d} \frac{n_M}{V N_{AV}}. \tag{2.6}$$

Eq. (2.6) is derived based on the equilibrium condition, but we assume that this result can be applied to the nonequilibrium state. Then, substitute (2.4) and (2.6) into (2.3) to obtain

$$\frac{d\alpha}{dt} = C_f \rho T^{\eta_f} \left\{ (1-\alpha) e^{-\theta_d/T} - \frac{\rho}{\rho_d} \alpha^2 \right\} \frac{n_M}{V N_{AV}} . \tag{2.7}$$

Since M may be A or A_2, this equation (2.7) should be summed up for all M and it becomes

$$\frac{d\alpha}{dt} = \rho \cdot \left[\frac{1}{M} \left\{ C_{f,A} \rho T^{\eta_{f,A}} \alpha + C_{f,A_2} \rho T^{\eta_{f,A_2}} \frac{1-\alpha}{2} \right\} \right] \times \left\{ (1-\alpha) e^{-\theta_d/T} - \frac{\rho}{\rho_d} \alpha^2 \right\} . \tag{2.8}$$

Freeman (1958) made an approximation for the value of the bracket in eq. (2.8) which finally yields

$$\frac{d\alpha}{dt} = C \rho T^{\eta} \left\{ (1-\alpha) e^{-\theta_d/T} - \frac{\rho}{\rho_d} \alpha^2 \right\} . \tag{2.9}$$

Equations (2.2) and (2.9) are required to account for the equilibrium and nonequilibrium behavior of the gas.

2.4 Normal shock in IDG

The normal shock relation in IDG can be calculated by solving the following equation set.

Mass conservation

$$\rho_0 u_0 = \rho u \tag{2.10}$$

Momentum conservation

$$\rho_0 u_0^2 = \rho u^2 \tag{2.11}$$

Total enthalpy conservation

$$h_0 = h + \frac{u^2}{2} \tag{2.12}$$

Thermal equation of state

$$p = \frac{k}{2m} \rho T (1+\alpha) \tag{2.13}$$

Caloric equation of state

$$h = \frac{k}{2m} \{(4+\alpha) T + \alpha \theta_d\} \tag{2.14}$$

Law of mass action (equilibrium flow)

$$\frac{\alpha^2}{1-\alpha} = \frac{\rho_d}{\rho} e^{-\frac{\Theta_d}{T}} \tag{2.2}$$

or (nonequilibrium flow)

$$\frac{d\alpha}{dt} = C\rho T^{\eta} \left\{ (1-\alpha) e^{-\theta_d/T} - \frac{\rho}{\rho_d} \alpha^2 \right\} \tag{2.9}$$

2.5 Lees Heat Flux Correlation for Blunted Cone

Lees (1956) studied laminar heat transfer over a blunted cone based on hypersonic boundary layer self similar solutions. According to his result, the stagnation point heat flux is given by

$$\dot{q}_w(0) = \frac{0.5 \times 2^{k/2} \, \mathrm{Pr}^{-2/3} \sqrt{(\rho_e \mu_e)_0} \sqrt{u_\infty} \, h_0 \, G(M_\infty, \gamma_{eff}, \gamma_\infty)}{\sqrt{r}}, \tag{2.15}$$

where

$$G(M_\infty, \gamma_{eff}, \gamma_\infty) = \left\{ \left(\frac{\gamma_{eff} - 1}{\gamma_{eff}} \right) \left(1 + \frac{2}{\gamma_\infty - 1} \frac{1}{M_\infty^{\,2}} \right) \left(1 - \frac{1}{\gamma_\infty M_\infty^{\,2}} \right) \right\}^{1/4}. \tag{2.16}$$

On the spherical part, the heat flux is given by

$$\frac{\dot{q}_w(\theta)}{\dot{q}_w(0)} = \frac{2\theta\sin\theta\left\{\left(1-\frac{1}{\gamma_\infty M_\infty{}^2}\right)\cos^2\theta+\left(\frac{1}{\gamma_\infty M_\infty{}^2}\right)\right\}}{\sqrt{D(\theta)}} \tag{2.17}$$

where

$$D(\theta) = \left(1-\frac{1}{\gamma_\infty M_\infty{}^2}\right)\left(\theta^2 - \frac{\theta\sin 4\theta}{2} + \frac{1-\cos 4\theta}{8}\right) + \frac{4}{\gamma_\infty M_\infty{}^2}\left(\theta^2 - \theta\sin 2\theta + \frac{1-\cos 2\theta}{2}\right) \tag{2.18}$$

The heat flux on the cone part can be computed with the following equations.

$$\frac{\dot{q}_w(s)}{\dot{q}_w(0)} = A(\theta_c)\frac{s'/r}{\left\{B(\theta_c)+(s'/r)^3\right\}^{1/2}} \tag{2.19}$$

where

$$\begin{cases} \dfrac{s'}{r} = \cot\theta_c + \left\{\dfrac{s}{r} - \left(\dfrac{\pi}{2}-\theta_c\right)\right\} \\ A(\theta_c) = \dfrac{\sqrt{3}}{2}\left\{\left(1-\dfrac{1}{\gamma_\infty M_\infty{}^2}\right)\sin^2\theta_c + \dfrac{1}{\gamma_\infty M_\infty{}^2}\right\}^{1/2}\sqrt{\dfrac{\pi}{2}-\theta_c} \\ B(\theta_c) = \dfrac{3}{16\sin^2\theta_c\left\{\left(1-\dfrac{1}{\gamma_\infty M_\infty{}^2}\right)\sin^2\theta_c + \dfrac{1}{\gamma_\infty M_\infty{}^2}\right\}} \\ \qquad \times\left[\dfrac{D(\theta)}{\theta}\right]_{\theta=\frac{\pi}{2}-\theta_c} - \cot^3\theta_c \end{cases} \tag{2.20}$$

2.6 Fay and Riddell Stagnation Point Heat Flux Correlation

Fay and Riddell (1958) proposed a correlation for stagnation point heat flux in dissociated air. This correlation is most widely used for the prediction of stagnation heat flux. For the equilibrium boundary layer, the correlation is

$$\dot{q}_w = 0.76\,\mathrm{Pr}^{-0.6}\left(\rho_w \mu_w\right)^{0.1}\left(\rho_e \mu_e\right)^{0.4}\left\{1+\left(Le^{0.52}-1\right)\frac{h_D}{h_0}\right\}\left(h_0 - h_w\right)\sqrt{\left(\frac{du_e}{dx}\right)_0} \qquad (2.21)$$

and for the frozen boundary layer with noncatalytic wall, it is

$$\dot{q}_w = 0.76\,\mathrm{Pr}^{-0.6}\left(\rho_w \mu_w\right)^{0.1}\left(\rho_e \mu_e\right)^{0.4}\left(h_0 - h_w\right)\sqrt{\left(\frac{du_e}{dx}\right)_0} \qquad (2.22)$$

From modified Newtonian theory, the velocity gradient at the stagnation point is given by

$$\left(\frac{du_e}{dx}\right)_0 = \frac{1}{r}\sqrt{\frac{2(\rho_e - \rho_\infty)}{\rho_e}} \qquad (2.23)$$

and h_D in eq. (2.21) is defined as

$$h_D = -\sum_s c_s\, h_{0,s}. \qquad (2.24)$$

The values of h_D for several species are summarized in table B.1 in Appendix B.

CHAPTER 3

EXPERIMENTAL METHOD

3.1 Introduction

The wind tunnel used is T5 hypervelocity free piston shock tunnel. This kind of shock tunnel uses adiabatic compression of the driver gas to get the high shock speed in the shock tube which implies high enthalpy flow can be obtained in the test section. This shock tunnel is instrumented with pressure transducers to get the primary operating data. Differential interferometry is used to visualize the flow field. The wind tunnel model used for this experiment was a spherically blunted cone instrumented with seven thermocouple heat flux sensors and seven pressure transducers.

3.2 T5 Free Piston Shock Tunnel

T5 hypervelocity free piston shock tunnel was used for this research. The schematic of T5 shock tunnel is shown in figure 3.1 and primary dimensions of this tunnel are summarized in table 3.1. The secondary reservoir is filled with high pressure air to accelerate the piston loaded in the end of the compression tube. Monatomic gas mixtures are used as driver gas, the test gas is filled into the shock tube and the test section is evacuated. The compression tube and the shock tube are divided by the primary diaphragm. The shock tube and test section are divided by the secondary diaphragm. An operating diagram of the free piston shock tunnel is shown in figure 3.2 (from Belanger (1993)). One unique feature of this type of shock tunnel is that it has a free piston in the compression tube. Its velocity reaches up to about 300 m/s and it compresses the driver gas almost adiabatically. This heats and compresses the driver gas to high temperature and high pressure. Because inert gases are used in the compression

tube, there is no dissociation which would absorb heat. Therefore high temperature and high pressure driver gas can be attained efficiently. The primary diaphragm is made of stainless steel and typical burst pressures are 50 to 90 MPa. The diaphragm has two grooves which cross normal to each other (for more detail, see Cummings (1993)). This groove configuration can maintain the burst pressure fairly constant and it produces very little debris at the test section. The typical shock speed is about 2 km/s to 5 km/s and the shock wave is reflected at the end of the shock tube. High enthalpy and high pressure gas is produced behind the shock and this gas expands through the nozzle. Typical flow duration time is 2 ms. A contoured nozzle is used for this experiment, and its expansion ratio is 100. The nozzle throat is made of molybdenum. This is because of the intense heat flux of magnitude of 1 GW/m^2. Characteristic quantities, velocity, temperature, density and others, can be obtained by numerical computation from the measured reservoir conditions. The performance in the shock tube is computed based on the assumption of one-dimensional equilibrium flow with ESTC program (see Lordi et al. (1965)). The condition at the exit of the nozzle was calculated with quasi-one-dimensional characteristic method (see McIntosh (1971)). A more detailed description of the operation and performance of T5 is given by Hornung (1992).

Table 3.1 Primary Dimensions of T5

Max. Diaphragm Burst Pressure	130 MPa
Max. Secondary Reservoir Pressure	15 MPa
Compression Tube Diameter	300 mm
Compression Tube Length	30 m
Shock Tube Diameter	90 mm
Shock Tube Length	12 m
Nozzle Exit Diameter	314 mm
Piston Mass	120 kg

3.3 Instrumentation of the Wind Tunnel

The pressure history at the end of the compression tube, pressure history in the shock tube and nozzle reservoir pressure history were measured as the primary wind tunnel operating condition. The burst pressure of the diaphragm was determined from the pressure history at the end of compression tube. The pressure history of the shock tube was used for the calculation of averaged shock speed. Nozzle reservoir pressure was used for the computation of the nozzle flow computation. All the pressures were measured with piezoelectric pressure transducers made by PCB Piezotronics Inc. The specifications of the transducers are shown in table 3.2.

Table 3.2 Specification of Pressure Transducers for T5

Specifications : Model Number		119M44
Range	psi	80,000
Maximum Pressure	psi	100,000
Resolution	psi	1
Sensitivity (nominal)	pC/psi	0.25
Resonant Frequency	kHz	500
Rise Time	μs	1
Acceleration Sensitivity	psi/G	0.004
Vibration, Shock	G	10,000; 20,000

3.4 Wind Tunnel Model and its Instrumentation

The wind tunnel model is a spherically blunted cone with a semivertex angle of 35 degrees. The drawings of the model are presented in Appendix A. A photograph of the model is shown in figure 3.3. The model is made of steel. This model is instrumented with 7 pressure transducers and 7 thermocouple heat transfer gauges. The location of the sensors are listed in table 3.3.

Table 3.3 Location of the Sensors

Thermocouples			Pressure Transducers		
Ch. No.	s (mm)	θ (deg.)	Ch. No.	s (mm)	θ (deg.)
1	0.0	–	1	0.0	−180
2	31.4	0	2	31.4	−45
3	62.8	45	3	62.8	0
4	72.8	90	4	72.8	−135
5	82.8	135	5	82.8	−90
6	92.8	0	6	92.8	−45
7	102.8	45	7	102.8	0

s : Distance along the surface from the tip

θ : Angle around the symmetric axis looking from the top view

The heat flux gauges are coaxial thermocouples and made by MEDTHERM Corporation. Their specifications are summarized in table 3.4.

The pressure transducers were made by PCB Piezotronics Inc. and their specifications are summarized in table 3.5. The method of mounting the transducer is also shown in figure in Appendix A. Five transducers are mounted in the holders first and both of them are mounted in the model. The holder is screwed to the model by a nut with a plastic ring between holder and nut. There are also 2 o-rings to fix the holder and also to seal the air. With these rings, holder and transducer have no metal contact with the model and this is intended to reduce the noise from the vibration of the model. A Pitot probe was used to measure stagnation pressure.

For the visualization of the flow, differential interferometry was used. A frequency-doubled YAG laser was used as light source and its wave length is 532 nm.

Table 3.4 Specification of Thermocouples

Specifications : Model Number		TCS-E-10370
Type		K (Chromel-Constantan)
Range	K	78 - 1272
Response Time	μs	1
Sensing Surface Diameter	mm	1.55

Table 3.5 Specification of Pressure Transducers for Model

Specifications : Model Number		113A21
Range	psi	250
Maximum Pressure	psi	3000
Resolution	psi	0.01
Sensitivity (nominal)	mV/psi	20
Resonant Frequency	kHz	500
Rise Time	μs	1
Acceleration Sensitivity	psi/G	0.002
Vibration, Shock	G	2000, 20000

The nozzle recoils about 0.1 m upstream during the piston motion phase of the operation. Therefore, the model was positioned with its tip just at the nozzle exit before test. The model was set 1 inch below the centerline of the nozzle for better observation of the upper portion of the model by interferogram. The Pitot probe was set far enough below the model to avoid interference of the bow shock wave from the Pitot tip with the sensors of the model. The arrangement of the test section is shown in figure 3.4.

3.5 Experimental Conditions

The experimental conditions are summarized in table 3.6. Major parameters of these cases are reservoir enthalpy and reservoir pressure (nozzle reservoir stagnation pressure). Experiments are conducted at four reservoir enthalpies and three reservoir pressures. Expected stagnation enthalpy and nozzle reservoir stagnation pressure are shown in figure 3.5. Also three kinds of test gases were used, nitrogen, air and carbon dioxide. Nitrogen is for understanding the physics of flow because of its simple chemistry. The carbon dioxide was used because a larger fraction of energy is absorbed in dissociation in the carbon dioxide flow than in air flow or nitrogen flow so that more dramatic real gas effects occur, and also because higher Reynolds numbers can be obtained.

3.6 Data Handling

3.6.1 Data Acquisition

Experimental data was acquired through CAMAC analog digital interface by DSP Technology. At the time of the experiment, the data were digitized and loaded into the memory of total capacity 128 kbyte. And then the data in the memory was downloaded into the work station to be reduced. Each channel had 4 kbyte (4096 byte) length and sampling rate was 200 kHz. 1/8 of the total data length was pre-trigger data and the rest of it was post-trigger data.

The thermocouples were connected to amplifiers and then to digitizers. The output from the pressure transducer power supply was directly connected to the digitizers.

Table 3.6 Experimental Conditions

No.	Secondary Reservoir Pressure (MPa)	Driver Gas He + Ar (% He)	Driver Gas Pressure (kPa)	Primary Diaphragm Burst Pressure (MPa)	Test Gas Pressure (kPa)	Stagnation Enthalpy (MJ/kg)
1	4.61	100	145	32.5	40.0	11.6
2	7.82	95	116	90.0	50.0	16.8
3	7.89	100	116	90.0	40.0	21.6
4	7.89	85	116	90.0	85.0	10.1
5	11.48	95	143	115.	65.0	12.2
6	7.92	85	116	90.0	85.0	10.5
7	7.92	95	116	90.0	35	14.4

3.6.2 Method to Calculate Heat Flux

The outputs of the thermocouples were converted to temperature by the following equation which is valid for chromel-constantan thermocouples.

$$T(K) = Ae + Be^2 + Ce^3 + De^4 \tag{3.1}$$

where

$$\begin{cases} A = 1.7022525 \times 10^{-2} \\ B = -2.209724 \times 10^{-4} \\ C = 5.4809314 \times 10^{-6} \\ D = -5.7669892 \times 10^{-8} \end{cases}$$

The heat flux is calculated based on the one-dimensional semi-infinite slab heat conduction assumption. The heat flux into a homogeneous semi-infinite slab can be represented as

$$\dot{q}(t) = \sqrt{\frac{\rho c k}{\pi}} \int_0^t \frac{dT(\tau)}{d\tau} \frac{d\tau}{\sqrt{t-\tau}}. \tag{3.2}$$

The discretized form of equation (3.2) is written as

$$\dot{q}_n = 2\sqrt{\frac{\rho c k}{\pi}} \sum_{j=1}^{n} \frac{T_j - T_{j-1}}{\sqrt{t_n - t_j} + \sqrt{t_n - t_{j-1}}}. \tag{3.3}$$

This form is given by Schultz and Jones (1973) and this method is referred to as the direct method.

Another method to compute heat flux is called the indirect method. First, the integrated heat input Q(t) is computed from thermocouple output by the following equation

$$Q(t) = \sqrt{\frac{\rho c k}{\pi}} \int_0^t \frac{T(\tau)}{\sqrt{t-\tau}} d\tau. \tag{3.4}$$

Equation (3.4) can be discretized as follows.

$$Q_n = \sqrt{\frac{\rho c k}{\pi}} \sum_{j=1}^{n} \frac{T_j + T_{j-1}}{\sqrt{t_n - t_j} + \sqrt{t_n - t_{j-1}}} (t_n - t_{n-1}). \tag{3.5}$$

By differentiating eq. (3.5) with respect to time, the heat flux can be computed. The result is

$$\dot{q}_n \approx \frac{\Delta Q_n}{\Delta t} = \frac{-2Q_{n-8} - Q_{n-4} + Q_{n+4} + 2Q_{n+8}}{40(t_n - t_{n-1})}. \tag{3.6}$$

The direct method is more straightforward than the indirect method and does not require as much computing time. But the direct method amplifies the noise on the original thermocouple output more than the indirect method. Therefore, some filtering technique is required to remove any noise from the output of the thermocouple in the direct method. In the indirect method, it is unnecessary to filter the data explicitly. For this reason, the indirect method was used for this experiment.

The heat flux of each location of thermocouple was computed by taking the average at a certain time over a certain time width. The average was taken at time of 1 millisecond after the flow starts and the width is 0.5 millisecond. The value for $\sqrt{\rho c k}$ is 8918.6 J m^{-2} K^{-1} $s^{-0.5}$.

CHAPTER 4

NUMERICAL COMPUTATION

4.1 Introduction

Many details of the flow field, such as degree of dissociation, dissociation rate or boundary layer profile are not accessible during the experiment, but can be obtained by computation. By combining experiment and computation, a better understanding of the physics of the flow can be obtained. In this chapter, the basic physical considerations for the computation and the corresponding governing equations will be described. Since computational interferograms were generated for the verification of the numerical solution, the methodology for computational interferometry will also be covered.

4.2 Flow Field Computation

In this section, the outline of the computation method of the flow field will be summarized. The computer code was prepared and provided by Candler. The flow field computations were performed using a CRAY Y-MP in Jet Propulsion Laboratory (JPL) of California Institute of Technology. Post-processing of computed data was done by a SUN SPARC station. First, the equation set solved by the code is outlined and then, the boundary condition and computational grid will also be presented.

4.2.1 Basic Considerations and Governing Equations

There are several differences between the computational method of hypervelocity flow and that of supersonic perfect gas flow. One significant difference is in the energy equation. In some cases of hypervelocity flow, the flow becomes chemically and thermally nonequilibrium. Therefore, a chemical source term appears in the energy

conservation equation and in the case of thermally nonequilibrium flow, each temperature which describes the internal energy mode such as rotation, vibration or electronic excitation may be different from the other temperatures. Therefore the energy equation should be separated for each internal mode. But for the case that we have interest in, the translational mode and rotational mode are fully excited because the temperature which describes each energy state is much higher than the respective characteristic temperatures of each mode. For example, the rotational characteristic temperature is 2.86 K for nitrogen molecule. Thus, we can treat these two temperatures as equal. Park (1988, 1989) suggested a two temperature model for the hypervelocity flow in nitrogen and air. The translation and rotation temperature are the same and a different temperature describes vibration and electronic excitation . Therefore, two kinds of energy equation appear. One is the total energy equation the other is the vibration-electron energy equation. Vibration-electron energy may be different for different chemical species. But Candler et al. (1988) concluded that we can consider that the vibrational temperature is the same even for different species. Based on the argument above, the governing equations for flow field computation are summarized below.

One species conservation equation is needed for each of the n chemical species.

$$\frac{\partial \rho_s}{\partial t} + \frac{\partial}{\partial x_j}(\rho_s u_{s\,j}) = -\frac{\partial}{\partial x_j}(\rho_s v_{s\,j}) + \dot{w}_s \qquad (4.1)$$

There are d total momentum conservation equations, where d is the number of spatial dimensions.

$$\frac{\partial}{\partial t}(\rho u_i) + \frac{\partial}{\partial x_j}\left(\rho u_i u_j + p\,\delta_{ij}\right) = -\frac{\partial \tau_{ij}}{\partial x_j} - \sum_{s=1}^{n} Z_s \frac{\partial p_e}{\partial x_i}. \qquad (4.2)$$

One vibration-electron energy conservation equation is represented as

$$\frac{\partial E_V}{\partial t}+\frac{\partial}{\partial x_j}\left\{\left(E_V+p_e\right)u_j\right\}=-\frac{\partial}{\partial x_j}\left\{\left(E_V+p_e\right)v_j\right\}-\frac{\partial q_{V,j}}{\partial x_j}$$
$$-N_e\,e\,\tilde{E}_i\left(u_i+v_{e,i}\right)-\frac{\partial}{\partial x_j}\left\{\left(u_i+v_{e,i}\right)\tau_{e,ij}\right\}+Q_{T-e}+\sum_s\left(Q_{T-v_s}+Q_{v-v_s}+\dot{w}_s\,e_{v,s}\right)+\dot{w}_e\,e_e \tag{4.3}$$

Finally, one total energy conservation equation can be written as

$$\frac{\partial E}{\partial t}+\frac{\partial}{\partial x_j}\left((E+p)u_j\right)=-\frac{\partial}{\partial x_j}\left(q_j+q_{v-e,j}\right)-\frac{\partial}{\partial x_j}\left(u_i\,\tau_{ij}\right)$$
$$-\sum_{s=1}^{n}\frac{\partial}{\partial x_j}v_{sj}\,h_s-\sum_{s=1}^{n}\frac{N_s}{N_e}Z_s\frac{\partial p_e}{\partial x_i}u_i \tag{4.4}$$

These equations are then written in the conservative form

$$\frac{\partial U}{\partial t}+\frac{\partial F}{\partial x}+\frac{\partial G}{\partial y}=W, \tag{4.5}$$

where U is given by

$$U=\left(\rho_1,\rho_2,\cdots,\rho_n,\rho u,\rho v,E_{v-e},E\right)^T \tag{4.6}$$

and the flux of x-direction is

$$F = \begin{pmatrix} \rho_1(u+u_1) \\ \rho_2(u+u_2) \\ \vdots \\ \rho_n(u+u_n) \\ \rho u^2 + p + \tau_{xx} \\ \rho uv + \tau_{xy} \\ E_{v-e}\, u + q_{v-e,x} \\ (E+p+\tau_{xx})u + \tau_{xy}\, v + q_x + q_{v-e,x} + \sum_{s=1}^{n} \rho_s\, h_s\, v_s \end{pmatrix}. \qquad (4.7)$$

And, the flux for the y direction can be written as

$$G = \begin{pmatrix} \rho_1(v+v_1) \\ \rho_2(v+v_2) \\ \vdots \\ \rho_n(v+v_n) \\ \rho uv + \tau_{yx} \\ \rho v^2 + p + \tau_{yy} \\ E_{v-e}\, v + q_{v-e,x} \\ (E+p+\tau_{yy})u + \tau_{yx}\, u + q_y + q_{v-e,y} + \sum_{s=1}^{n} \rho_s\, h_s\, v_s \end{pmatrix}. \qquad (4.8)$$

Finally, the source flux W can be written as

$$W = \begin{pmatrix} w_1 \\ w_2 \\ \vdots \\ w_n \\ -\sum_{s=1}^{n} Z_s \frac{N_s}{N_e} \frac{\partial p_e}{\partial x} \\ -\sum_{s=1}^{n} Z_s \frac{N_s}{N_e} \frac{\partial p_e}{\partial y} \\ Q_{T-V} + Q_{V-V} + \sum_{s=1}^{n} w_s e_{V,s} - p_e \left(\frac{\partial u}{\partial x} + \frac{\partial v}{\partial y} \right) \\ -\sum_{s=1}^{n} Z_s \frac{N_s}{N_e} \left(u \frac{\partial p_e}{\partial x} + v \frac{\partial p_e}{\partial y} \right) \end{pmatrix}. \qquad (4.9)$$

The detailed explanation of each term was described by Candler (1988).

4.2.2 Overview of Numerical Scheme

When the above equations are solved numerically, first, the equation is transformed into the orthogonal computational domain by using a Jacobian matrix. Each flux, F, G and W, in the computation domain is split for positive and negative directions of each coordinate by diagonalization of the matrix. The flux splitting method used in this code was proposed by MacCormack (1985) except for the part which has strong pressure gradient, such as the shock wave region. For this region, the method of Steger and Warming (1979) was used. The transformed equation is discretized with a first order accuracy finite volume method in space, and backward Euler implicit scheme in time. The discretized equation becomes a block-tridiagonal system and this is solved with Gauss-Seidel line-relaxation method (see MacCormack (1985)).

4.2.3 Chemical Reactions

The chemical reaction used in this code for nitrogen is a one stage two chemical species, such as,

$$N_2 + M \leftrightarrow 2N + M, \tag{4.10}$$

and the reaction constants for this dissociation reaction were taken from Park (1985). The reaction for air is five stage five species, that is,

$$\begin{aligned} &N_2 + M \leftrightarrow 2N + M \\ &O_2 + M \leftrightarrow 2O + M \\ &NO + M \leftrightarrow O_2 + N \\ &N_2 + O \leftrightarrow NO + N \\ &NO + O \leftrightarrow O_2 + N. \end{aligned} \tag{4.11}$$

The rate constants for air were also taken from Park (1985) and Wray (1961). Finally the chemical reaction for carbon dioxide is also five stage five species, which is

$$\begin{aligned} &CO_2 + M \leftrightarrow CO + O + M \\ &CO + M \leftrightarrow C + O + M \\ &O_2 + M \leftrightarrow O + O + M. \\ &CO + O \leftrightarrow O_2 + C \\ &CO_2 + O \leftrightarrow O_2 + CO \end{aligned} \tag{4.12}$$

The reaction rate constants for these reactions were taken from Park et al. (1991).

These reaction rates constants are summarized in the table B.2 and B.3 in Appendix B.

4.2.4 Boundary Conditions

The free stream is assumed to be uniform supersonic flow, therefore, all quantities outside of bow shock wave are uniform. The boundary condition for outgoing flow is zero pressure gradient and is also supersonic even in the boundary layer. In viscous computation, the velocity at the wall is zero everywhere (no-slip condition), and in the inviscid case, the boundary condition for velocity is free slip. The boundary condition for the energy equation is specified as fixed wall temperature condition and that for chemical

reaction is non-catalytic wall, it means that the gradient of the concentration of species is zero at the wall.

4.2.5 Heat Flux Computation

For non-reacting flow, the convective heat flux to a body can be computed by

$$\dot{q}_w = \left(\kappa \frac{\partial T}{\partial n} \right)_w . \tag{4.13}$$

For viscous reacting flow, the contribution from species diffusion should be taken into account. Therefore, the convective heat flux can be expressed as

$$\dot{q}_w = \left(\kappa \frac{\partial T}{\partial n} \right)_w + \left(\rho D_{12} \sum_s h_s \frac{\partial c_s}{\partial n} \right)_w . \tag{4.14}$$

But we assume that the wall of the model is non-catalytic. Therefore, the second term of eq. (4.14) is put equal to zero and heat flux can be computed with eq. (4.13).

4.2.6 Computational Grid

For all computations in this research, the finite volume cell number was fixed to 56 $\times$ 100. For viscous flow computation, fine grid near the body surface is necessary to reproduce the boundary layer profile which governs the accuracy of the heat flux computation. Therefore, an exponentially expanding grid in wall-normal direction was used. The number of grid points was fixed and the grid was refined near the body surface relative to the coarser grid at larger distance from the body. It implies that the resolution near the shock region becomes worse and the feature of the flow field may be lost. Therefore, a different grid was used for viscous computation and inviscid computation. Coarse grid was used for inviscid computation to get good resolution in the shock wave

region and fine grid near the wall was used for viscous computation to get good resolution in the boundary layer. The grid fineness is expressed by the minimum cell size in y-direction dymin which is represented by the fraction of the nose radius r. To determine the fineness of the grid, four different grids were tried, r/2000, r/5000, r/7500 and r/10000. These grids are shown from figure 4.1 to 4.4. For the inviscid case, r/600 was used to get good resolution in the shock wave region. This is shown in figure 4.5.

4.3 Computational Interferometry

Since the flow field was visualized with differential interferometry, a computational differential interferogram had to be generated to verify the flow field solution. In this section, the methodology to generate a computational interferogram will be summarized.

4.3.1 Computation Method

A Mach-Zehnder interferogram is obtained by superposing two different beams, the reference beam and object beam. The former does not go through the flow field and the latter does go through it. The phase and the direction of the object beam are changed by the density variation in the flow field. For evaluating these changes, the index of refraction should be calculated. For equilibrium or nonequilibrium reacting gas, the refractive index is given by Mertz (1983)

$$n = 1 + \sum_{s} \kappa_s \rho_s \tag{4.15}$$

and the phase shift of the object beam compared to the reference beam can be computed by integrating the following equation along a beam path. The Gladstone-Dale constants κ_s in eq. (4,15) are summarized in table B.5 in Appendix B.

$$\phi = \frac{2\pi}{\lambda} \int_{-z}^{z} (n - n_0)\, dl. \tag{4.16}$$

For finite fringe interferometry, a linearly varying phase

$$\delta\phi = k_x\, x + k_y\, y \qquad (4.17)$$

should be added to the phase shift ϕ in eq. (4.16). Two constants k_x and k_y determine the spatial frequency and orientation of the fringes in the free stream, thus, they can be determined from the experimental interferogram.

The next step to compute the interferogram is to get the beam trajectory. Here, one important assumption was made. The beam is refracted when it passes through the non-uniform density field. But, except for the region without shock wave, the density gradient is so small that the refraction angle can be neglected, that means that the beam path is assumed to be straight. This assumption will lose computation accuracy when the beam passes through the shock wave because there exists a large density gradient in the shock wave region. But, as discussed by Yates (1992), the error according to this is small compared to the experimental error. This straight-beam assumption implies that diffraction around the body can also be neglected. To compute the beam path, the computation grid was rotated 90 degree around the x-axis and this three-dimensional grid was transformed from the physical domain into the computation domain with Jacobian matrices. The computation grids and several beam paths are shown in figure 4.6 (for inviscid flow) and in figure 4.7 (for viscous flow). The x-y plane is the image plane. A beam starts from a grid point in the x-y plane.

The judgment of which cell the marching point for the line integration of the eq. (4.16) belongs to was done as follows. Suppose a marching point along the object is in the cell number (i, j, k) and this cell is composed of the following eight grid points, grid A (i, j, k), grid B (i+1, j, k), grid C (i, j+1, k), grid D (i, j, k+1), grid E (i+1, j+1, k+1), grid F (i+1, j, k+1), grid G (i, j+1, k+1) and grid H (i+1, j+1, k). Let X_0 (x_0, y_0, z_0) and X_0' (x_0', y_0', z_0') be the coordinates of the marching point in physical domain and computational domain respectively. Let us define a function int(x) so that int(x) gives the

largest integer which is no more than x. By using this function, the coordinate of X_0' satisfies an equation,

$$\begin{cases} i = \mathrm{int}(x_0') \\ j = \mathrm{int}(y_0') \\ k = \mathrm{int}(z_0') \end{cases}. \tag{4.18}$$

Now, let δz be the marching length in physical domain. Since the object beam is straight and normal to the x-y plane, the coordinate of a new marching point Y in physical domain is $(x_0, y_0, z_0+\delta z)$. By using a Jacobian matrix, marching length in computational domain can be calculated by

$$\begin{cases} \Delta i = \dfrac{\det(A_{31})}{\det(A)}\delta z \\ \Delta j = \dfrac{\det(A_{32})}{\det(A)}\delta z \\ \Delta k = \dfrac{\det(A_{33})}{\det(A)}\delta z \end{cases}, \tag{4.19}$$

where

$$A = \begin{pmatrix} x_B - x_A & x_C - x_A & x_D - x_A \\ y_B - y_A & y_C - y_A & y_D - y_A \\ y_B - x_A & y_C - x_A & y_D - x_A \end{pmatrix}$$

and x_A represents x-coordinate of grid A. A_{ij} represents a i-jth cofactor matrix of A. And finally the cell number which the new marching point belongs to is given by

$$\begin{cases} i' = \mathrm{int}(x_0' + \Delta i) \\ j' = \mathrm{int}(y_0' + \Delta j) \\ k' = \mathrm{int}(z_0' + \Delta k) \end{cases}. \tag{4.20}$$

The density at each point during the integration was obtained by first order linear interpolation and the line integration of eq. (4.16) was done by the trapezoidal rule. This

integral started from each grid point in the x-y plane and the total phase shift was obtained by multiplying by the two because flow field and beam path are symmetric with respect to the x-y plane. Once the phase shift at each grid point is obtained, the intensity of the beam in the image plane can be obtained from

$$F(x, y) \propto \cos^2(\pi \phi). \tag{4.21}$$

Contours of F give a Mach-Zehnder interferogram. Using the intensity F(x, y), a differential interferogram can be obtained by

$$F(x, y) - F(x+dx, y+dy) = \text{const.} \tag{4.22}$$

or

$$F(x, y) - F(x-dx, y-dy) = \text{const.} \tag{4.23}$$

The difference between these two equations is the sign before dx and dy. The value of dx and dy should be determined from the separation of the two images in the experimental differential interferogram. The sign before dx and dy corresponds to the orientation of the Wollaston prism used in the experimental differential interferogram. This sign determines the direction of the fringe shift. This is easily understood qualitatively by considering a one-dimensional model, normal shock. In this case, a Mach-Zehnder interferogram shows density contours after the normal shock wave (see figure 4.8 (a)). Figure 4.8 (b) and (c) shows the difference of fringe shift direction expressed by eq. (4.22) and eq.(4.23).

4.4 Computation Cases

Basically, the computations were done based on the experimental free-stream conditions. Two cases were calculated for each condition. One was the viscous case and

the other was the inviscid case. From the viscous solution, heat flux at the wall can be computed. The inviscid solution was mainly used for the calculation of the local Reynolds number along the model surface or for obtaining the condition at the edge of the boundary layer.

CHAPTER 5

RESULTS AND DISCUSSIONS

5.1 Introduction

In this chapter, the data from the experiment and computation will be summarized. The data obtained from the wind tunnel were the burst pressure of the primary diaphragm, the pressure history in the shock tube at three stations and the nozzle reservoir pressure history. From these data, the condition at the exit of the nozzle can be computed. Based on the computed nozzle exit data, the numerical computations were also done. First of all, the computational results will be compared to the experimental differential interferogram and heat flux rate to show the validity of the computational results. And then discussion for the heat flux will be done based on both experimental results and computational results at the stagnation point as well as after body. Subsequently, the method of the extrapolation for the stanation heat transfer from the high enthalpy shock tunnel to the actual flight will be presented based on the binary scaling. Finally, the result of pressure measurement will be discussed.

5.2 Operational Data and Nozzle Exit Conditions

An example of the operational data from T5 is shown from figure 5.1 to 5.3. The summary of the primary running data of T5 is shown in table 5.1. The nozzle exit conditions were computed based on these results. The computed conditions at the exit of the nozzle are summarized in table 5.2. Computations were done based on this table.

5.3 Influence of Grid Size

As we stated in section 4.2.6, four different size grid were tried to see the influence of the grid size on the computation results, that are dymin=r/2000 (grid 1), dymin=r/5000 (grid 2), dymin=r/7500 (grid 3) and dymin=r/10000 (grid 4). These four grids are shown figure 4.1 to 4.4. Figure 5.4 shows the pressure distribution on the body with these grids. There is no significant difference between these four results. This can be understood from the fact that the inviscid computation also can reproduce the reasonably accurate pressure distribution and the resolution of the boundary layer has only very weak influence on the pressure. The computed heat flux distribution with different grid is shown in figure 5.5. Significant difference can be seen in this figure. Based on these results, the grid 3 was used for the following computations because this grid can reproduce fairly accurate heat flux and it also has a satisfactory resolution near the shock wave. There is less than 5% difference in the stagnation point heat flux between the result from grid 3 and that of grid 4. This difference can be considered to be small compared to the experimental error.

Table 5.1 Primary Running Data of T5

Run #	Condition No. (Table 3.6)	Shock Tube Pressure (kPa)	Shock Speed (m/s)	Test Gas	Nozzle Reservoir Pressure (MPa)
425	1	40.1	3570	N_2	30
429	2	50	4110	N_2	67.5
433	5	85	3226	N_2	70
435	3	36	4580	N_2	65
439	5	65	4082	N_2	95
428	1	40	3509	Air	28
432	2	50	4000	Air	60
436	4	85	3158	Air	55
430	6	85.1	2830	CO_2	70
444	7	35.1	3896	CO_2	60
445	6	85.2	2830	CO_2	65

5.4 Features of Blunted Cone Flow

The flow field was visualized with the differential interferogram and computational interferograms were also generated from the computed density field. The generation of Mach-Zehnder interferogram took about 3 hours of CPU time in SUN SPARC Station and about 30 seconds of CPU in CRAY Y-MP. An example of computational Mach-Zehnder interferogram is shown in figure 5.6. The differential interferogram could be generated from the Mach-Zehnder interferogram within a minute by SUN. For the computation for the flow field, it took 0.11 to 0.20 millisecond of CPU per grid per iteration in CRAY and 1000 to 2000 iterations were required for each case. The comparison of the experimental interferograms and the computational ones are shown in figure 5.7 to 5.9. These computational interferograms were generated from inviscid computations. From these figures, in general, it may be seen that the inviscid computation can reproduce the features of the flow field very well except for the boundary layer. Also the shock inflection point can be observed more obviously in figure 5.7 compared to figure 5.8. Discussions about shock inflection will be made in the next paragraph. In the experimental photograph in figure 5.10 (run 445), weak waves can be observed near the end of the cone and this cannot be seen in computational interferogram. As understood obviously from heat flux data shown in chapter 5.4, this might be because of the transition of the boundary layer. Figure 5.11 shows the computed interferograms based on viscous solutions. Compared to the inviscid interferogram, the resolution near the shock wave was degraded because of the coarseness of the computational grid in the shock wave region (see figure 4.6 and 4.7). However, the fringe shift in the boundary layer is resolved.

Table 5.2 Nozzle Exit Conditions

Run #	Gas	Density (kg/m^3)	Temp. (K)	Velocity (m/s)	Mach Number	Enthalpy (MJ/kg)	Species Conc. (kg/kg)
425	N_2	0.02477	1652	4518	5.660	12.7	N_2 0.983 N 0.017
429	N_2	0.04329	2413	5191	5.403	17.4	N_2 0.967 N 0.033
433	N_2	0.06228	1491	4341	5.709	11.2	N_2 0.997 N 0.003
435	N_2	0.03608	2845	5603	5.319	21.6	N_2 0.928 N 0.072
439	N_2	0.05997	2509	5237	5.363	17.5	N_2 0.975 N 0.025
428	Air	0.02609	1665	4282	5.344	12.0	N_2 0.731 O_2 0.132 NO 0.0513 N 4.38×10^{-6} O 0.0720
432	Air	0.04225	2371	4925	5.204	16.1	N_2 0.731 O_2 0.132 NO 0.0513 N 4.38×10^{-6} O 0.0720
436	Air	0.05871	1492	4010	5.352	10.1	N_2 0.723 O_2 0.184 NO 0.0645 N 8.79×10^{-8} O 0.0139
430	CO_2	0.1351	1920	3054	4.525	7.54	CO_2 0.790 CO 0.134 O_2 0.0761 C 3.13×10^{-14} O 3.73×10^{-4}
444	CO_2	0.06665	2435	3968	4.957	14.4	CO_2 0.376 CO 0.397 O_2 0.0202 C 5.12×10^{-13} O 0.0253
445	CO_2	0.1267	1887	3039	4.519	7.48	CO_2 0.788 CO 0.135 O_2 0.0767 C 3.16×10^{-14} O 2.88×10^{-4}

One significant feature of blunted cone flow is the existence of adjustment phenomenon from spherical flow to conical flow. This adjustment happens not at the junction point of sphere and cone but downstream of the junction point. This is understood from the existence of the inflection point in the shock wave. As pointed by Giese and Bergdolt (1953), the wave from the recompression of the gas causes the inflection of the shock. In dissociating gas, the shock inflection point moves upstream compared to the perfect gas. One reason for this is that the compression wave in dissociating gas is bent toward upstream (see Gai et al. (1984), also see Vincenti and Kruger, chapter VIII, section 16) and another reason is that the shock is closer to the body in the real gas case. There is the other reason of shock inflection movement. That is the movement of the location of the recompression. To see this movement, the pressure distributions along the surface are shown in figure 5.12 and 5.13. Figure 5.12 is from the lower stagnation enthalpy which is 12.7 MJ/Kg (run 425) and figure 5.13 is higher stagnation enthalpy of 21.6 MJ/Kg (run 435). Since the semiapex angle of the cone is 35 degrees, the junction of the sphere and the cone is at s/r=0.96. In real gas computation of run 425, the recompression happens around s/r=1.5. And in the frozen gas in run 425, the recompression happens in larger region and it is up to around s/r=3.0. This can be seen in the higher enthalpy case run 435. As can be seen in figure 5.13, the recompression happens around s/r=1.0 but in frozen gas condition, it happens around s/r=1.5. This can be also understood from the pressure and density along the streamline. These are shown in figure 5.15 to figure 5.17. Figure 5.14 and 5.16 show the streamline from ix=12 of the computational grid in run 425 and run 435 respectively. Significantly there exists pressure and density minimum region after the shock wave. This can also be seen in the density profile. The density profile of computation results are shown in figure 5.18 (run 425) and 5.19 (run 435). As understood from these figures, in perfect gas computation, the density minimum region is very small and the recompression is very weak compared

to the real gas computation. Therefore, the shock inflection in these figures becomes weaker in the perfect gas computations than in the real gas computations.

5.5 Heat Flux

Data of heat flux measurement are shown in from figure 5.20 to 5.30. Each column represents temperature history, integrated heat input calculated by eq. (3.5) and the heat flux history calculated by eq. (3.6) from left to right and each row corresponds to each thermocouple from the stagnation point to downstream. More detail will be discussed in the following sections.

5.5.1 Stagnation Point Heat Flux

Stagnation point heat flux data were made dimensionless in the form of Stanton number and Reynolds number. Reynolds number for the stagnation point heat flux is defined based on the free stream condition and the nose radius of the model,

$$\mathrm{Re} = \frac{\rho_\infty u_\infty r}{\mu_\infty}. \tag{5.1}$$

Stanton number for the stagnation point heat flux is defined as follows.

$$St = \frac{\dot{q}_w}{\rho_\infty u_\infty (h_0 - h_w)}$$

But in the range of this experiment, it could be assumed that the wall enthalpy is negligible in comparison with the stagnation enthalpy. Therefore, the experimental Stanton number was calculated by

$$St = \frac{\dot{q}_w}{\rho_\infty u_\infty h_0}. \tag{5.2}$$

Free stream density, velocity and stagnation enthalpy were taken from the result of the nozzle calculation in table 5.2. Free stream viscosity in eq. (5.1) was computed from the viscosity model developed by Blottner et al. (1971). The viscosity of each chemical species is calculated by

$$\mu_s = 0.1\exp\left\{\left(A_s \ln T + B_s\right)\ln T + C_s\right\}. \tag{5.3}$$

And the viscosity for the mixture can be calculated by Wilke's rule (Wilke (1950), that is

$$\mu = \sum_s \frac{X_s \mu_s}{\phi_s} \tag{5.4}$$

where

$$\begin{cases} X_s = \dfrac{c_s M}{M_s} \\ M = \left(\displaystyle\sum_s \frac{c_s}{M_s}\right)^{-1} \\ \phi_s = \displaystyle\sum_r X_r \left\{1 + \sqrt{\frac{\mu_s}{\mu_r}}\left(\frac{M_r}{M_s}\right)^{1/4}\right\}^2 \left\{\sqrt{8\left(1+\frac{M_s}{M_r}\right)}\right\}^{-1} \end{cases} . \tag{5.5}$$

The value of the coefficient As, Bs and Cs in eq. (5.3) are summarized in the table B.4 in Appendix B. The measured heat flux, the calculated Stanton number and the Reynolds number are summarized in table 5.3.

(1) Lees' Correlation

As mentioned in section 2.5, Lees calculated stagnation heat flux based upon hypersonic boundary layer self similarity. Equation (2.15) can be converted into a dimensionless form as follows.

$$St = \frac{k}{\sqrt{\mathrm{Re}}} \tag{5.6}$$

where

$$k = \frac{\sqrt{2}}{2}\sqrt{\frac{\rho_e \mu_e}{\rho_\infty \mu_\infty}}\,\mathrm{Pr}^{-2/3} G(\gamma_\infty, \gamma_{eff}, M_\infty) \tag{5.7}$$

and G is given by eq. (2.16). The density and viscosity at the outer edge of the boundary layer were taken from the inviscid numerical computation result.

Table 5.3 Stagnation Point Heat Flux Measurement Results

Run #	Gas	Re	$\dot{q}$(MW/m^2)	St
425	N_2	59690	20.4	0.0151
429	N_2	90910	46.0	0.0118
433	N_2	165900	33.4	0.0110
435	N_2	66830	55.0	0.0126
439	N_2	123600	51.3	0.00933
428	Air	50470	20.4	0.0152
432	Air	73820	41.6	0.0124
436	Air	112730	26.6	0.0112
430	CO_2	210800	20.3	0.00652
444	CO_2	89520	30.1	0.00792
445	CO_2	199200	18.4	0.00637

γ_{eff} is the effective value of the ratio of specific heats after the bow shock. For simplicity, let us consider only dissociation reaction of diatomic gas by eq. (2.1). When the diatomic gas dissociates, γ_{eff} varies as a function of the degree of dissociation. Because the specific heat ratio of monatomic gas is different from that of diatomic gas, the γ_{eff} after the bow shock wave can be estimated by following equation,

$$\gamma_{eff} = \frac{(f+2)(1-\alpha)+5\alpha}{f(1-\alpha)+3\alpha}. \tag{5.8}$$

The plot of γ_{eff} for several degrees of freedom is shown in figure 5.31. The value of γ_{eff} for each shot calculated by (5.8) is summarized in table 5.4. The species concentration for this calculation was taken from the value at the outer edge of the boundary layer. And the vibrational mode was assumed to be fully excited, therefore, the value of six was used for f in eq. (5.8). The value of k calculated for each shot condition for each γ_{eff} is also tabulated in table 5.4. The variation of k is within 3.0 % of maximum value for each gas. Therefore, k can be considered as a constant in this experiment for each gas. The reason is that the k by eq. (5.7) is changed only very weakly by free stream Mach number and the variation of the free stream Mach number is not large in this experiments. Also the viscosity ratio does not change so much during this experiments. The effect of viscosity will be discussed quantitatively in section 5.5.

Table 5.4 (1) Results from Lees' Theory for Nitrogen

Run #	Gas	γ_{eff}	k	$\dot{q}$(MW/m^2)	St
425	N_2	1.35	3.32	19.3	0.0136
429	N_2	1.38	3.27	42.4	0.0108
433	N_2	1.35	3.35	26.5	0.00875
435	N_2	1.40	3.26	51.3	0.0118
439	N_2	1.38	3.25	50.8	0.00924
		Average	3.29		

Table 5.4 (2) Results from Lees' Theory for Air

Run #	Gas	γ_{eff}	k	$\dot{q}$(MW/m^2)	St
428	Air	1.33	2.94	17.5	0.0131
432	Air	1.33	2.91	35.9	0.0107
436	Air	1.34	2.93	20.7	0.00871
		Average	2.93		

(2) Fay and Riddell's Correlation

The other correlation for the stagnation heat flux was done by Fay and Riddell (1958).

The equation for heat flux (2.21) can be written in dimensionless form with Stanton number and free stream Reynolds number with eq. (5.1) and (5.2), that is

$$St = \frac{k_f}{\sqrt{\mathrm{Re}}} \tag{5.9}$$

where

$$k_f = 0.76\,\mathrm{Pr}^{-0.6}\left\{1+\left(Le^{0.52}-1\right)\frac{h_D}{h_0}\right\}\left(\frac{2(p_e-p_\infty)}{\rho_\infty u_\infty^2}\frac{\rho_\infty}{\rho_e}\right)^{1/4}\frac{(\rho_e\mu_e)^{0.4}(\rho_w\mu_w)^{0.1}}{(\rho_\infty\mu_\infty)^{0.5}}. \tag{5.10}$$

The density and pressure values at the outer edge of boundary layer were taken from inviscid computation result at i=2, j=2 and the values at the wall were taken from the values at i=2, j=2 of the viscous solution. The computation cell at i=2, j=2 is the closest cell to the stagnation point. Originally this correlation was based on the data for symmetric diatomic gas. Therefore, the correlation factor k_f was calculated based upon the results of nitrogen and air. The result is summarized in table 5.5. The variation of the values is within 5 % of maximum for each gas. Therefore, k_f can be considered as constant for each gas.

Table 5.5 (1) Results from Fay and Riddell Correlation for Nitrogen

Run #	425	429	433	435	439	Ave.
k_f	3.60	3.46	3.59	3.43	3.43	3.50
q	20.9	44.8	28.4	54.0	53.5	
St	0.0147	0.0115	0.00813	0.0133	0.00976	

Table 5.5 (2) Coefficient for Fay and Riddell Correlation for Air

Run #	428	432	436	Ave.
k_f	3.32	3.26	3.26	3.28
q	19.8	40.2	23.1	
St	0.0148	0.0120	0.00971	

(4) Fay and Riddell Correlation with Ideal Dissociating Gas Model

The condition after the normal shock wave in ideal dissociating gas (IDG) can be computed based on the equations summarized in section 2.4. By assuming that nitrogen behaves as IDG and equilibrium state variables, such as temperature or density, are equal

to the post shock values of IDG, the stagnation heat flux can be estimated based on Fay and Riddell correlation. The density at the wall necessary for Fay and Riddell formula was calculated based on the following simplification. The species concentration is constant throughout the shock layer and the boundary layer. Then the wall density was calculated with eq. (2.13). The temperature of the wall assumed to be 300 K that is same as numerical computation. The density at the wall was calculated with the wall temperature and the species concentration stated above. The result is summarized in Table 5.6.

Table 5.6 Stagnation Point Heat Flux Estimation with IDG and Fay and Riddell Correlation

Run #	425	429	433	435	439
$\dot{q}_{eq}$ (MW/m^2)	17.5	37.6	24.2	45.5	46.9
$\dot{q}_{fr}$ (MW/m^2)	11.6	21.1	18.2	25.9	22.8

(4) Summary of Stagnation Heat Flux

As a summary, heat fluxes from six different methods are tabulated in table 5.7.

Table 5.7 Summary of Stagnation Point Heat Flux

Run #	(1) $\dot{q}$ St	(2) $\dot{q}$ St	(3) $\dot{q}$ St	(4) $\dot{q}$ St	(5) $\dot{q}$ St	(6) $\dot{q}$ St
425	21.4 0.0151	18.8 0.0133	19.3 0.0136	20.9 0.0147	17.5 0.0123	11.6 0.00816
429	46.0 0.0118	49.4 0.0126	42.4 0.0108	44.8 0.0115	37.6 0.00962	21.1 0.00540
433	33.4 0.0104	28.5 0.00884	26.5 0.00875	28.4 0.00813	24.2 0.00799	18.2 0.00601
435	55.0 0.0135	54.0 0.0133	51.3 0.0118	54.0 0.0133	45.5 0.0104	25.9 0.00594
439	51.3 0.00933	65.8 0.0120	50.8 0.00924	53.5 0.00974	46.9 0.00853	22.8 0.00415
428	20.4 0.0152	18.8 0.0140	17.5 0.0131	19.8 0.0148		
432	41.6 0.0124	45.2 0.0135	35.9 0.0107	40.2 0.0120		
436	26.6 0.0112	27.6 0.0116	20.7 0.00871	23.1 0.00971		
430	20.3 0.00652	12.0 0.00385				
444	30.1 0.00792	13.6 0.00357				
445	18.4 0.00637	11.0 0.00383				

(1) : Experimental Data
(2) : Computation Result
(3) : Computation + Lees
(4) : Computation + Fay and Riddell
(5) : IDG + Fay and Riddell, eq. (2.21):Equilibrium
(6) : IDG + Fay and Riddell, eq. (2.22):frozen

(5) Discussions

Figure 5.32 shows experimental data, computation data and correlation line based on Lees' theory and Fay and Riddell formula in dimensionless form. Fay and Riddell correlation shows very good agreement with the experimental data. There exists the error more than 14 % in run 433 and run 445. But the error in the other runs are less than 7 %. Lees' theory gives lower heat flux than experimental results. This may be explained by too small value of γ_{eff} in eq. (5.8).

In general, the stagnation point heat flux data were very well correlated with free stream Reynolds number based on nose radius and Stanton number. This implies that the binary scaling with Stanton number defined by eq. (5.2) is a very useful method for the evaluation of the stagnation heat flux. This is mainly because the heat transfer in the stagnation region is dominated by the dissociation reaction and this means that the first term in eq. (2.9) plays a more important role than the second term. This can be understood quantitatively by observing the reaction rate along the streamline. This is shown in figure 5.33 and figure 5.34 and each reaction rate corresponds to the streamline shown in figure 5.14 and 5.16 respectively. For run 425 that is the lower stagnation enthalpy case, the dissociation rate is always much higher than the recombination rate. Therefore, the dissociation dominates the overall chemical reactions and it implies that binary scaling is applicable. But for the higher stagnation enthalpy case, the recombination rate becomes higher than in the range of $0.3 < s/r < 2.0$ and the dissociation rate and the recombination rate become close each other. Therefore, the recombination cannot be ignored in this case and this implies that the binary scaling does not applicable anymore in the region of $s/r > 0.3$.

One more important feature can be mentioned from figure 5.32. The experimental data fits well to a line whose gradient is -0.5. This means that heat flux is inversely proportional to the square root of the nose radius and this feature can be reproduced by fixed radius experiments.

5.5.2 Heat Flux Distribution on the After Body

Both experimental and computational heat flux distributions including stagnation point are shown in figure 5.35 to 5.45. For nitrogen and air cases, computational results show good agreement with experimental data. This implies that both experimental and computational methodology were appropriate for the study of heat flux in air and nitrogen. But for the carbon dioxide cases, computed heat flux is less than experimental results by a factor of 2. This is partly because of the effect of the recombination in the boundary layer. As mentioned in section 4.2, computations assume that the model wall is non-catalytic. During the test, carbon particles deposited on the model surface might be also oxidized by atomic oxygen in the test gas. Therefore to be exact, the model surface should probably have been considered to be catalytic. This hypothesis is endorsed by the results from air. The difference between computation and experiment is slightly larger in air cases than nitrogen cases. Carbon dioxide consumes more energy to equilibrate its internal degrees of freedom than air. In other words, carbon dioxide releases more energy than air when it recombines. Therefore, the effect of recombination in the boundary layer becomes more significant in carbon dioxide cases. Figure 5.46 ,5.47 and 5.48 show concentration profiles in the boundary layer. Temperature profiles are also shown in the figures as references. These three figures are taken from the location of the same local Reynolds number. From these figures, the recombination in the boundary layer is more significant in carbon dioxide than air or nitrogen even for non catalytic computation. To examine this quantitatively, the code to be able to change the catalyticity of the wall is necessary. Heat flux distribution on the after body was predicted based on Lees' theory for selected cases. Heat flux on after body was calculated as a ratio to the stagnation heat flux calculated in the previous section. Therefore the absolute value of heat flux on the after body was below the experimental data and computation result because Lees' theory underestimates the stagnation heat flux. But the heat flux distribution by Lees' theory was well fit to experimental data and computation results.

Figure 5.49 shows dimensionless heat transfer characteristics on the after body of the model. The data are well correlated in the same gas but the differences among the gases are significant. Stanton number of carbon dioxide tends to be highest in three test gases and that of nitrogen tends to be lowest. This is partly because the flow at after body has two characteristic lengths, one is nose radius and the other is the distance from the stagnation point. Therefore these two lengths should be taken into account to correlate. The other reason for this is that the recombination reaction may play a more important role than the dissociation in the heat transfer on the after body. This can be also understood from figure 5.34. In higher enthalpy case (run 435), the recombination reaction rate becomes larger than the dissociation rate and it means that the binary scaling does not work any more after this region. Therefore the local Reynolds number and Stanton number correlation may not work. For these reasons, the other correlation should be found for the after body heat flux.

5.6 Scaling of Stagnation Heat Flux to Actual Flight Condition

The data presented in the above sections were obtained from the wind tunnel with scaled model. From the practical design point of view, it is very important to study the scaling law of the scaled model experiments and actual flight conditions because heat transfer is one of the most dominant factors for the design of hypersonic vehicles. In this section, one simple method of the scaling for stagnation heat flux will be presented.

The "model" hypersonic vehicle is assumed to have a nose radius of 0.4 m. The selected free stream condition of this "model" vehicle is summarized in table 5.8. The velocity is same as the experimental conditions in table 5.2. The density of the flow is determined with the condition that the binary scaling parameter is constant i.e., the density of the flow times the nose radius is kept constant. For example, from the experimental data of run 428 in table 5.2,

$$\rho' = \frac{r}{r'}\rho$$
$$= \frac{0.03}{0.4} \times 0.02609$$
$$= 0.001957 \ (kg / m^3)$$

And the temperature is determined from U.S. Standard Atmosphere (1976) based on this density.

Table 5.8 Free Stream Conditions for "Model" Vehicle

Case # (Run #)*	Height (m)	Density (kg/m^3)	Temp. (K)	Velocity (m/s)	Mach Number	Species Conc. (kg/kg)
1 (428)	45000	0.001957	264.2	4282	13.41	N_2 0.8 O_2 0.2 NO 0.0 N 0.0 O 0.0
2 (432)	41600	0.003169	254.8	4925	16.01	N_2 0.8 O_2 0.2 NO 0.0 N 0.0 O 0.0
3 (436)	39400	0.004403	248.7	4010	13.10	N_2 0.8 O_2 0.2 NO 0.0 N 0.0 O 0.0

* : Corresponds to the Run # in table 5.1 and 5.2

From the results in section 5.4.1, the stagnation point heat flux is well correlated with Stanton number and Reynolds number by the following equation.

$$St = \frac{k}{\sqrt{\mathrm{Re}}} \qquad (5.11)$$

The coefficient k in this equation should be determined by some ways, i.e., by experiments or by numerical computation. The scaling methodology will be discussed based on this equation. In general, the differences between hypervelocity shock tunnel experiments with scaled model and actual flight are in the following quantities,

(1) Degree of dissociation of free stream,

(2) free stream temperature (Mach number),

(3) surface temperature,

(4) characteristic length.

Of these four factors, (4) has already been taken into account by considering the binary scaling parameter. The effects of the other three factors will be examined in the following sections. The gas used in this study is air because of the practical purposes.

5.6.1 Effect of Free Stream Dissociation

To check the influence of (1), the computation was conducted with zero free stream dissociation and with the same condition for other parameters. The free stream condition is summarized in table 5.8. The experimental data, the computed results based on table 5.2 and the computed results based on table 5.8 are summarized in table 5.9. From these results, the effect of the free stream dissociation can obviously neglected.

5.6.2 Effect of Free Stream Temperature

The free stream temperature in typical hypervelocity shock tunnel is order of 1000 K. But in the actual flight, the free stream temperature at high altitude, where the aerodynamic heating is an important issue is much lower than that. The computation conditions to examine this effect are shown in table 5.10. The temperature is taken from table 5.8.

Table 5.9 Free Stream Conditions of Zero Dissociation

Case # (Run #)*	Density (kg/m^3)	Temp. (K)	Velocity (m/s)	Mach Number	Enthalpy (MJ/kg)	Species Conc. (kg/kg)
4 (428)	0.02609	1665	4282	5.344	12.0	N_2 0.8 O_2 0.2 NO 0.0 N 0.0 O 0.0
5 (432)	0.04225	2371	4925	5.204	16.1	N_2 0.8 O_2 0.2 NO 0.0 N 0.0 O 0.0
6 (436)	0.05871	1492	4010	5.352	10.1	N_2 0.8 O_2 0.2 NO 0.0 N 0.0 O 0.0

* : Corresponds to the Run # in table 5.1 and 5.2

Table 5.10 Computed Stagnation Heat Flux (MW/m^2)

Run #	428	432	436
Experiment	20.4	41.6	26.6
Comp. with Dissociation	18.8	45.2	27.6
Comp. without Dissociation	18.4	44.5	27.4

Table 5.11 Free Stream Conditions of Lower Temperature

Case # (Run #)*	Density (kg/m^3)	Temp. (K)	Velocity (m/s)	Mach Number	Enthalpy (MJ/kg)	Species Conc. (kg/kg)
7 (428)	0.02609	264.2	4282	13.41	9.3	N_2 0.731 O_2 0.132 NO 0.0513 N 4.38×10^{-6} O 0.0720
8 (432)	0.04225	254.8	4925	16.01	12.3	N_2 0.731 O_2 0.132 NO 0.0513 N 4.38×10^{-6} O 0.0720
9 (436)	0.05871	248.7	4010	13.10	8.92	N_2 0.723 O_2 0.184 NO 0.0645 N 8.79×10^{-8} O 0.0139

* : Corresponds to the Run # in table 5.1 and 5.2

The difference in the temperature works through the viscosity and Mach number. The effect of the temperature on k in eq. (5.11) can be estimated quantitatively by using eq. (2.16) and (5.7). Figure 5.50 shows the variation of the function G defined by eq. (2.16) with the variation of free stream Mach number in constant $\gamma_{eff.}$ The Mach number difference causes less than 0.5 % of difference in G. Another factor affected by the difference of the temperature is the value of γ_{eff}. Different free stream Mach number may results in different γ_{eff}. Figure 5.51 shows the variation of function G with variable γ_{eff} and with constant free stream Mach number. The relation between Mach number and γ_{eff} is not trivial and the value of γ_{eff} affects the value of k with a magnitude of 10 %. Therefore, we neglect the effect of the temperature through the variation of γ_{eff} in this study. The other factors affected by free stream temperature is the ratio of density and viscosity in eq. (5.7). The calculated density ratio and viscosity ratio for three cases are summarized in table 5.12. The viscosity ratio is calculated with Blottner's viscosity

model based on the numerically computed temperature ratio. The density ratio is calculated based on the numerical computation results. The table also includes the value of function G from eq. (2.16).

Table 5.12 Effect of Free Stream Temperature

Condition	Run 428	Case 7	Run 432	Case 8	Run 436	Case 9
T_∞	1665	264.2	2371	254.8	1492	248.7
T_e	5770	5300	6800	6300	5245	4700
μ_e/μ_∞	2.38	6.50	2.17	7.53	2.33	6.15
ρ_e/ρ_∞	8.54	9.2	9.15	10.0	8.62	9.8
$\sqrt{\frac{\rho_e \mu_e}{\rho_\infty \mu_\infty}}$	4.51	7.73	4.46	8.68	4.48	7.76
G	1.0059	1.0010	1.0062	1.0007	1.0059	1.0010
Ratio of $G\sqrt{\frac{\rho_e \mu_e}{\rho_\infty \mu_\infty}}$	1.71		1.94		1.72	

From this table the free stream temperature has strong influence on k through the viscosity. Therefore, when the stagnation point heat flux in the shock tunnel is scaled up to the flight condition, the difference of the viscosity of the free stream should be compensated.

5.6.3 Effect of Wall Temperature

In the shock tunnel experiment, the wall temperature is in the range of 300 K to 600 K approximately while the vehicle surface temperature may rise to 2000 K at the stagnation point. Lees' correlation does not include the effect of the wall temperature. But Fay and Riddell's correlation considers this factor. Therefore, an approximate estimation of this effect can be conducted by using eq. (5.10). Let us assume that the wall temperature is changed from 300 K to 2000 K and the pressure remains constant.

By using Blottner's viscosity model again with undissociated air (80 % nitrogen + 20 % oxygen),

$$\left[\frac{(\rho_w \mu_w)_{T=2000K}}{(\rho_w \mu_w)_{T=300K}}\right]^{0.1} \approx 1.08$$

Therefore, the effect of wall temperature is small compared to the effect of the free stream temperature and even for the stagnation region where the temperature of the vehicle surface becomes high, this effect is not so significant compared to the experimental error. Therefore, in this approximate estimation, we can ignore this effect. But if more accuracy is needed this effect should be taken into account.

5.6.4 Calculation of Stagnation Heat Flux at Flight Condition

To show the validity of the discussion above, the stagnation point heat fluxes in the flight conditions in table 5.8 are extrapolated from the experimental data and are compared with the computation results. The extrapolating procedure is as follows.

(1) Calculate the Stanton number with the heat flux from the experiments

(2) Calculate the free stream Reynolds number based on the nose radius

(3) Calculate the coefficient k by eq. (5.11) with the experimental data

(4) Compute the ratio of $G\sqrt{\frac{\rho_e \mu_e}{\rho_\infty \mu_\infty}}$

(5) Consider the effect of the wall temperature like section 5.5.2, if necessary

(6) Modify k by multiply the result of (4) (and (5))

(7) Calculate the free stream Reynolds number in flight condition

(8) Compute the Stanton number and heat flux by using the result of (6) and (7)

The result of this procedure is summarized in table 5.13. The heat fluxes in the last column are taken from the numerical computation results based on the condition of table

5.8. The wall temperature is assumed to be 300 K for all cases. Therefore, we can neglect the effect of the wall temperature.

Table 5.13 Results of Extrapolation to Flight Conditions

	Case 1	Case 2	Case 3
Heat Flux (Run #)	20.4 (428)	41.6 (432)	26.6 (436)
St	0.0152	0.0124	0.0112
Re (shock tunnel)	50470	73820	112730
k Ratio of	3.41	3.37	3.76
$G\sqrt{\frac{\rho_e \mu_e}{\rho_\infty \mu_\infty}}$	1.71	1.94	1.72
modified k	5.83	6.54	6.47
Re (flight)	164700	317100	363900
St (flight)	0.0144	0.0116	0.0107
Heat Flux (MW/m^2)	1.12	2.23	1.55
Computed Heat Flux (MW/m^2)	0.964	2.34	1.51

From this table, this method can estimate the stagnation heat flux in satisfactory accuracy.

5.7 Pressure Measurement Results

One example of the output of the transducers is shown in figure 5.52. The transducer of channel two was attached to the model directly and channel 3 to 7 were isolated with two o-rings from the model and there is no metal contact between the model and the transducers. From the trace of channel 2 to 7 of all runs (channel 1 was a Pitot probe data and it was isolated from the model), there is no significant difference in signal to noise ratio between channel 2 and the others. It implies that it is not necessary to

isolate transducers from the model if the model is made of steel and it is heavier than this model. And it also implies that the rigidity of the model support is enough for the pressure measurement.

The measured static pressure value gives very poor results. The reason for this phenomenon is as follows. When pressure transducers were installed in the model, the diaphragm of transducer was covered with silicon rubber of thickness of less than 1 mm to protect from the erosion of dusty gas and from the thermal problem. If this silicon rubber is too thick, it may work as a damping device. For channel 4, 5 and 6, silicon rubber was too much and the pressure hole was filled with silicon. This was confirmed when the transducers were taken out from the model.

For the above reason, quantitative static pressure data were not obtained but the know-how of the installation of the pressure transducers has been learned.

CHAPTER 6

CONCLUSIONS

6.1 Conclusions

In this thesis, the fundamental physics of chemically nonequilibrium flow has been studied by both experimental and computational approach. Each result has several features. Therefore, some conclusions can be made for each aspect.

First of all, the method to measure the heat flux has turned out to be very reliable and robust. This is endorsed by the comparison among the experimental data, the computation data and the theoretical results.

As for the stagnation point heat flux, the experimental data were very well correlated with free stream Reynolds number and Stanton number for all gases. And this also implies that the binary scaling is eligible for stagnation point heat flux. The difference among the three gases, nitrogen, air and carbon dioxide, is very small. Once correlation coefficient is calculated experimentally, stagnation point heat flux in different condition can be predicted for all gases. Therefore, the experimental approach turned out to be a very reliable way to determine this correlation coefficient.

The heat flux on the after body is also well correlated for each test gas by using Stanton number and local Reynolds number but the difference among the gases are more significant. The reason for this is that the recombination of atoms plays a more important role in the heat transfer mechanism at the after body.

From the heat flux data at after body and the interferograms, the beginning of the transition of boundary layer can be observed. This data are very rare data in the area of hypervelocity blunt body flow.

The two temperature model computation has been shown to be a reliable method to compute the nonequilibrium flow field. Even the inviscid computation can reproduce the density fields as a whole except for the boundary layer and shock wave region where the effect of viscosity is dominant. As can be seen from the viscous computational interferogram, the boundary layer can be observed clearly. For the heat flux computation, in general, the viscous computation can reproduce the heat fluxes very well but the results strongly depend on the grid fineness. And also the considerations for surface catalysis are needed because the model surface is not non-catalytic anymore. Therefore, the computation code for partially catalytic surface is needed for more detailed discussion.

Lees' theory and Fay and Riddell correlation based on inviscid computation give very close correlation coefficient with experimental data. But the Lees' theory tends to give lower heat flux than experimental data. But in the after body, Lees' theory can give dramatically good results compared to the experimental results.

When the stagnation heat flux in flight condition is extrapolated from the experimental data in the shock tunnel, the difference of the free stream temperature is the most dominant factor which works through the difference of the viscosity. The effect of the free stream dissociation can be neglected and the effect of the difference of the wall temperature needs to be considered when more accurate estimation is needed.

A simple method for the extrapolation from the experiment to flight condition is proposed and it can produce the fairly good result compared to the numerical computation.

The quantitative data for static pressure could not be obtained this time, but the know-how for the installation of the transducer could be learned.

6.2 Further Study

For understanding the effects on the surface catalysis, the study for the fabrication of the model whose surface catalysis is quantitatively measured is very important. Of

course, the measurement technique for the chemical species concentration like PLIF is necessary for this study. And also the computation code for partially catalytic surface will be a very powerful tool for understanding the flow physics.

The study of heat transfer on after body is also attractive. Especially, to find the new correlation which can incorporate the difference of gas will be an interesting subject. And also the study of the scaling law for after body heat transfer is the succeeding area of it.

By using carbon dioxide, the transition of the boundary layer can be obtained even with blunt body. Therefore, the transition in blunt body can be an interesting research.

Based on the know-how for the installation of the pressure transducers, the pressure measurement experiments is also recommended.

In the last, the study for various angles of blunted cones will be very interesting. The shock layer becomes thinner if more slender blunted cone is used. Therefore , the inflection point of the bow shock may have much more influence on the flow feature e.g., heat flux, pressure distribution.

REFERENCES

Alpher, R. A. and White, D. R. (1959), Optical Refractivity of High-Temperature Gases. I. Effects Resulting from Dissociation of Diatomic Gases, Physics of Fluids, Vol. 2, No. 2, pp. 153 - 161.

Belanger, J. (1993), The Studies of Mixing and Combustion in Hypervelocity Flows with Hot Hydrogen, Ph.D Thesis, California Institute of Technology.

Blottner, F. G., Johnson, M. and Ellis, M. (1971), Chemically Reacting Viscous Flow Program for Multi-Component Gas Mixtures, Report No. SC-RR-70-754, Sandia Laboratories, Albuquerque, New Mexico.

Candler, G. V. and MacCormack, R. W. (1988), The Computation of Hypersonic Ionized Flows in Chemical and Thermal Nonequilibrium, AIAA Paper No. 87-1546.

Candler, G. V. (1988), The Computation of Weakly Ionized Hypersonic Flows in Thermo-Chemical Nonequilibrium, Ph.D Thesis, Stanford University.

Cummings, E. (1993), The Design of T5 Diaphragm Indenter, GALCIT Report, in preparation.

Fay, J. A. and Riddell, F. R. (1958), Theory of Stagnation Point Heat Transfer in Dissociated Air, Journal of the Aeronautical Sciences, Vol. 25, No. 2, pp. 73 - 85.

Freeman, N. C. (1958), Non-equilibrium flow of an ideal dissociating gas, Journal of Fluid Mechanics, Vol. 4, pp. 407 - 425.

Gai, S. L., Sandeman, R. J. and Lyons, P. R. A (1984), Shock Shape over a Sphere Cone in Hypersonic High Enthalpy Flow, AIAA Journal, Vol. 22, No. 7, pp. 1007 - 1010.

Gai, S. L. and Lyons, P. R. A. (1989), Shock Standoff from Blunt Cones in High-Enthalpy Nonequilibrium Nitrogen Flow, AIAA Journal, Vol. 27, No. 7, pp. 918 - 920.

Giese J. H., and Bergdolt, V. E. (1953), Interferometric Studies of Supersonic Flows about Truncated Cones, Journal of Applied Physics, Vol. 24, No. 11, pp. 1389 - 1396.

Hornung, H. G. (1972), Non-equilibrium Dissociating Nitrogen Flow Over Spheres and Circular Cylinders, Journal of Fluid Mechanics, Vol. 53, pp. 149 - 176.

Hornung, H. G. (1976), Non-equilibrium Ideal Dissociation after a Curved Shock Wave, Journal of Fluid Mechanics, Vol. 74, 143.

Hornung, H. G. (1992), Performance Data of the New Free-Piston Shock Tunnel at GALCIT, AIAA paper No. 92-3943.

Kaye, G. W. C. and Laby, T. H. (1986), *Tables of Physical and Chemical Constants and Some Mathematical Functions*, Longman, New York.

Koppenwallner, G. (1984), Fundamental of Hypersonics: Aerodynamics and Heat Transfer, in the Short Course Notes entitled Hypersonic Aerothermodynamics, Von Karman Institute of Fluid Dynamics, Rhose Saint Genese, Belgium.

Lees, L. (1956), Laminar Heat Transfer Over Blunt-Nosed Bodies at Hypersonic Flight Speeds, Jet Propulsion, Vol. 26, pp. 259 - 269.

Lighthill, M. J. (1957), Dynamics of a Dissociating Gas. Part 1. Equilibrium Flow., Journal of Fluid Mechanics, Vol. 2, p. 1.

Lordi, J. A., Mates, R. E. and Mosella, J. R. (1965), Computer Program for the Numerical Solution of Nonequilibrium Expansions of Reacting Gas Mixtures, Contract No. NASr-109, Cornell Aeronautical Laboratory Inc., Buffalo, N. Y.

MacCormack, R. W. (1985), Current Status of the Numerical Solutions of the Navier -Stokes Equations, AIAA Paper No. 85-0032.

Macrossan, M. N. and Stalker, R. J. (1987), Afterbody Flow of a Dissociating Gas Downstream of a Blunt Nose, AIAA Paper No. 87-0407.

Macrossan, M. N. (1990), Hypervelocity flow of dissociating nitrogen downstream of a blunt nose, Journal of Fluid Mechanics, Vol. 217, pp. 167- 202.

McIntosh, M. K. (1971), ESTC Program ('Equilibrium Shock Tube Calculation"), WRE-Tech. Note 180, Australian Defense Scientific Service, Weapons Research Establishment, Salisbury, South Australia.

Mertz, L. (1983), Real-Time Fringe-Pattern Analysis, Applied Optics, Vol. 22, No. 10, pp. 1535 - 1539.

Merzkirch, W. (1974), *Flow Visualization*, Academic Press Inc., New York.

Muylaert, J., Walpot, L., Hauser, J., Sagnier, P., Devezeaux, D., Papirnyk, O. and Lourme, D. (1992), Standard Model Testing in the European High Enthalpy Facility F4 and Extrapolation to Flight, AIAA Paper No. 92-3905.

Nagamatsu, H. T. (1960), Geiger, R. E. and Sheer, Jr., R. E., Real Gas Effects in Flow Over Blunt Bodies at Hypersonic Speeds, Journal of Aeronautical Sciences, Vol. 27, No. 4.

Park, C. (1985), On Convergence of Computation of Chemically Reacting Flows, AIAA Paper No. 85-0247.

Park, C. (1988), Assessment of a Two-Temperature Kinetic Model for Dissociating and Weakly Ionizing Nitrogen, Journal of Thermophysics and Heat Transfer, Vol. 2, No. 1, pp. 8 - 16.

Park, C. (1989), Assessment of Two-Temperature Kinetic Model for Ionizing Air, Journal of Thermophysics and Heat Transfer, Vol. 3, No. 3, pp. 233 - 244.

Park, C., J. Jaffe, J. Howe and Candler, G. V. (1991), Chemical Kinetic Problems of Future NASA Missions, AIAA Paper No. 91-0464.

Schultz, D. L. and Jones, T. V. (1973), Heat-transfer Measurements in Short-duration Hypersonic Facilities, AGARD-AG-165.

Stalker, R. J. (1989), Approximations for Nonequilibrium Hypervelocity Aerodynamics, AIAA Journal, Vol. 27, No. 12, December, pp. 1761 - 1769.

Steger J. and Warming, R. W. (1979), Flux Vector Splitting of the Inviscid Gasdynamics Equations with Application to Finite Difference Methods, NASA TM-78605.

Traugott, S. C. (1962), Some Features of Supersonic and Hypersonic Flow About Blunted Cones, Journal of the Aerospace Sciences, Vol. 29, pp. 389 - 399.

U.S. Standard Atmosphere (1976), National Oceanic and Atmospheric Administration.

Vincenti, W. G. and Kruger, Jr., C. H (1965), *Introduction to Physical Gas Dynamics*, John Wiley and Sons, Florida.

Wilke, C. R. (1950), A Viscosity Equation for Gas Mixtures, Journal of Chemical Physics, Vol. 18, pp. 517 - 519.

Wray, K. L. (1961), Chemical Kinetics of High Temperature Air, presented at the ARS International Hypersonics Conference, Cambridge, Massachusetts.

Yates, L. A. (1992), Images Constructed from Computed Flowfields, AIAA paper No. 92-4030.

References which are not referred in the text

Anderson Jr., J. D. (1989), *Hypersonic and High Temperature Gas Dynamics,* McGraw-Hill, New York.

Fletcher, C. A. J. (1991), *Computational Techniques for Fluid Dynamics Vol. I and II Second Edition,* Springer-Verlag, New York.

Gnoffo, P. A., Gupta, R. N. and Shinn, J. L. (1989), Conservation Equations and Physical Models for Hypersonic Air Flows in Thermal and Chemical Nonequilibrium, NASA TP-2867.

Hornung, H. G. (1992), Ae234 Hypersonic Aerodynamics Lecture Notes, California Institute of Technology.

Liepmann, H. W. and Roshko, A. (1957), *Elements of Gasdynamics*, John Wiley and Sons, Inc., New York.

Rock, S. G., Candler, G. V. and Hornung, H. G. (1992), Analysis of Thermo-Chemical Nonequilibrium Models for Carbon Dioxide Flows, AIAA Paper No. 92-2852.

Thompson, P. A. (1988), *Compressible-Fluid Dynamics*.

Whitham, G. B. (1976), *Linear and Nonlinear Waves*, John Wiley and Sons, Inc., New York.

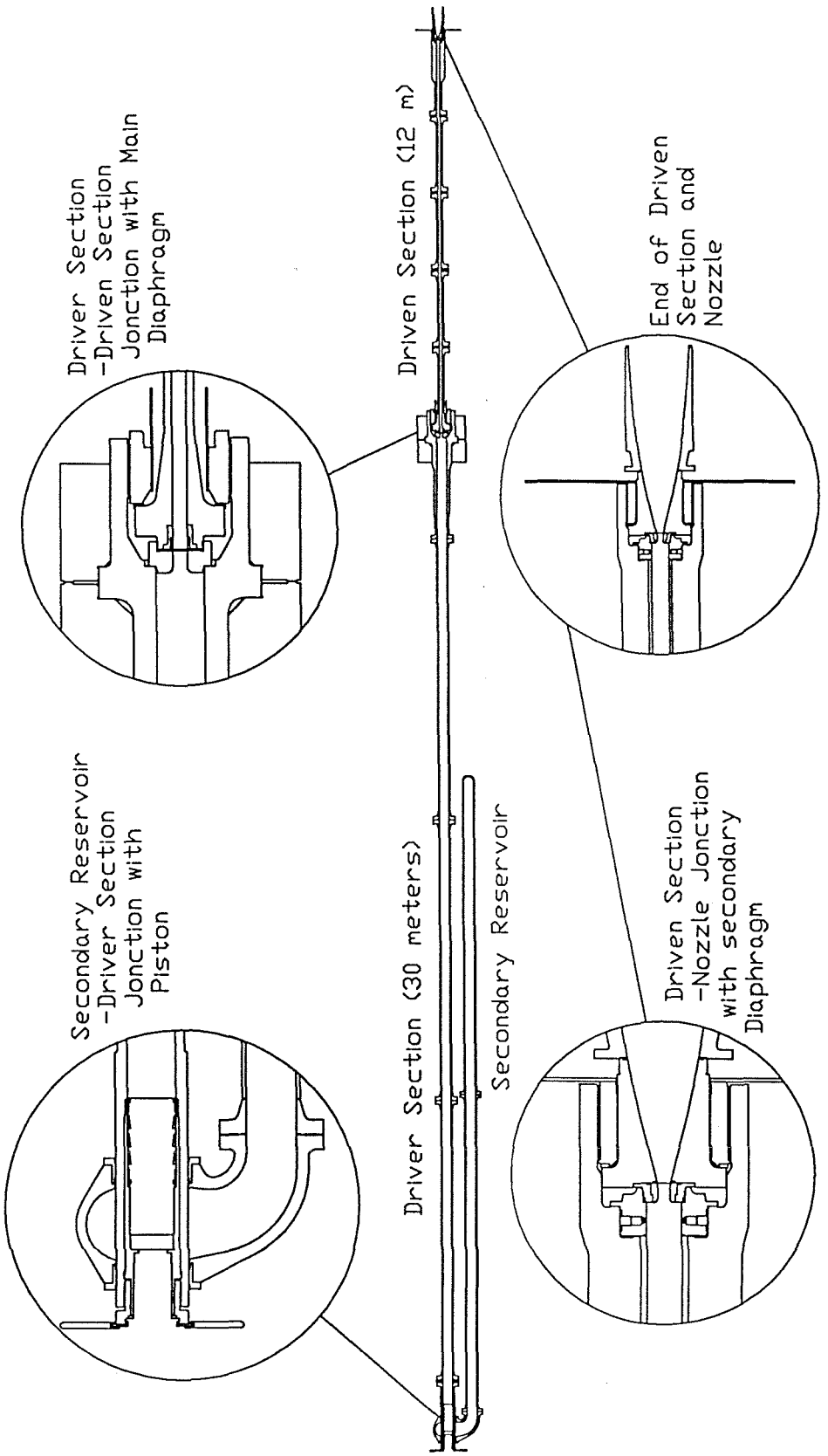

Figure 3.1 Schematic of T5

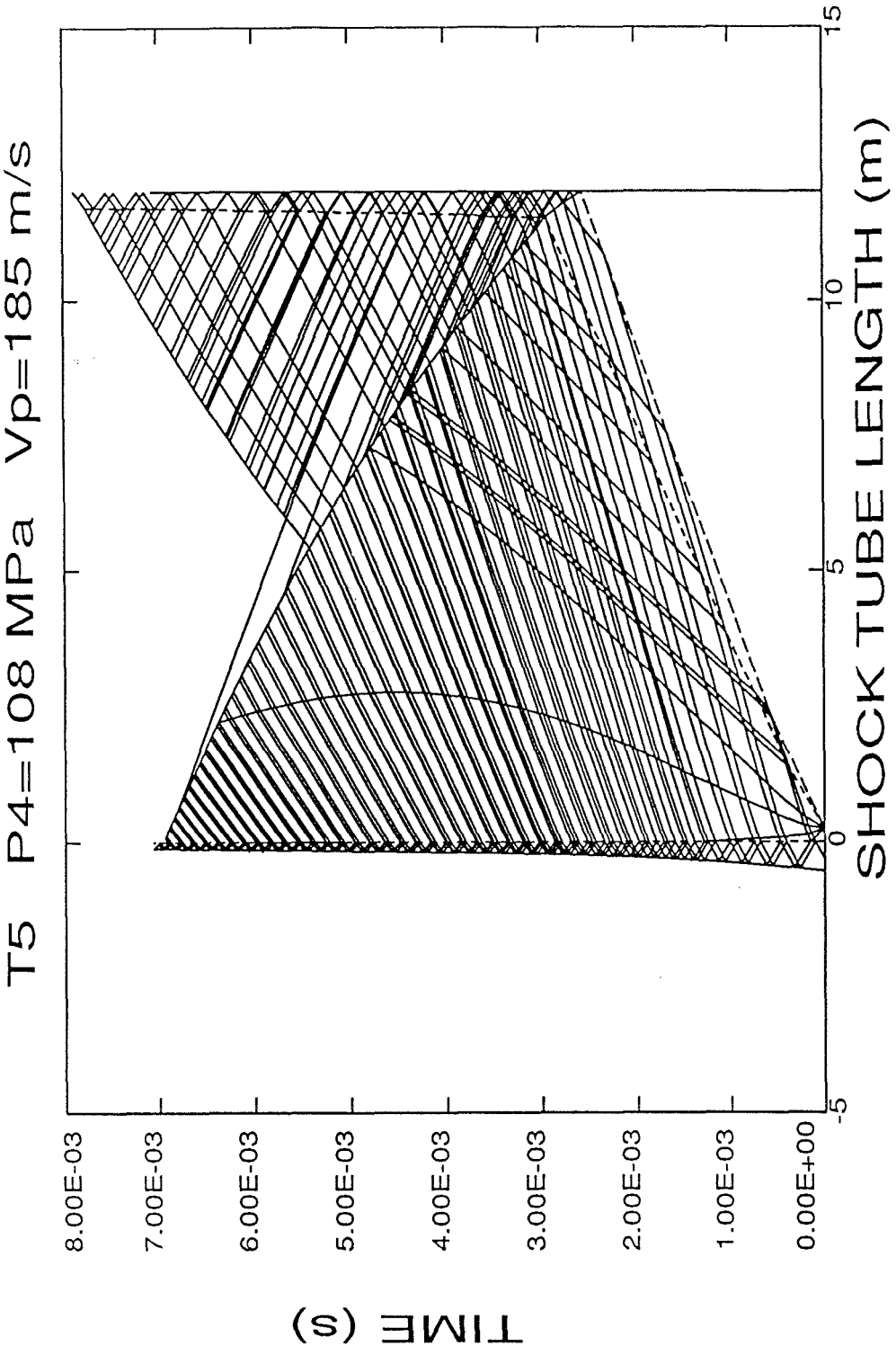

Figure 3.2 Operating Diagram of T5

(from Belanger (1993))

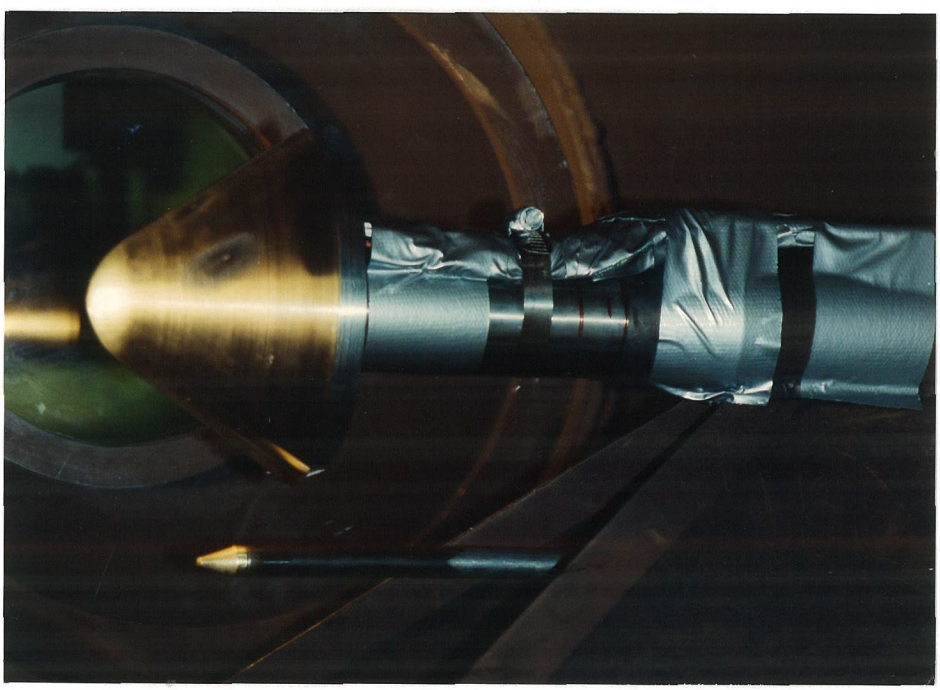

Figure 3.3. Photograph of Wind Tunnel Model

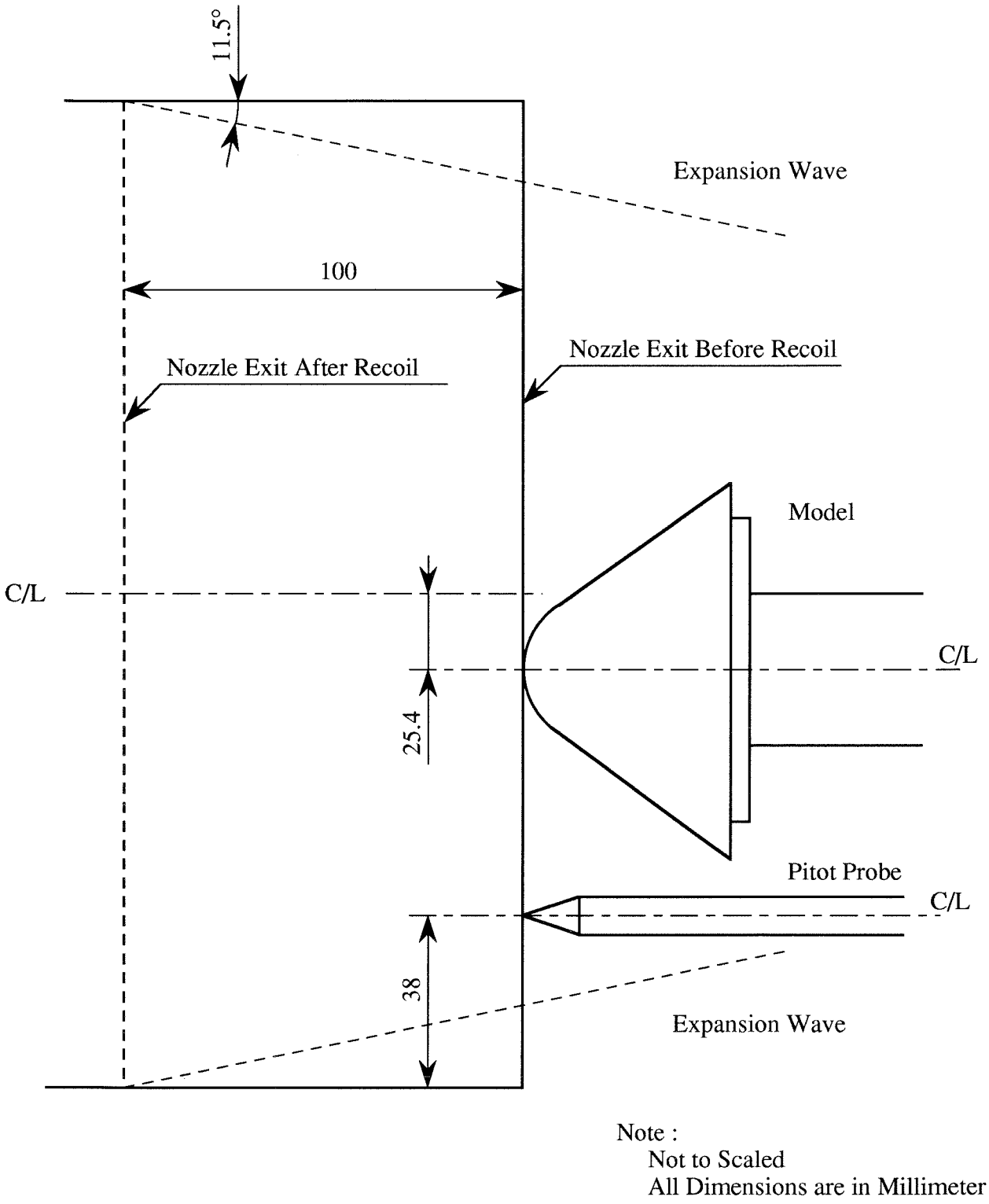

Figure 3.4. Arrangement of Test Section

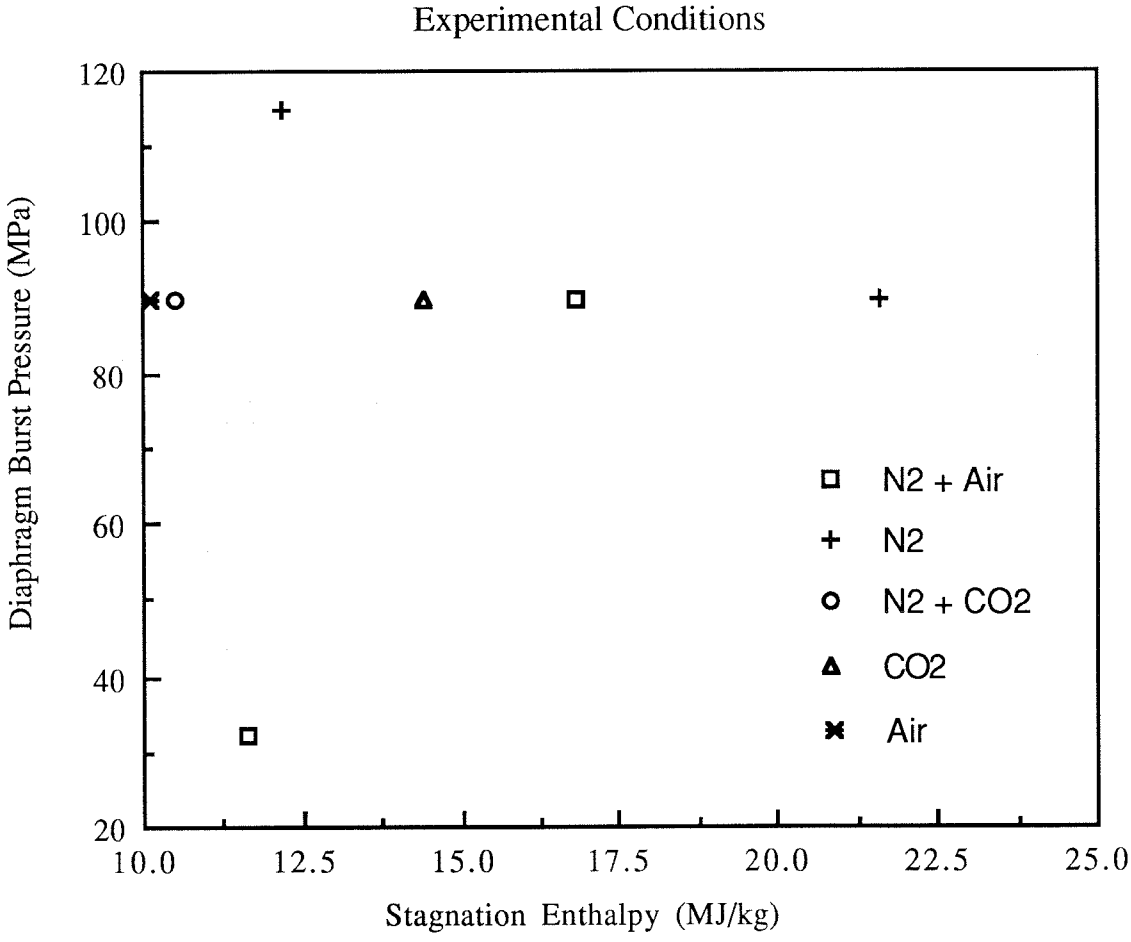

Figure 3.5. Experimental Conditions

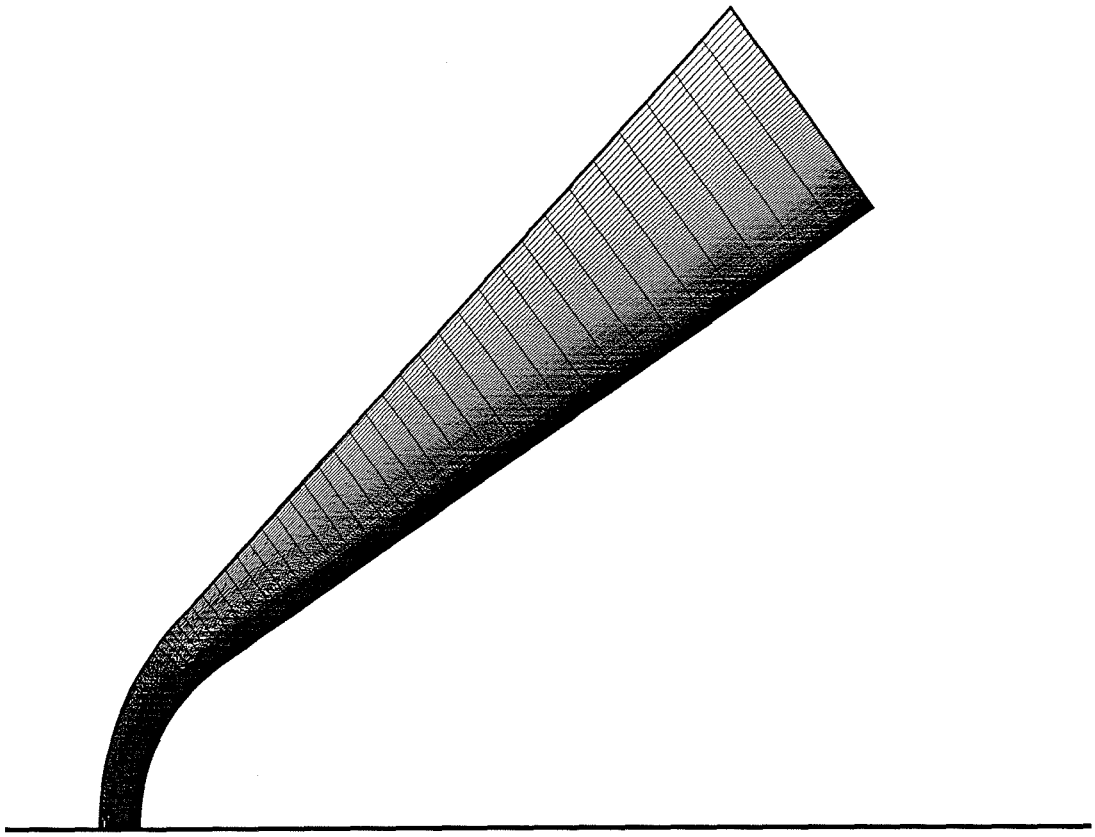

Fig. 4.1. Grid for Viscous Flow Field Computation (ymin=r/2000)

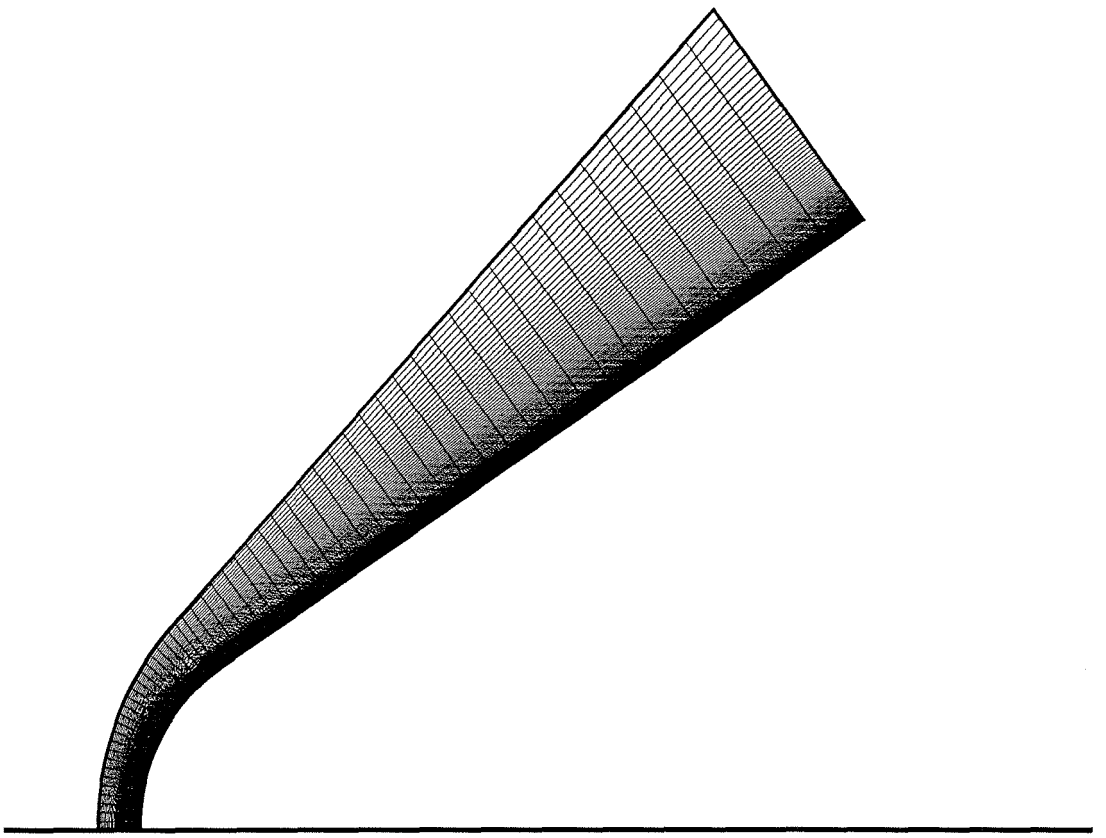

Fig. 4.2. Grid for Viscous Flow Field Computation (ymin=r/5000)

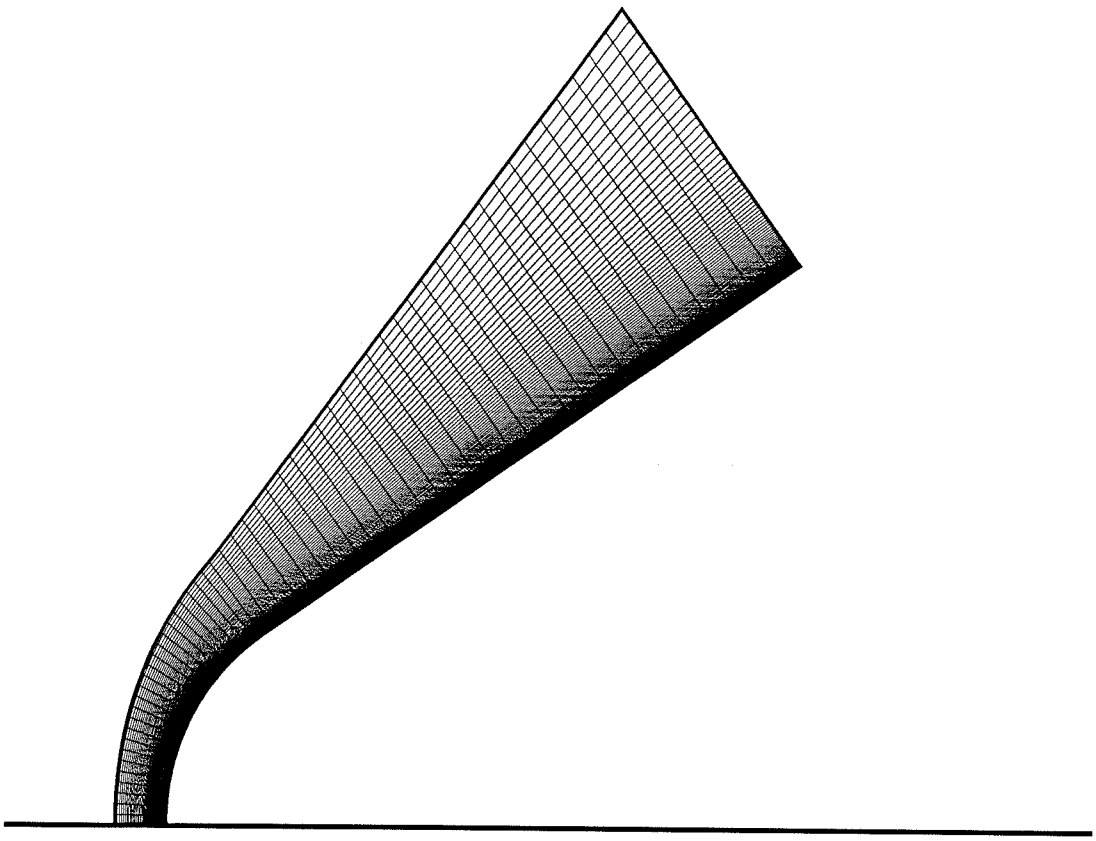

Fig. 4.3. Grid for Viscous Flow Field Computation (ymin=r/7500)

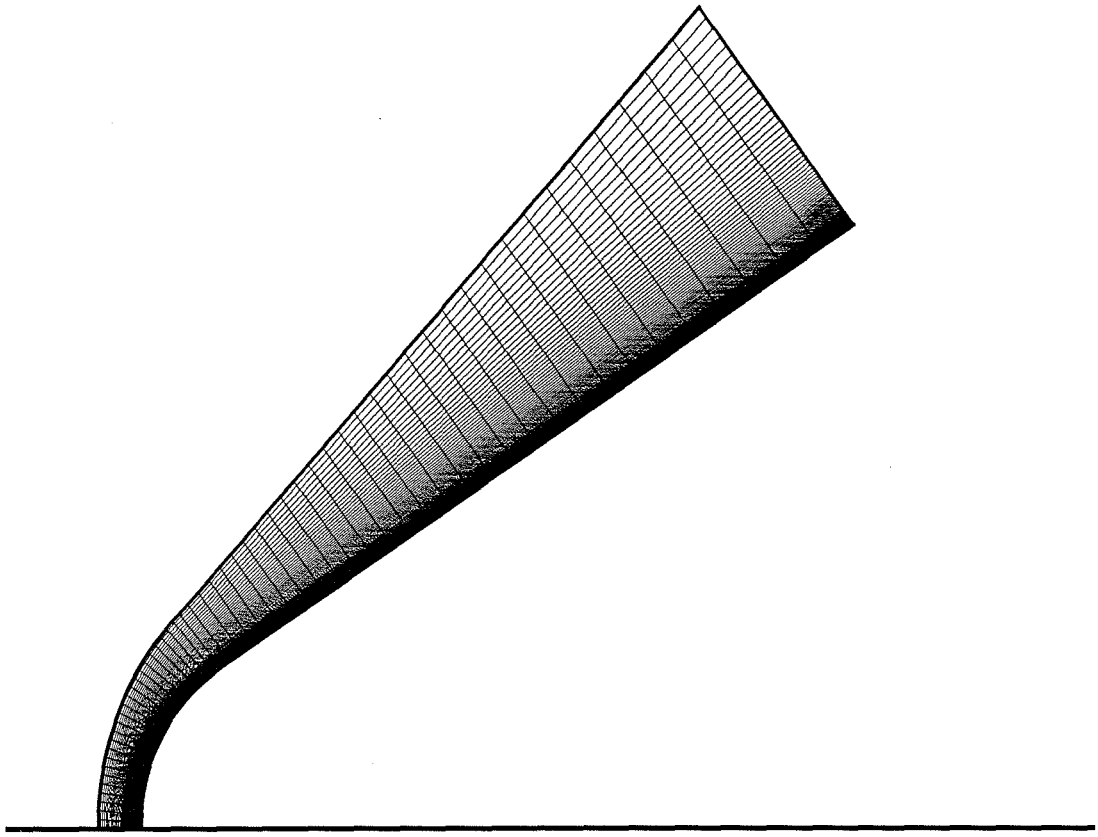

Fig. 4.4. Grid for Viscous Flow Field Computation (ymin=r/10000)

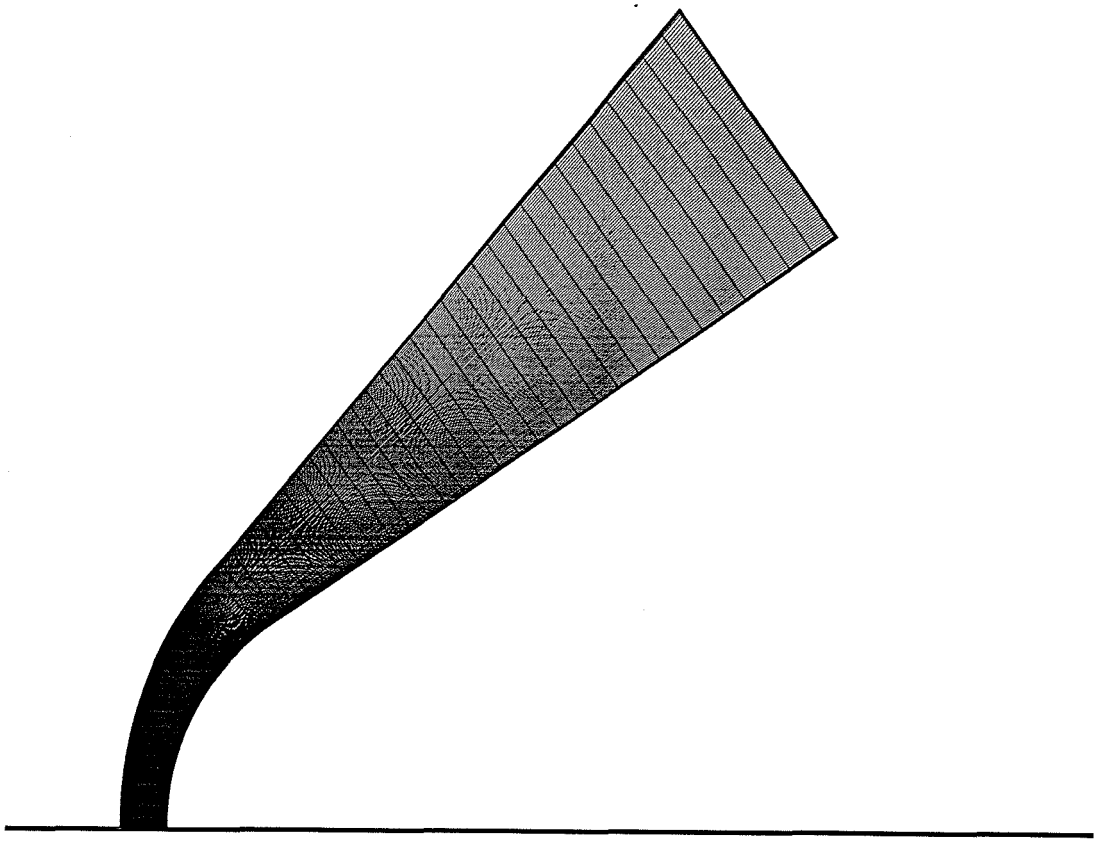

Fig. 4.5. Grid for Invisid Flow Field Computation (ymin=r/600)

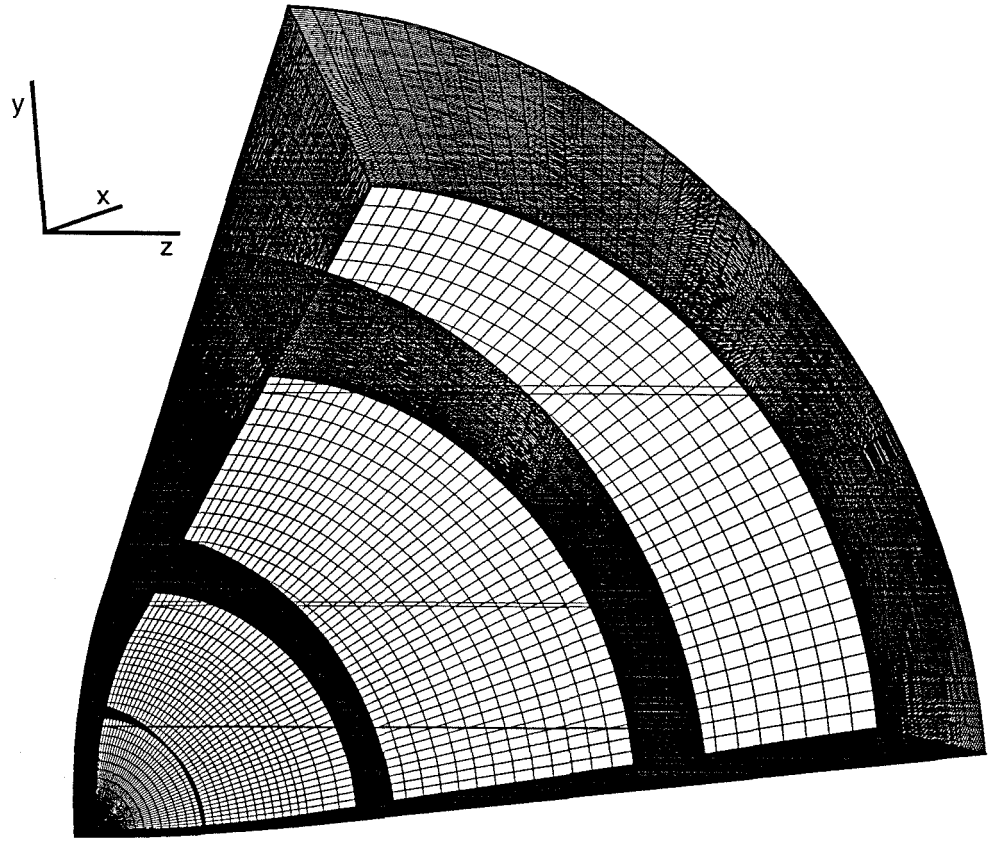

Figure 4.6. Grid for Computational Interferometry (Inviscid Case)

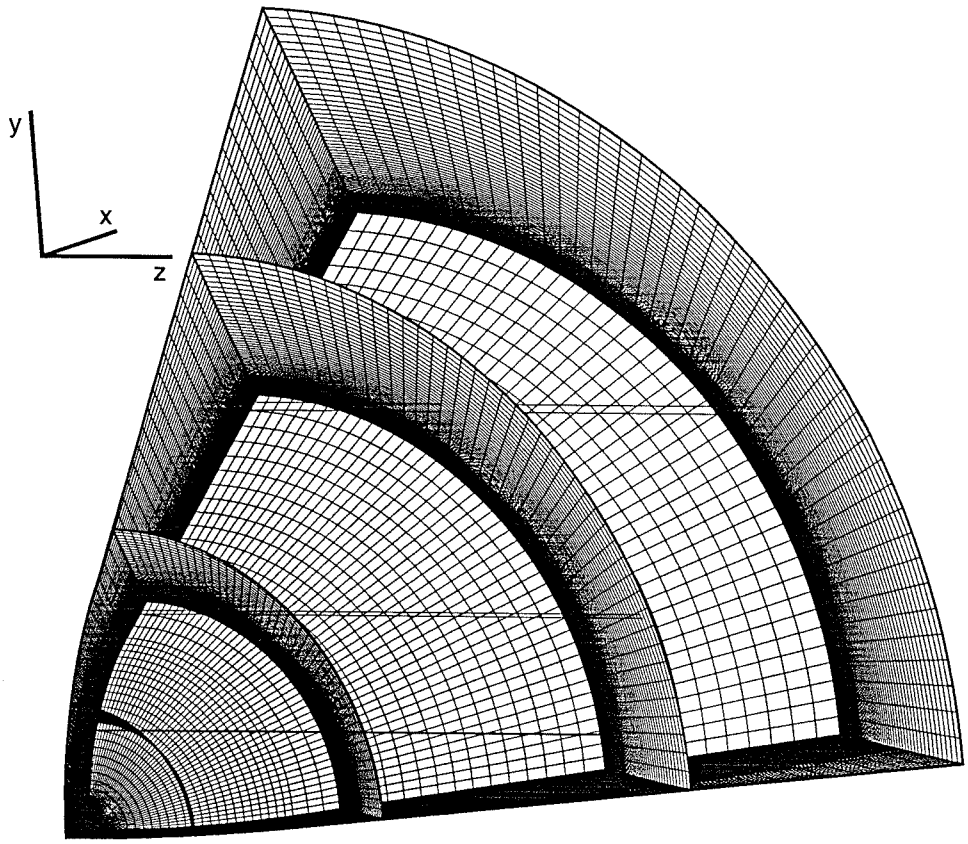

Figure 4.7. Grid for Computational Interferometry (Viscous Case)

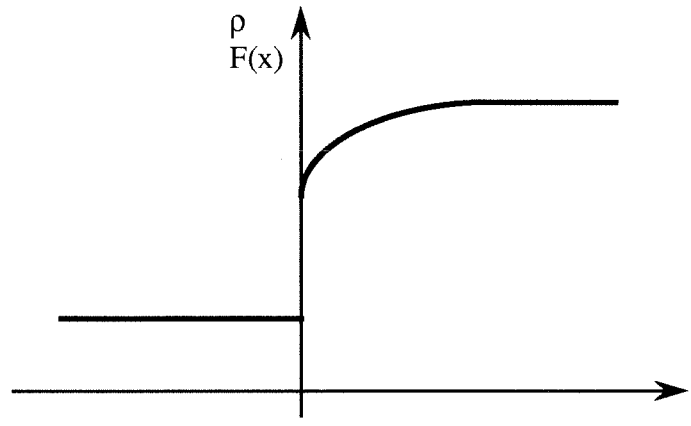

Figure 4.8 Schematic of Differntial Interferogram
(a) Density Contour and Fringe Shift of Mach-Zehnder Interferogram

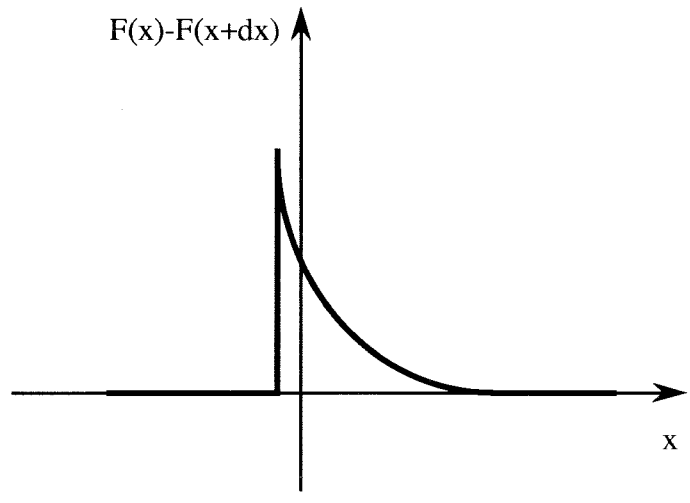

Figure 4.8 Schematic of Differential Interferogram
(b) Differential Interferogram by F(x)-F(x+dx)

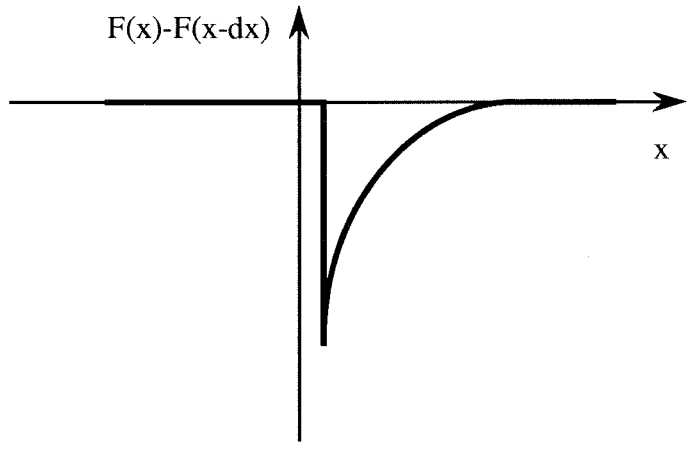

Figure 4.8 Schematic of Differential Interferogram
(c) Differential Interferogram by F(x) - F(x-dx)

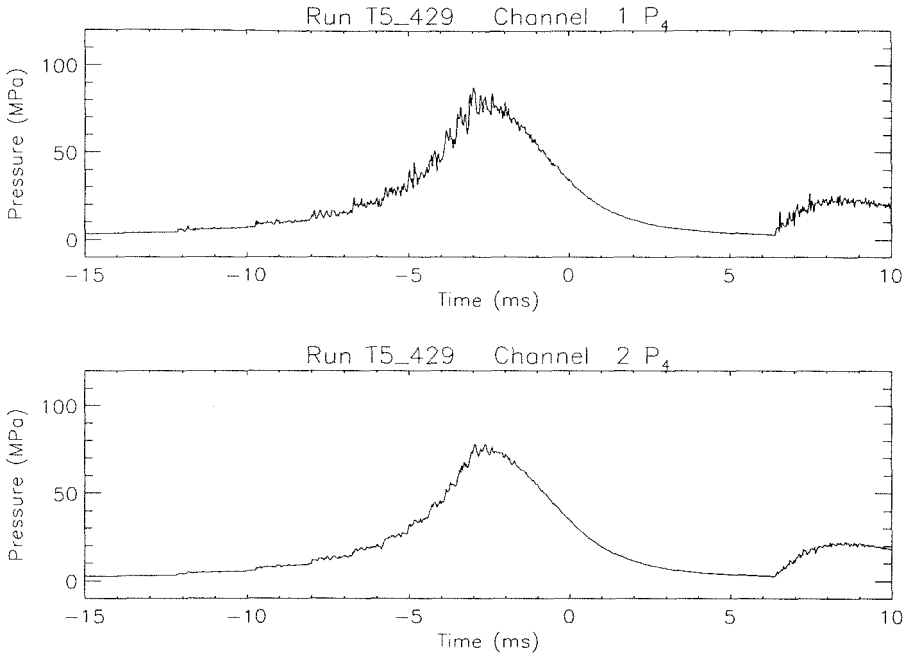

Fig. 5.1. Example of Pressure History at the End of the Compression Tube

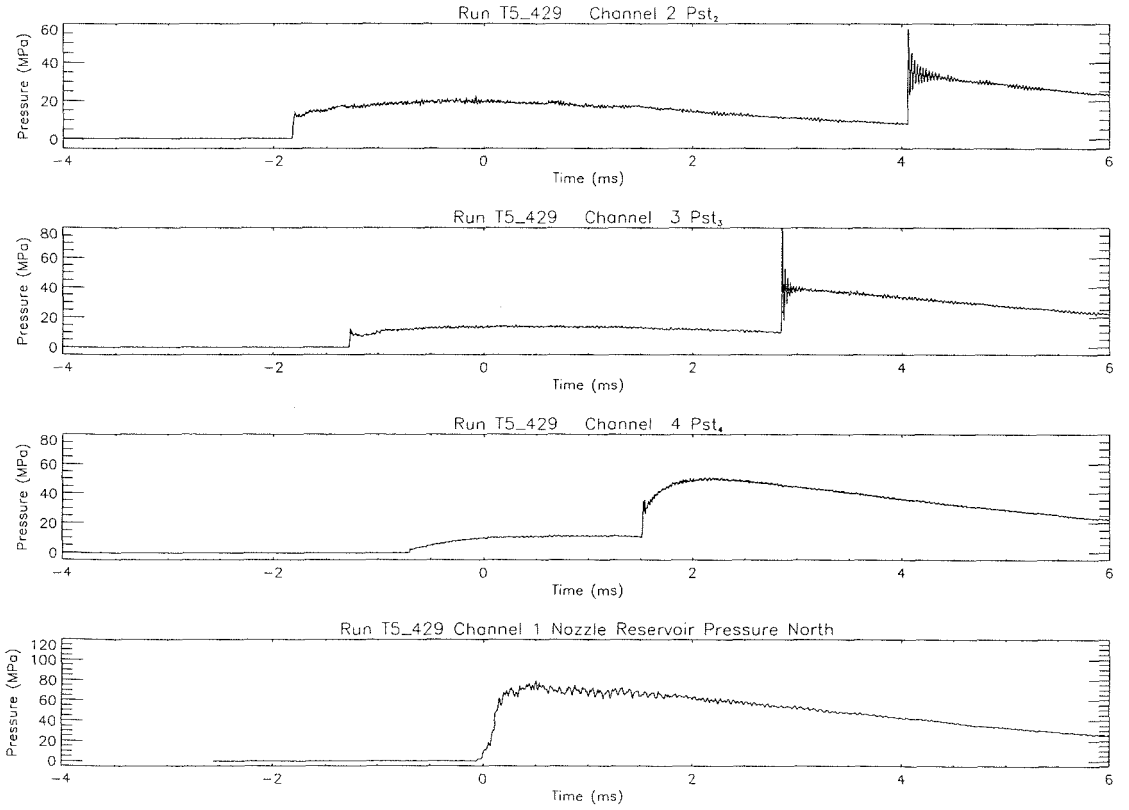

Fig. 5.2. Example of Pressure History in the Shock Tube

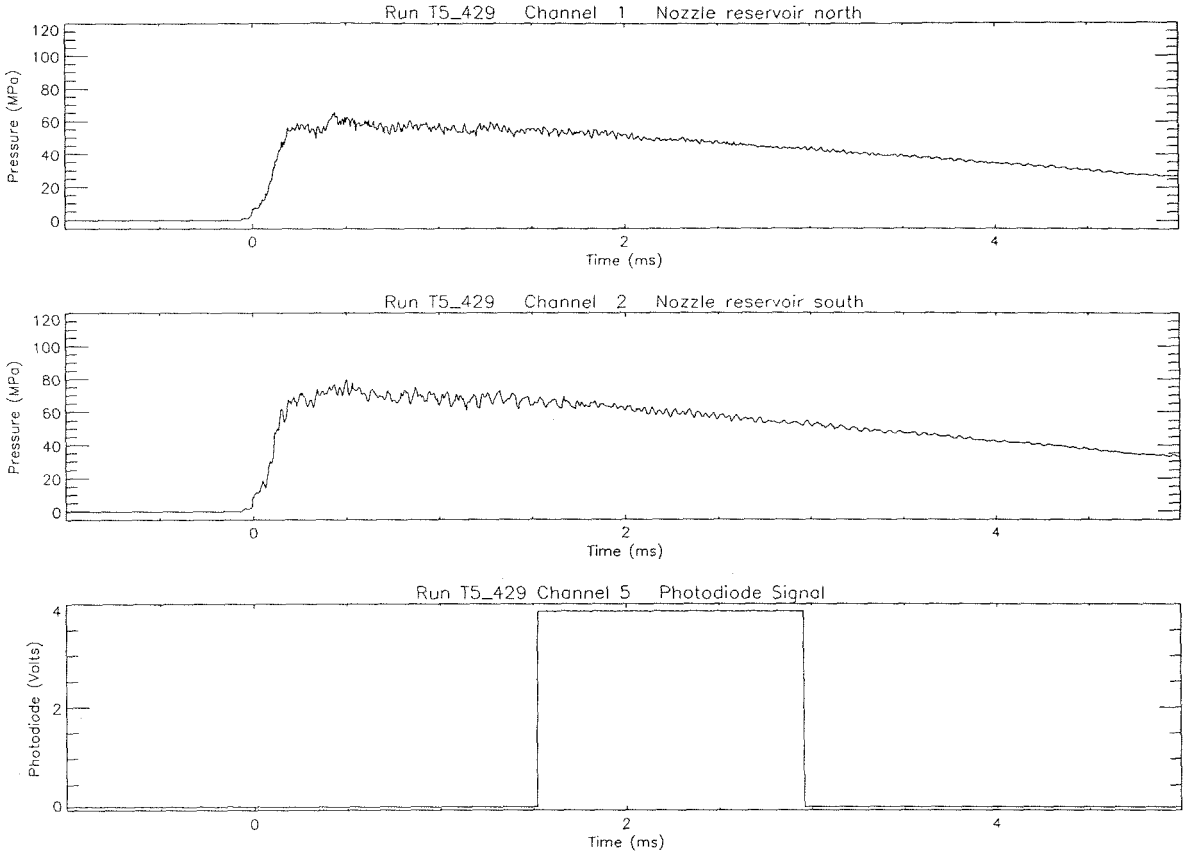

Fig. 5.3. Example of Pressure History at Nozzle Reservoir

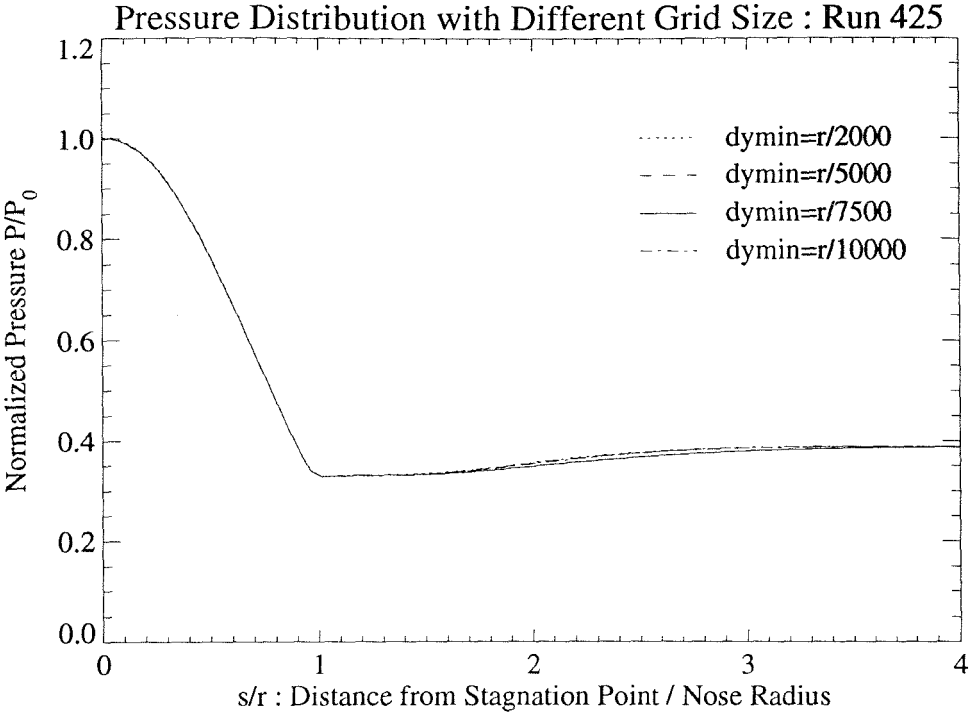

Fig. 5.4. Pressure Distribution with Different Grid Size

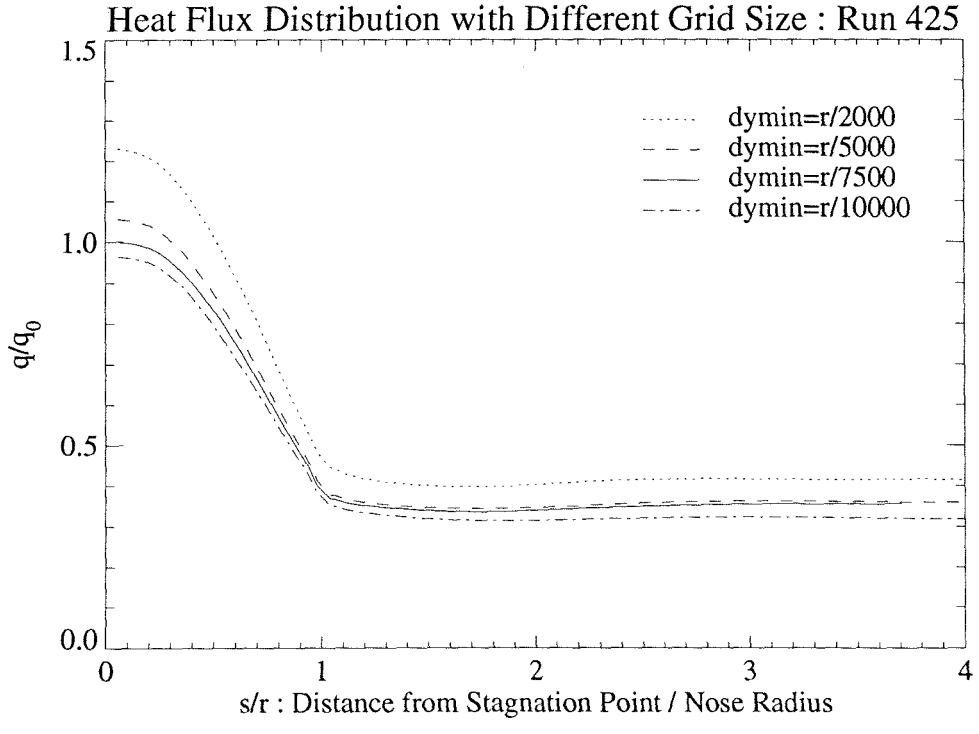

Fig. 5.5. Heat Flux Distribution with Different Grid Size

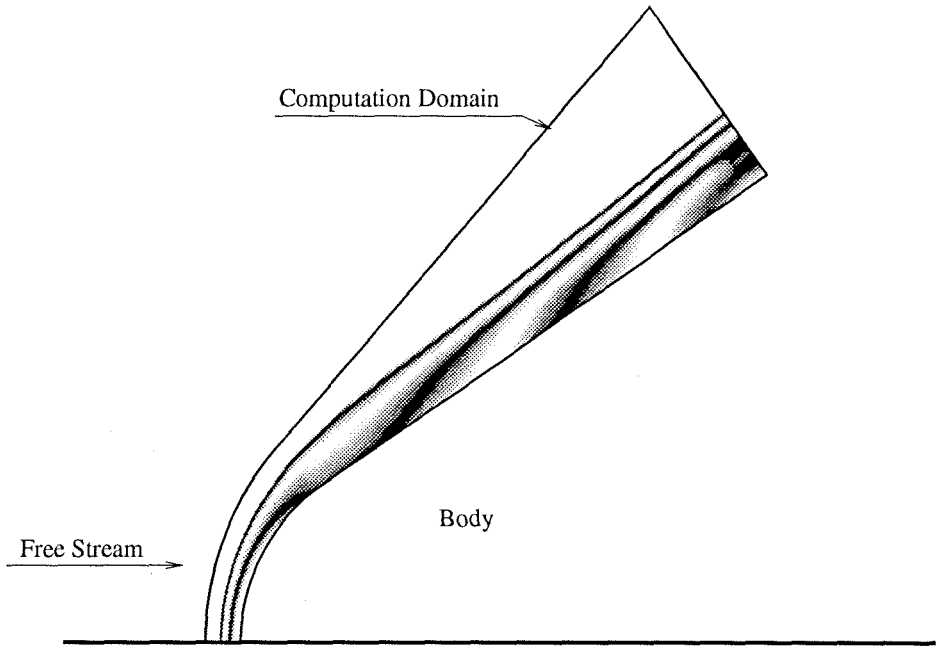

Fig. 5.6. Example of Computational Mach-Zehnder Interferogram (Run 425)

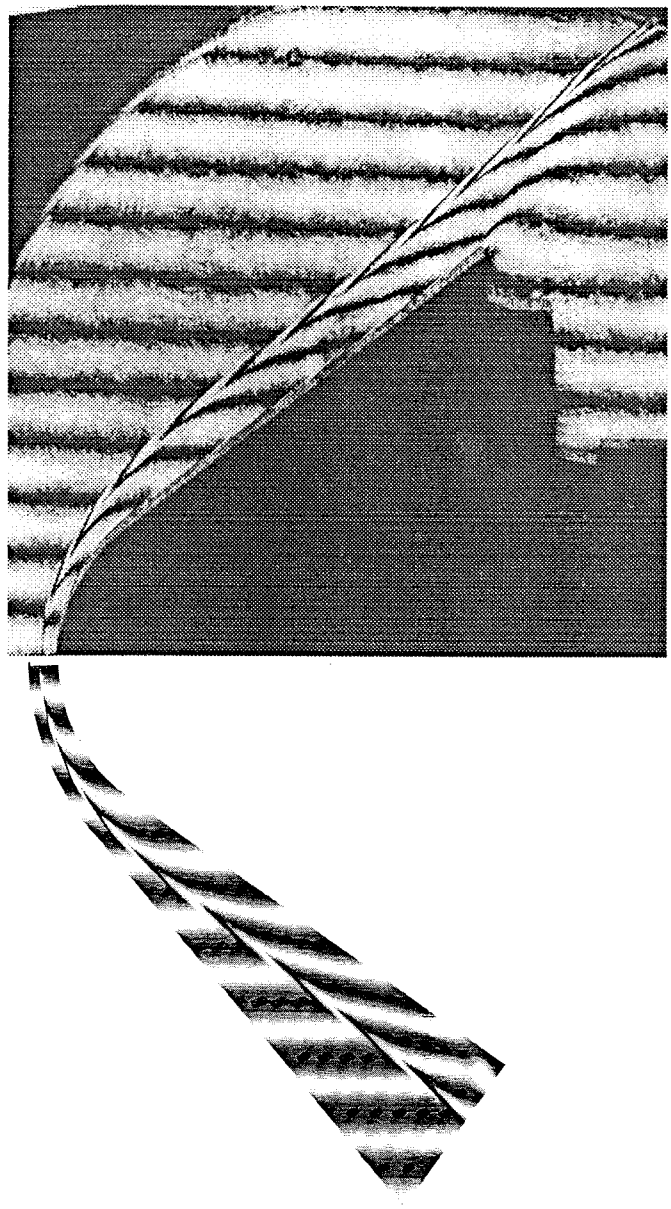

Figure 5.7. Comparison of Experimental and Computational Differential Interferograms (Run425; Above : Experiment , Below : Computational)

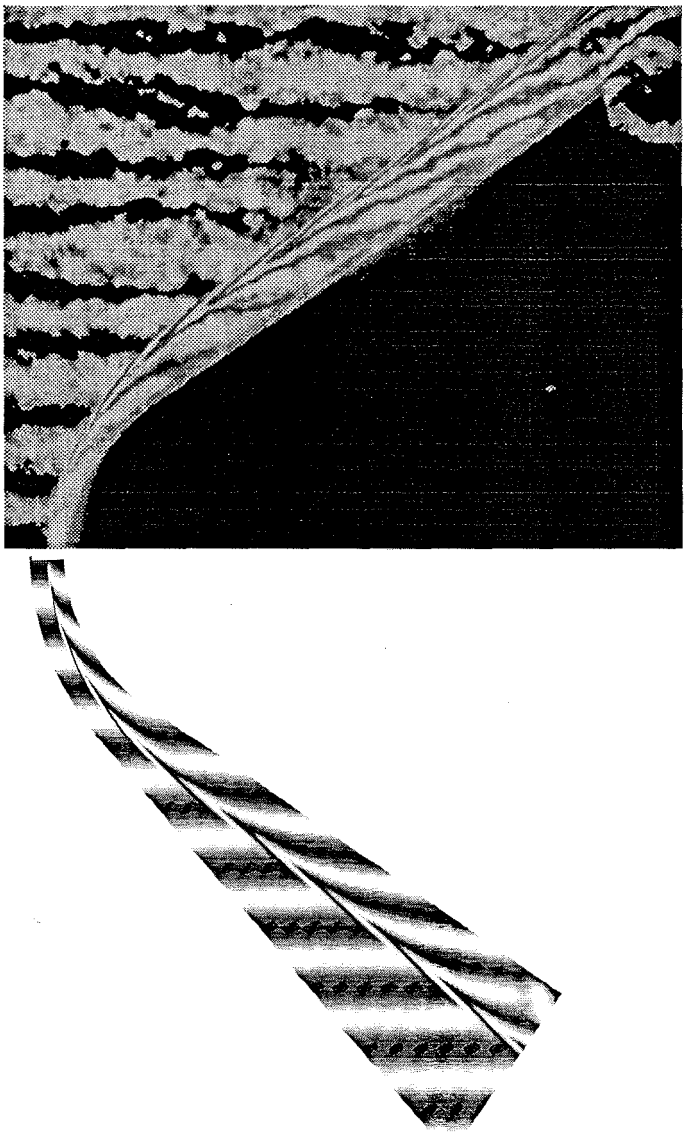

Figure 5.8. Comparison of Experimental and Computational Differential Interferograms (Run435; Above : Experiment , Below : Computational)

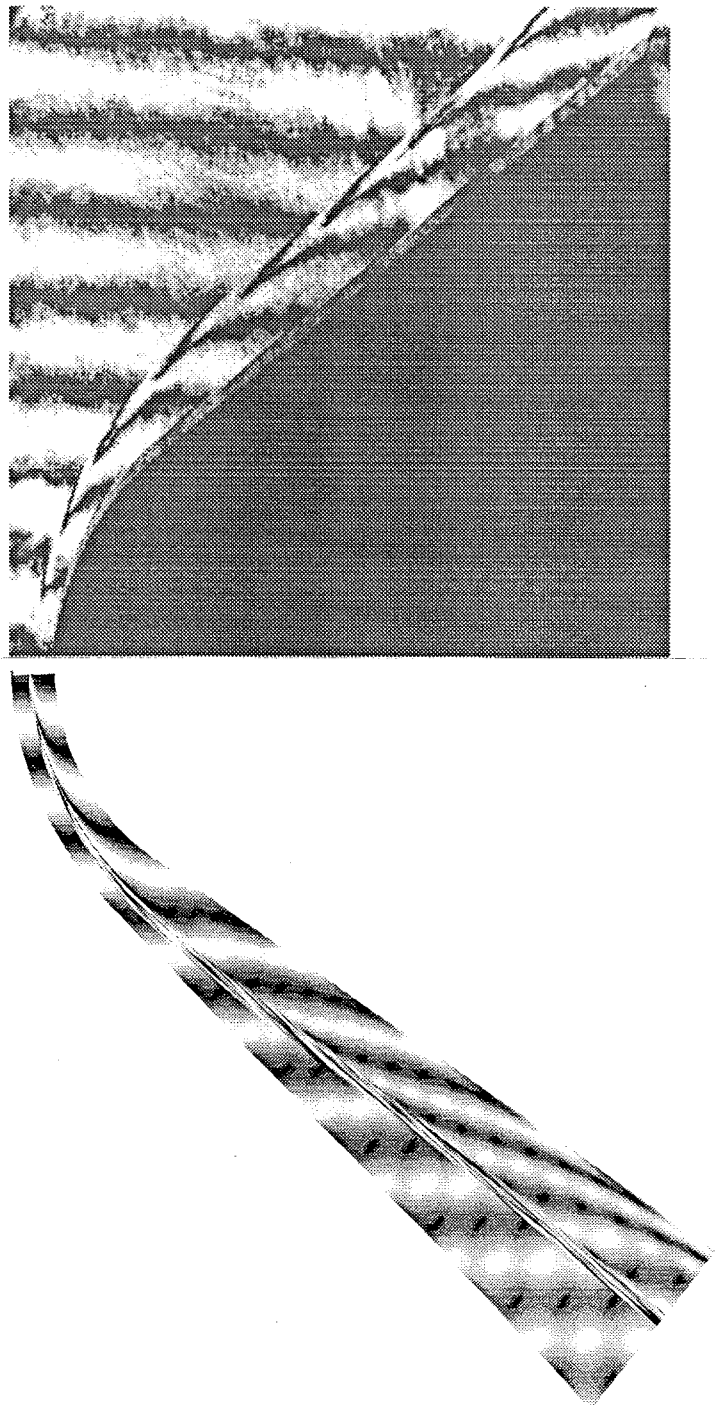

Figure 5.9. Comparison of Experimental and Computational Differential Interferograms (Run428; Above : Experiment , Below : Computational)

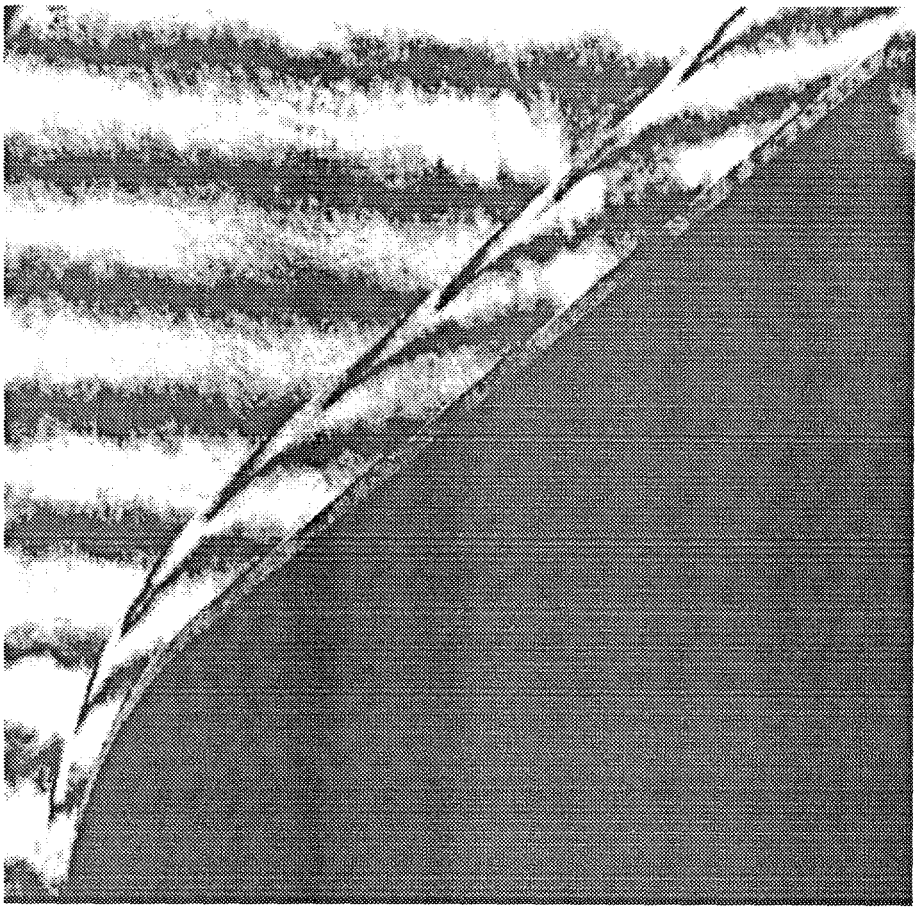

Figure 5.10. Experimental Differential Interferogram (Run 445)

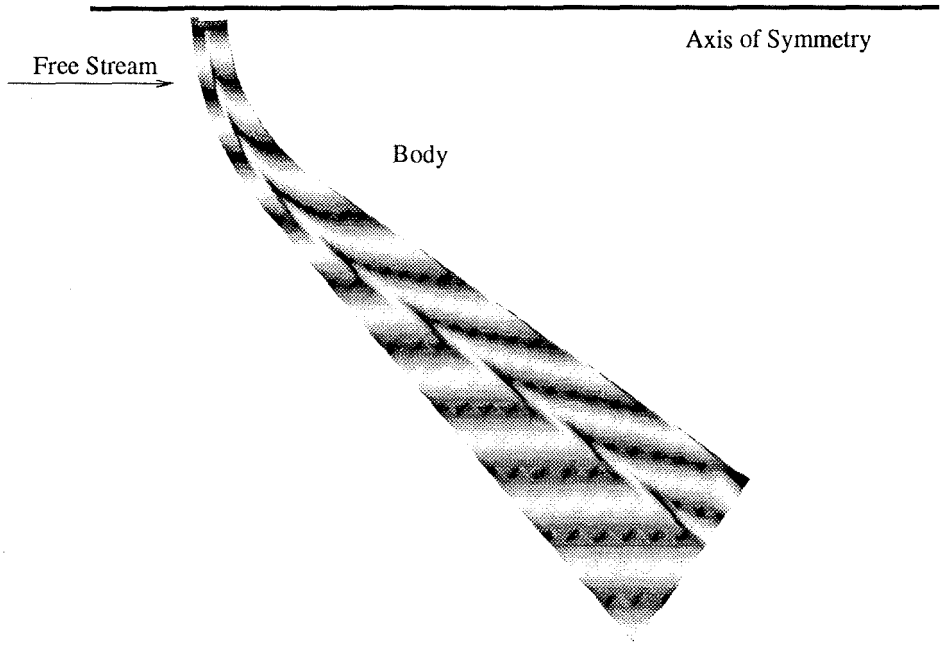

Figure 5.11. Computational Differential Interferogram based on Viscous Solution

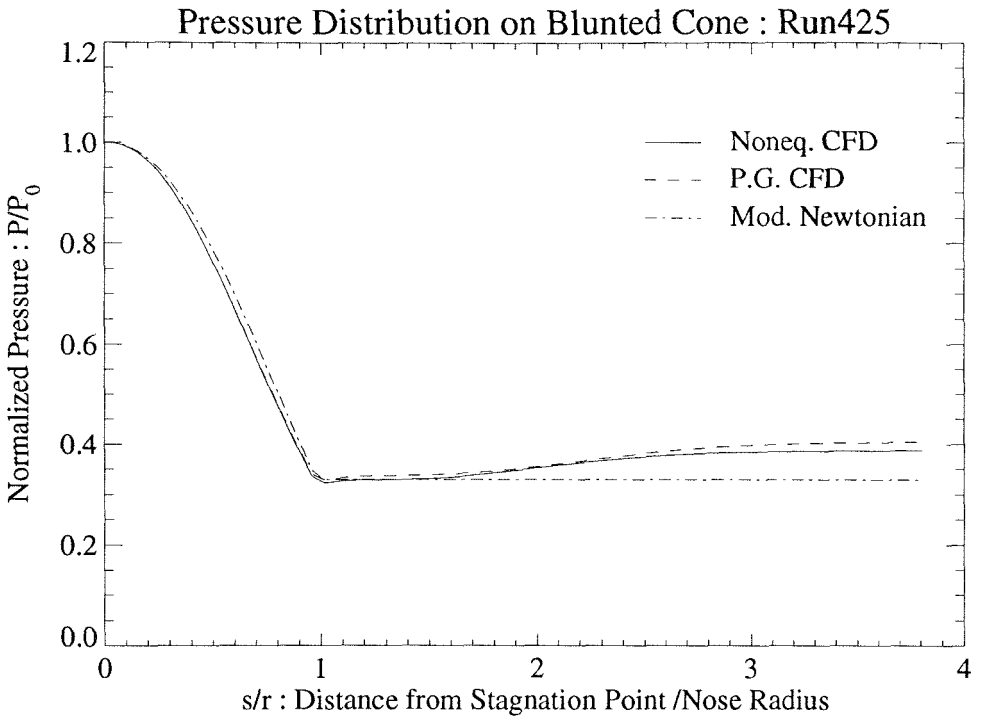

Fig. 5.12. Computed Pressure Profile (Run425)

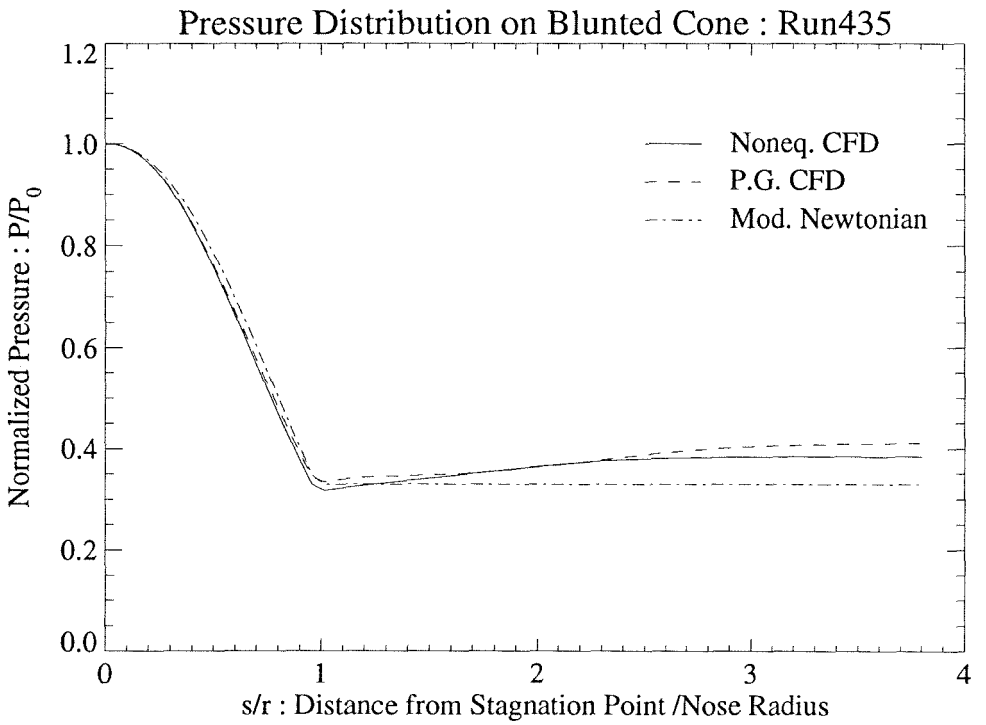

Fig. 5.13. Computed Pressure Profile (Run435)

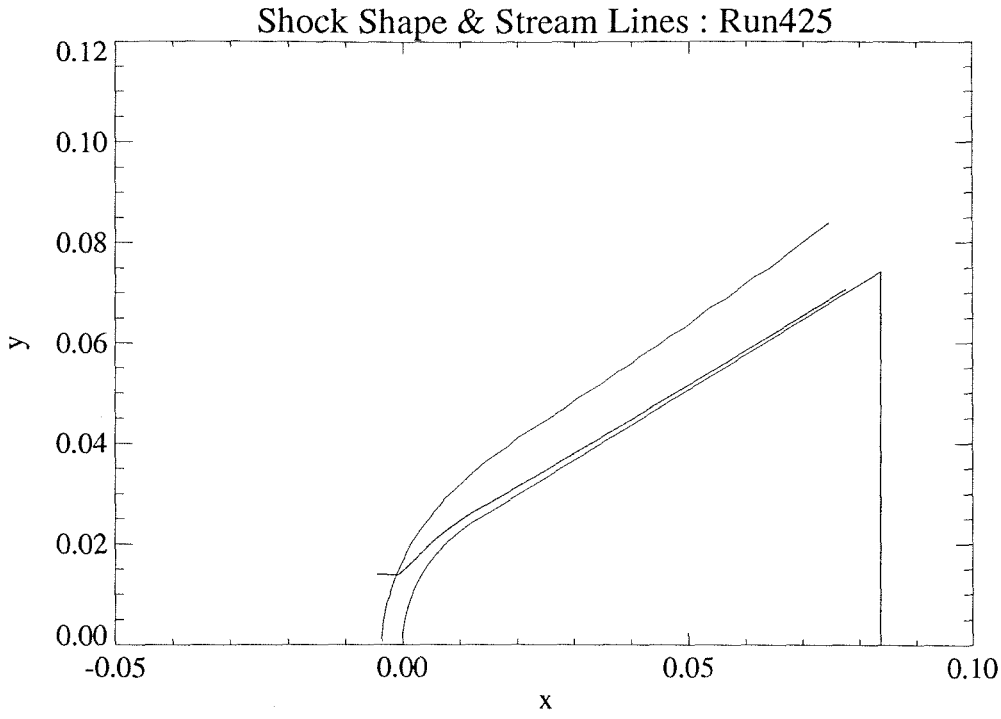

Fig. 5.14. Streamline from ix=12 and Shock Shape (Run 425)

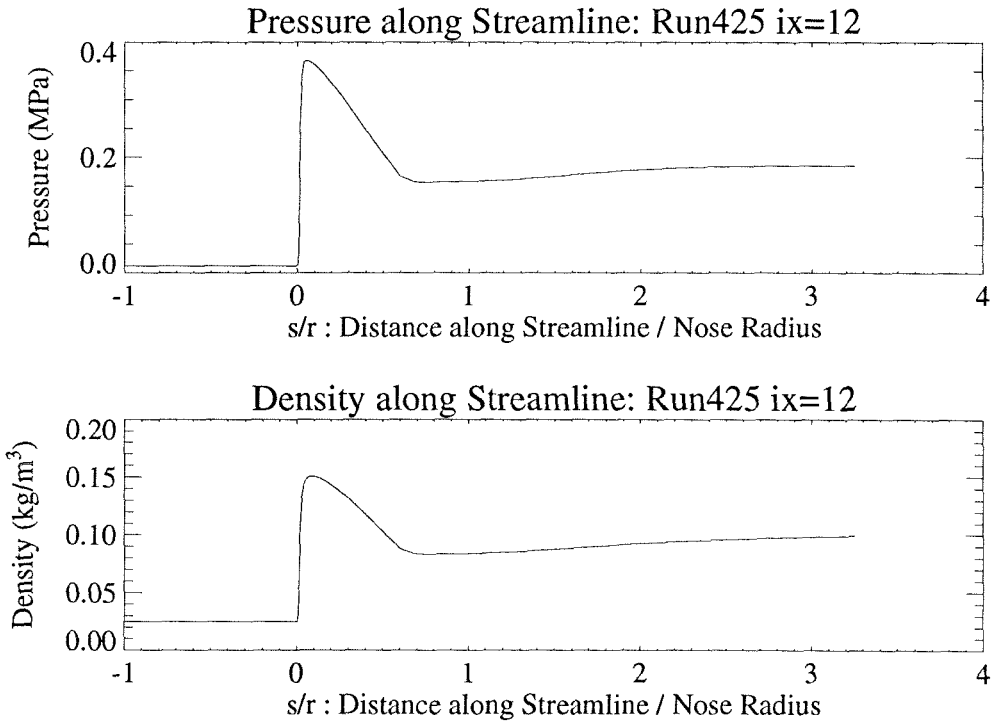

Fig. 5.15. Pressure and Density along Streamline (Run425)

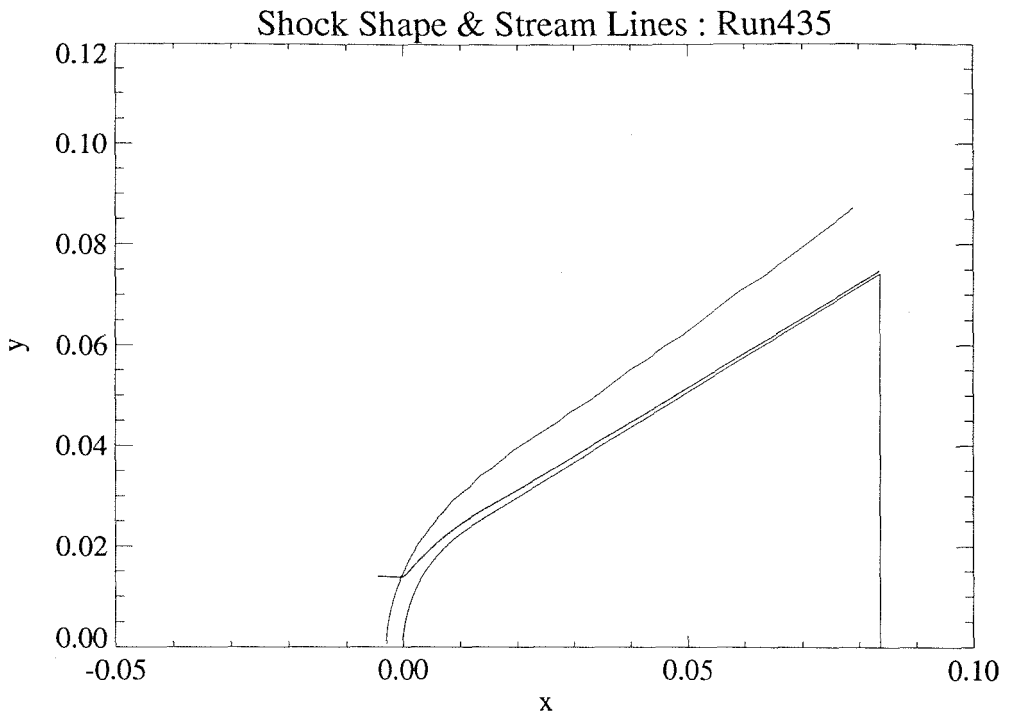

Fig. 5.16. Streamline from ix=12 and Shock Shape (Rnu 435)

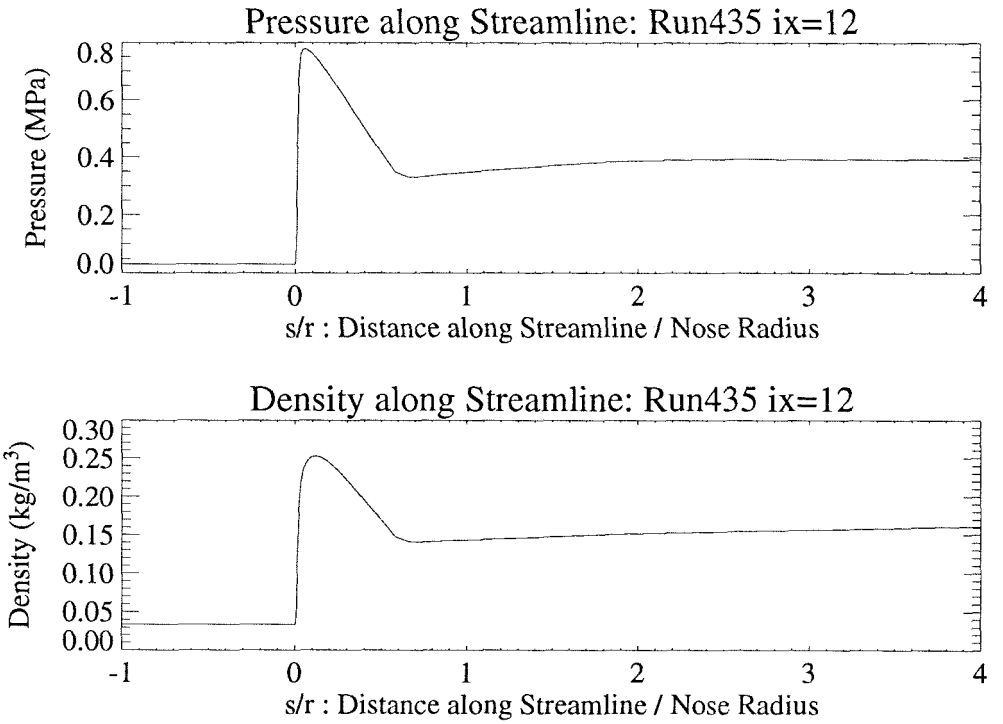

Fig. 5.17. Pressure and Density along Streamline (Run435)

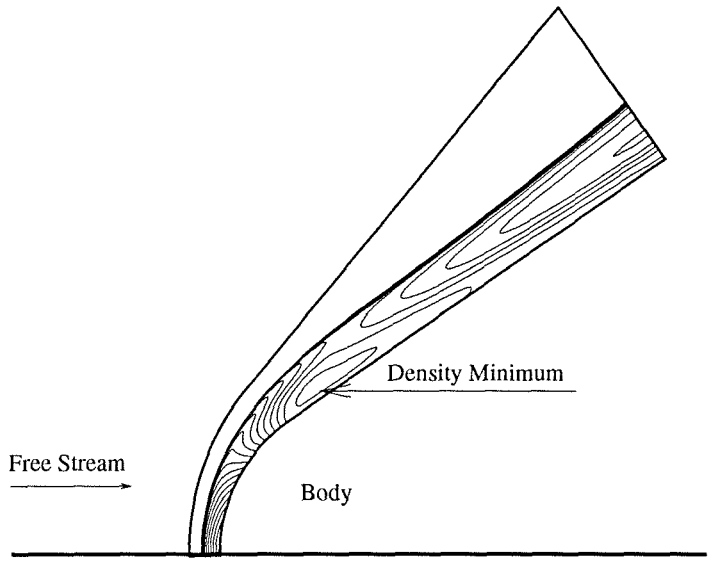

(a) Nonequilibrium Case

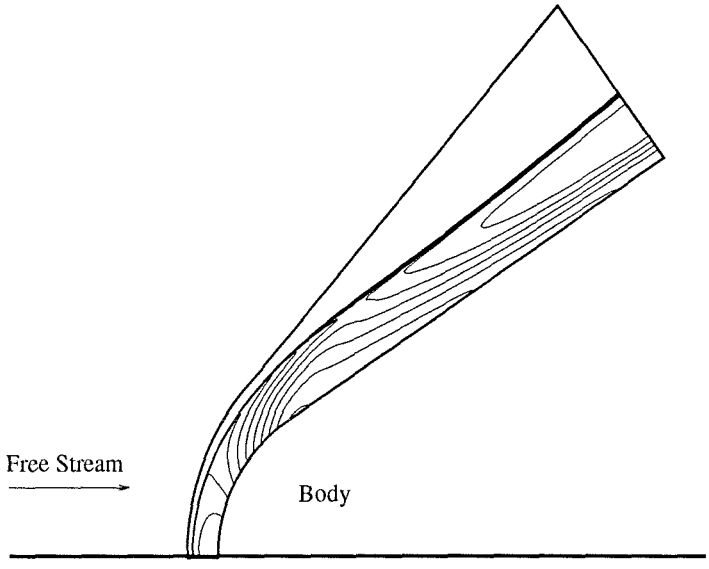

(b) Frozen Case

Fig. 5.18. Computed Density Profile (Run 425)

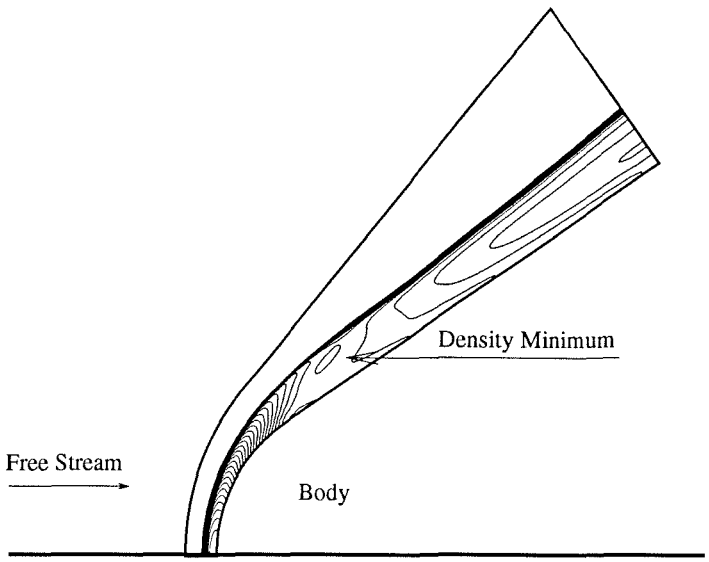

(a) Nonequilibrium Case

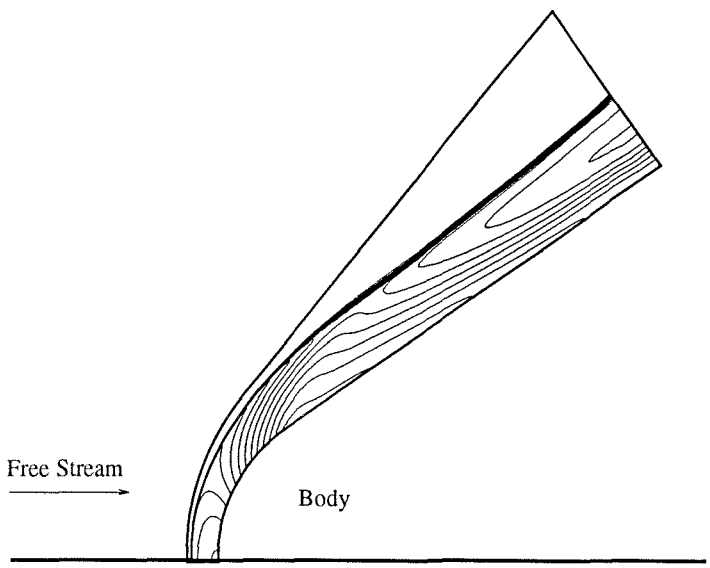

(b) Frozen Case

Fig. 5.19. Computed Density Profile (Run 435)

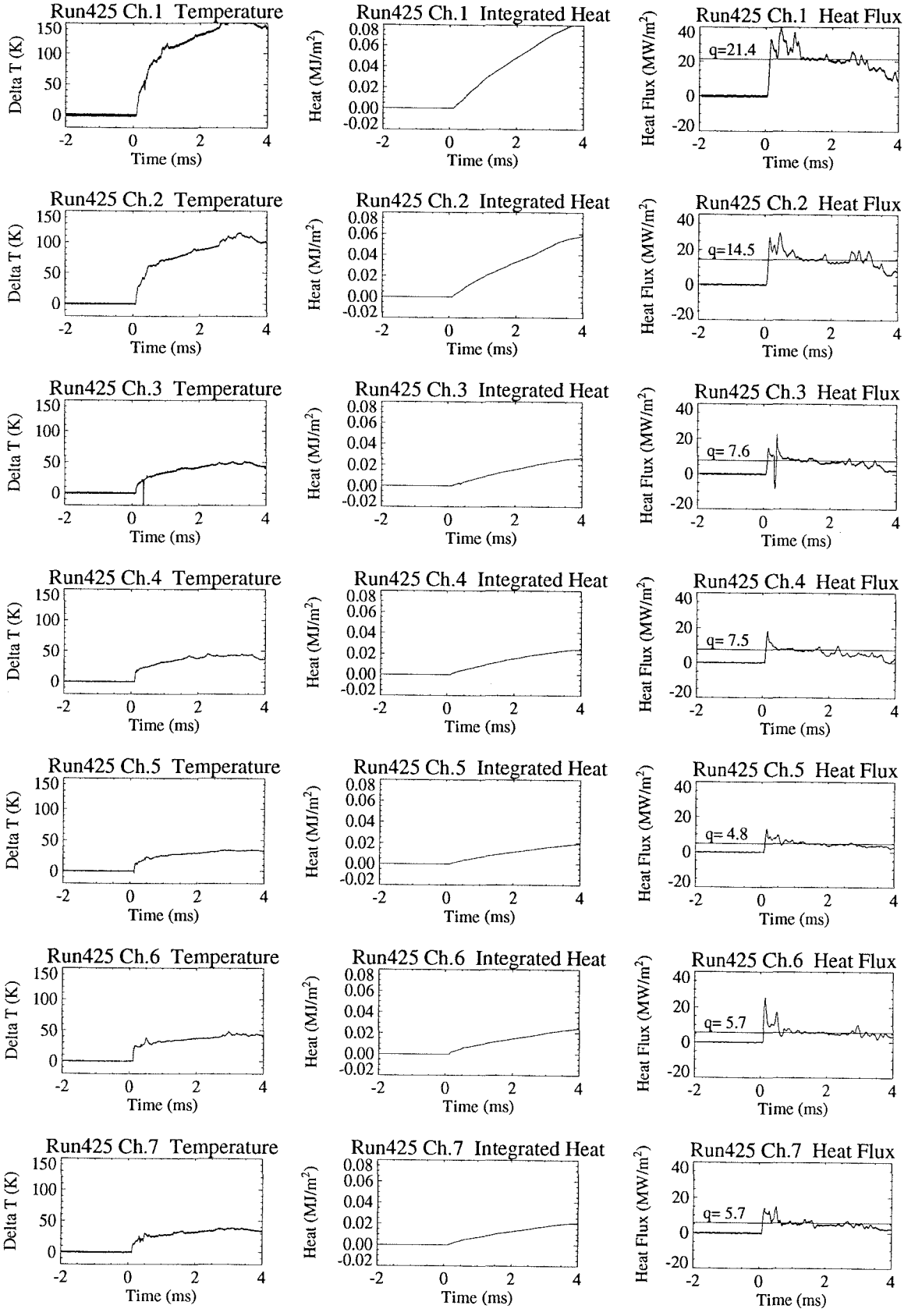

Fig. 5.20. Heat Flux Measurement Result in Nitrogen (Run425)

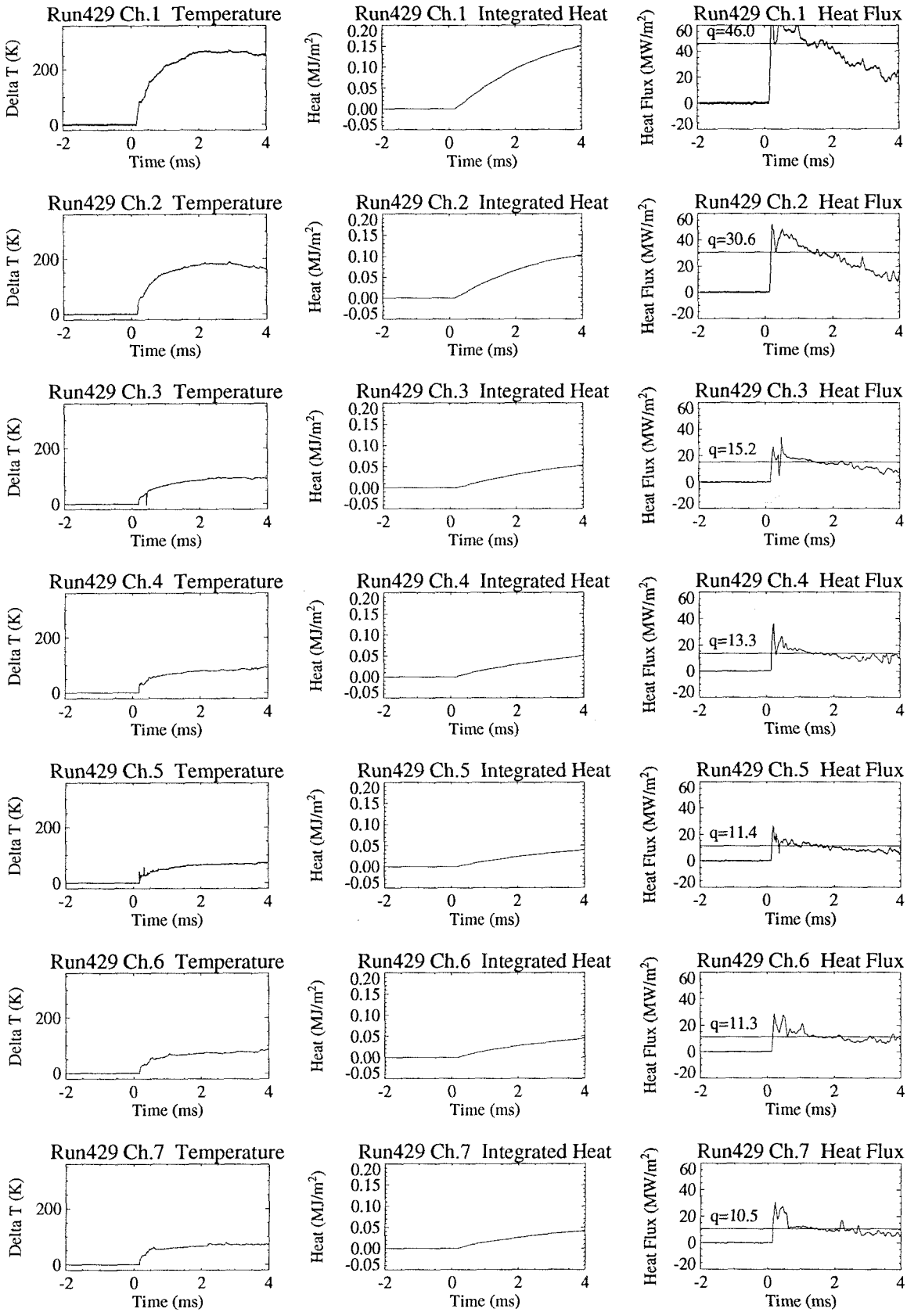

Fig. 5.21. Heat Flux Measurement Result in Nitrogen (Run429)

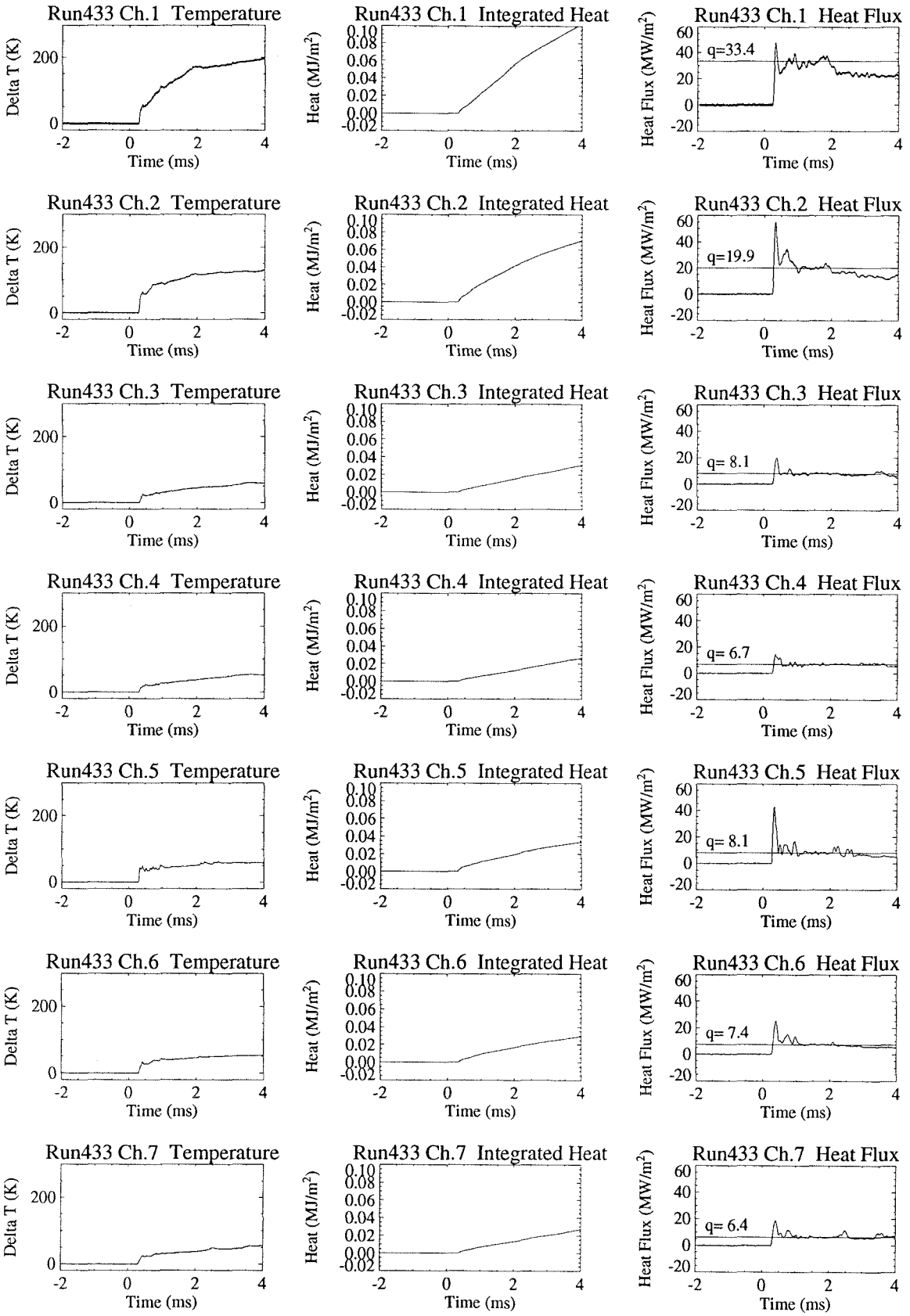

Fig. 5.22. Heat Flux Measurement Result in Nitrogen (Run433)

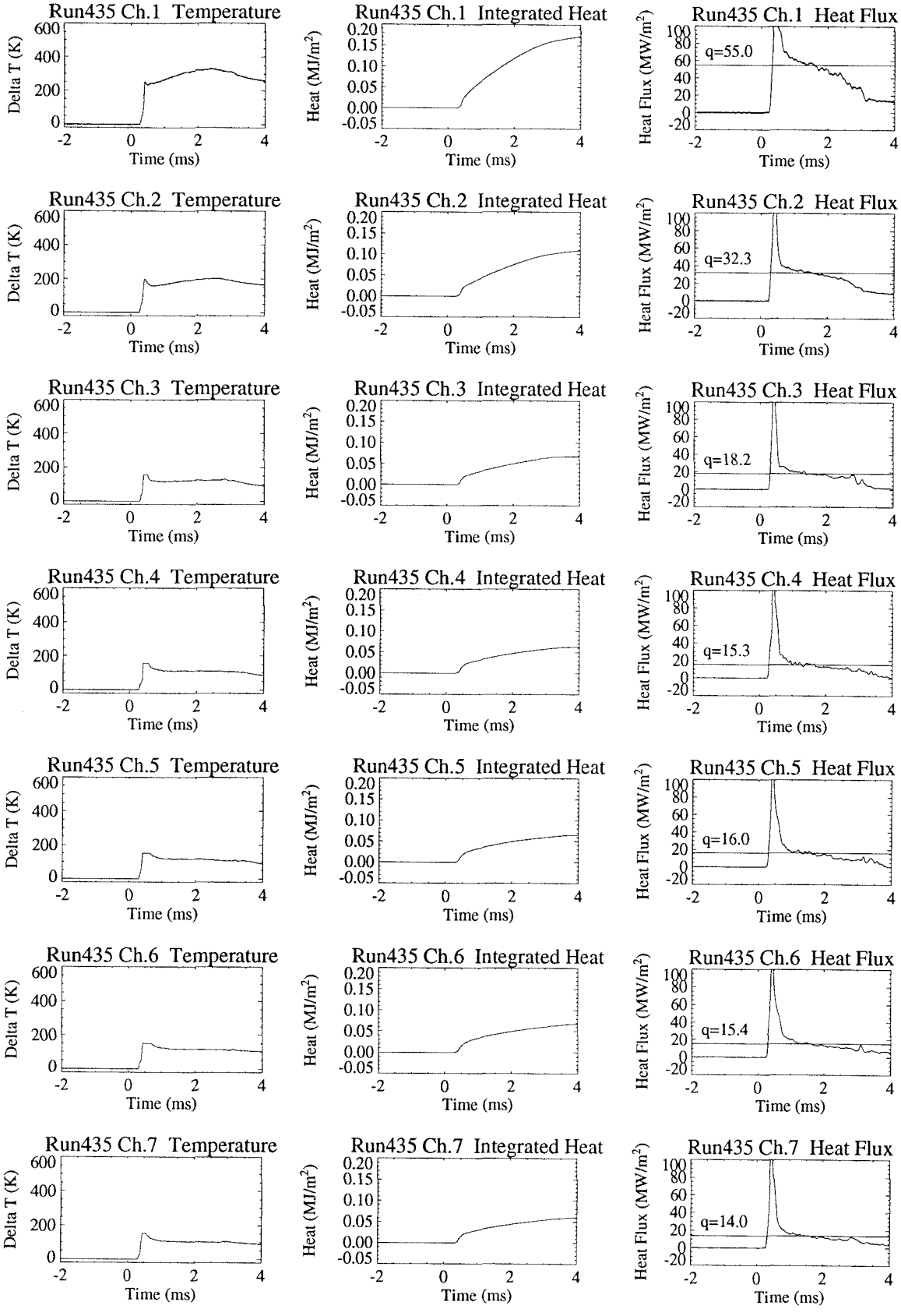

Fig. 5.23. Heat Flux Measurement Result in Nitrogen (Run435)

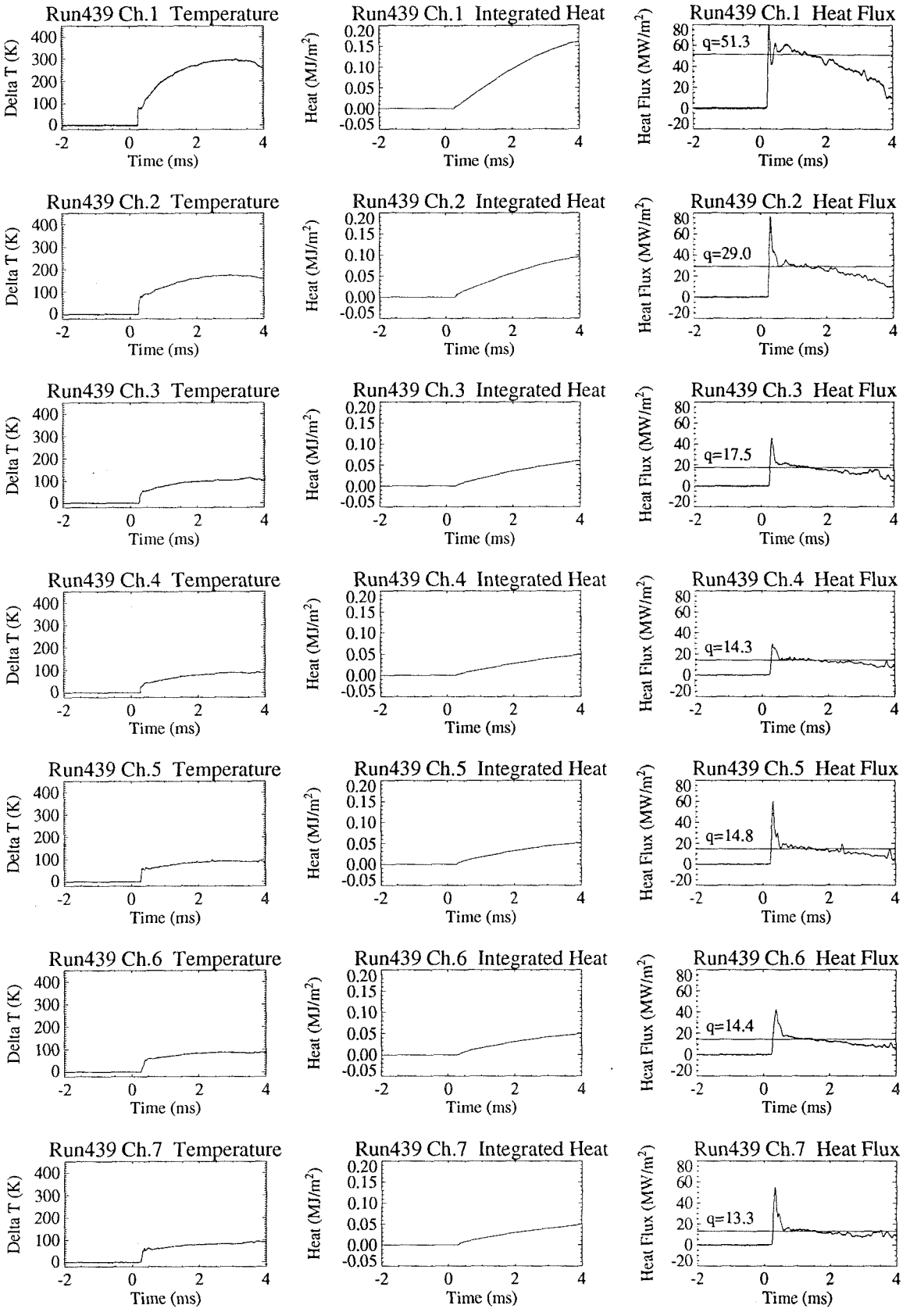

Fig. 5.24. Heat Flux Measurement Result in Nitrogen (Run439)

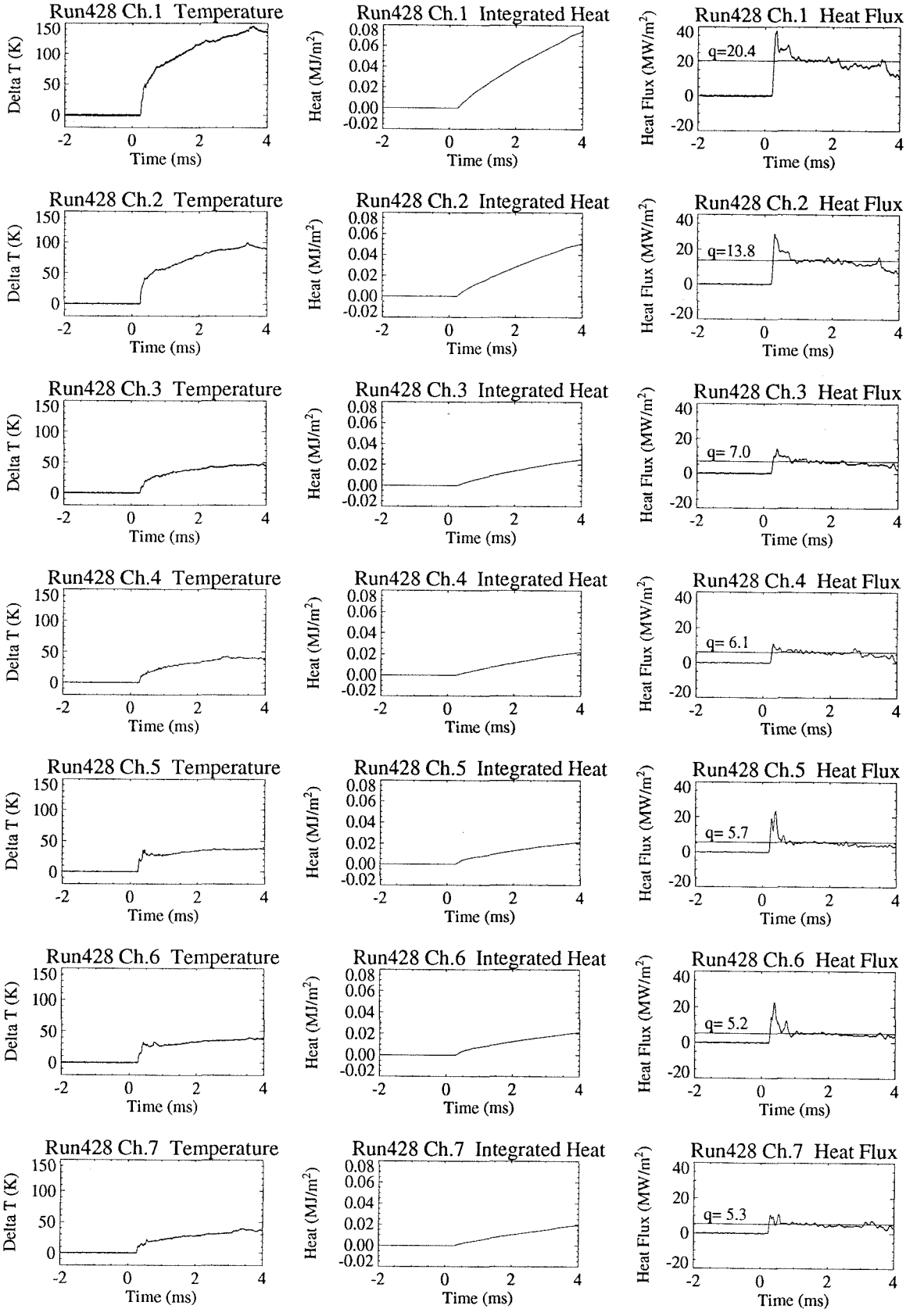

Fig. 5.25. Heat Flux Measurement Result in Air (Run428)

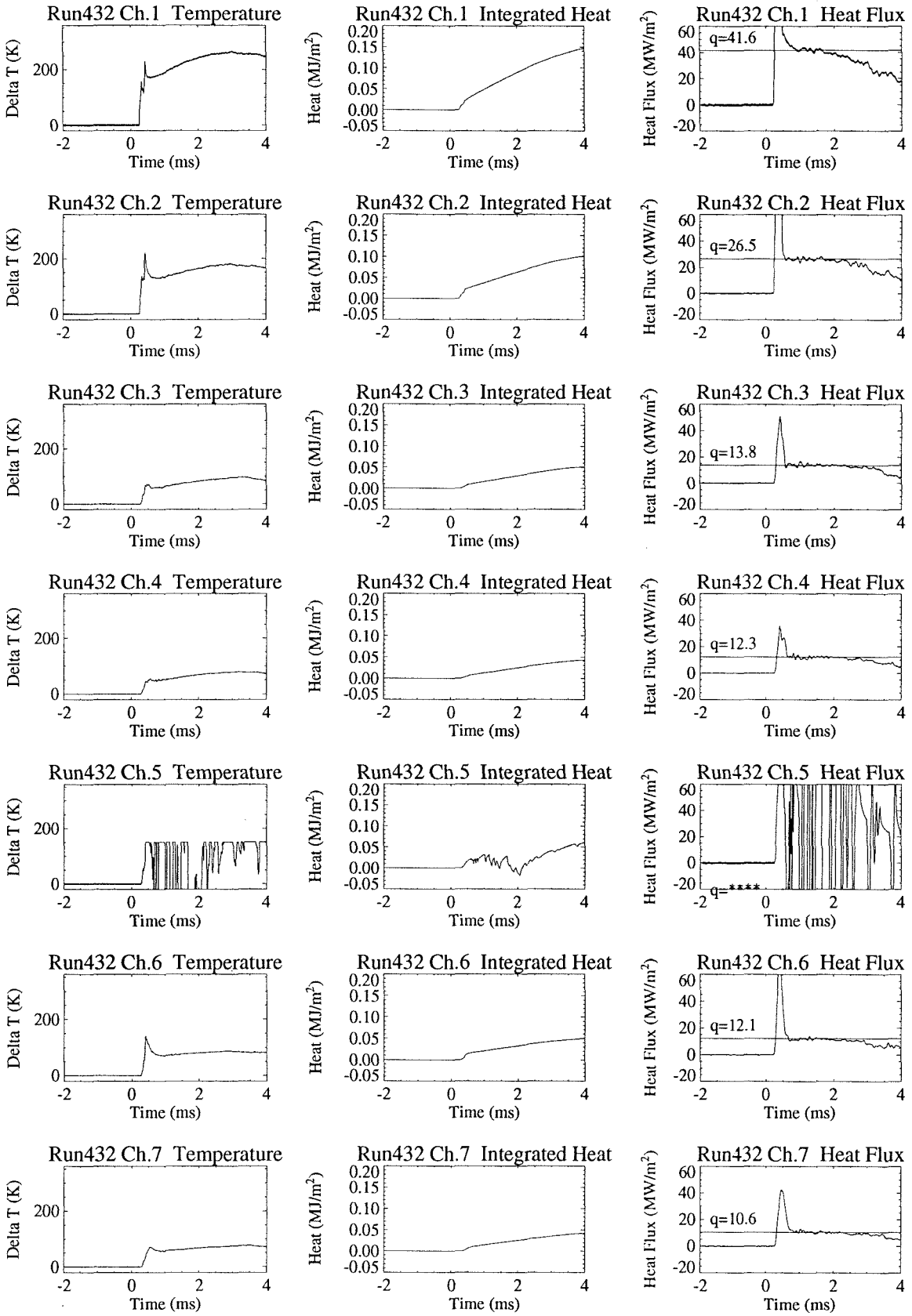

Fig. 5.26. Heat Flux Measurement Result in Air (Run432)

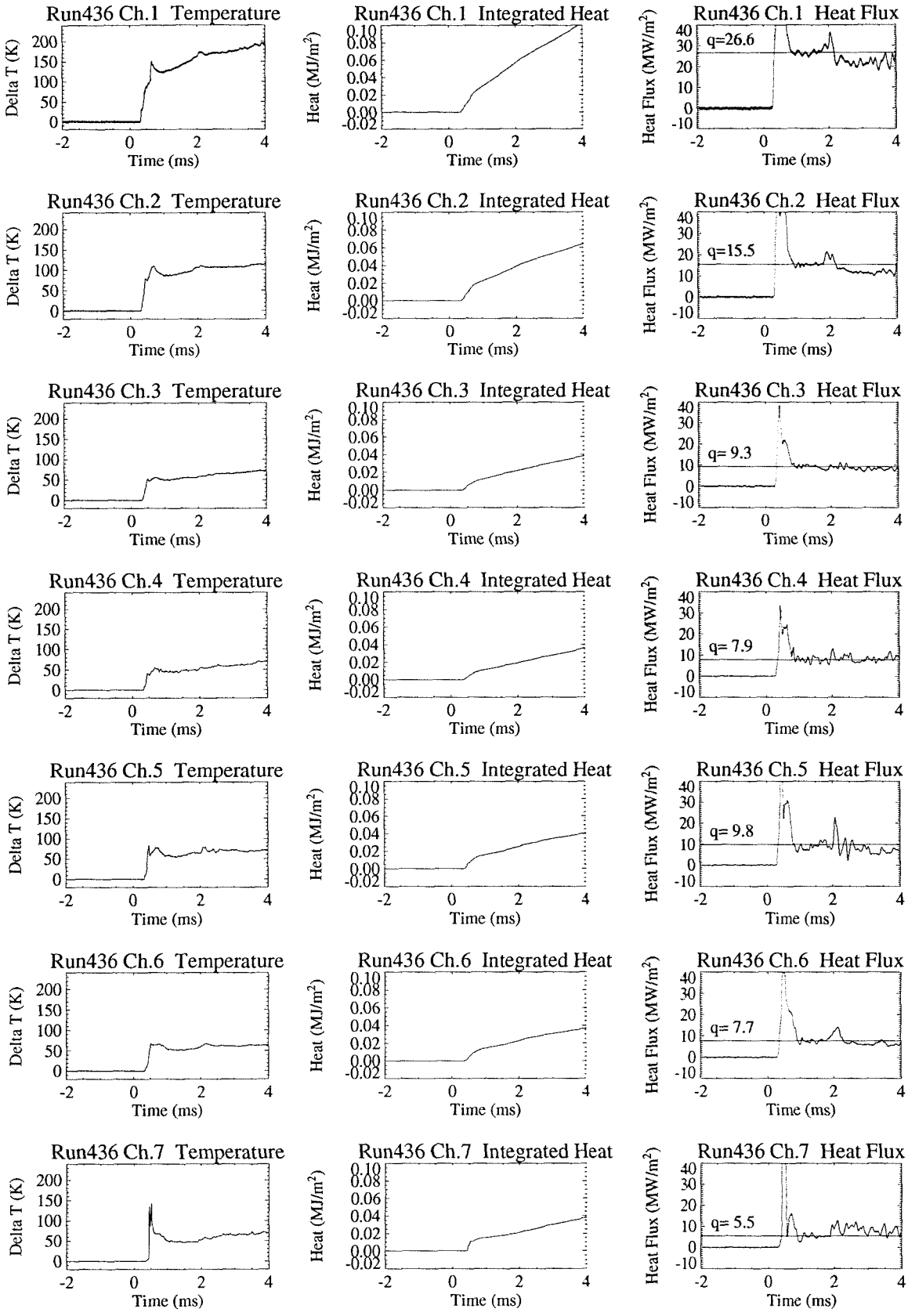

Fig. 5.27. Heat Flux Measurement Result in Air (Run436)

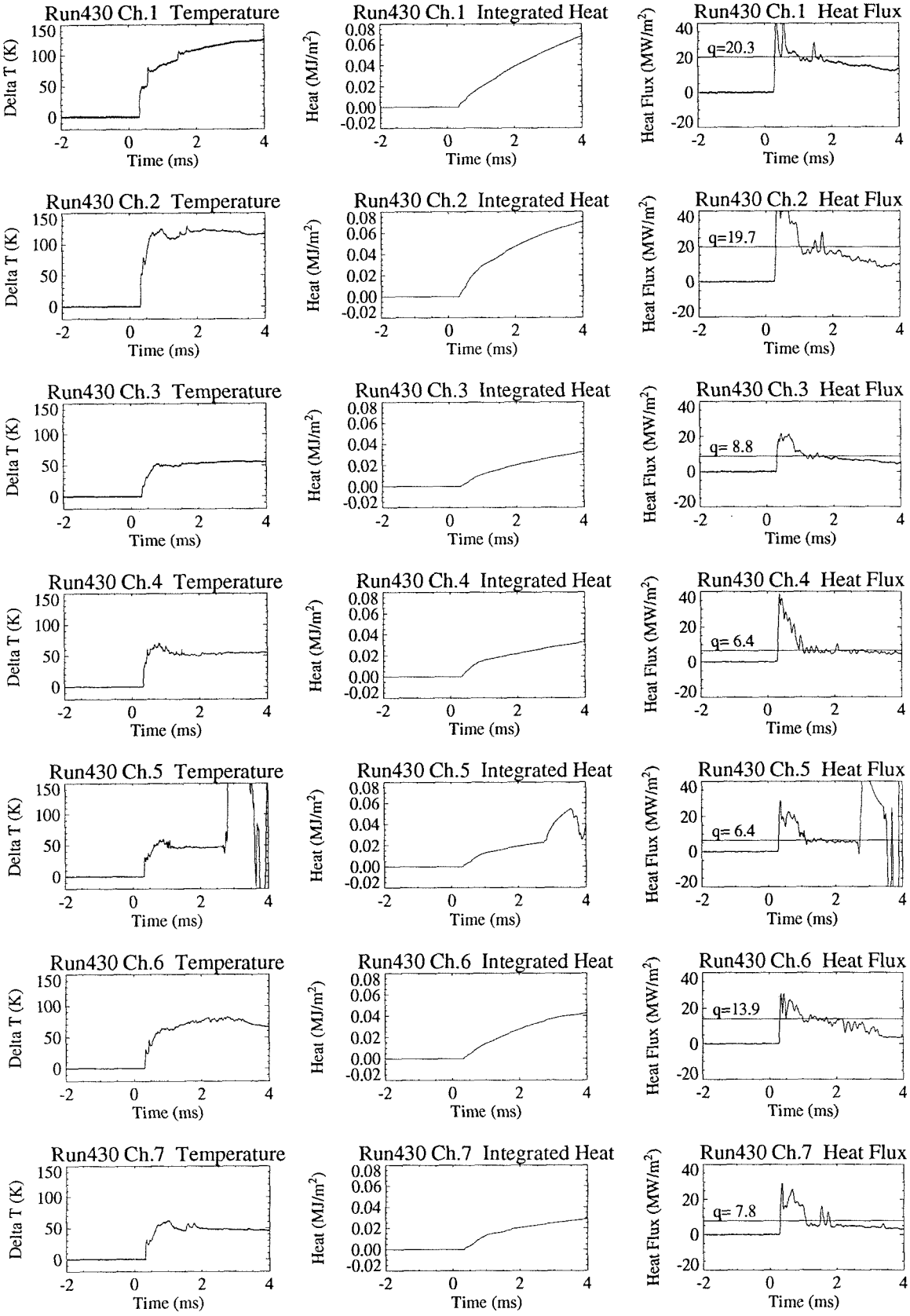

Fig. 5.28. Heat Flux Measurement Result in Carbon Dioxide (Run430)

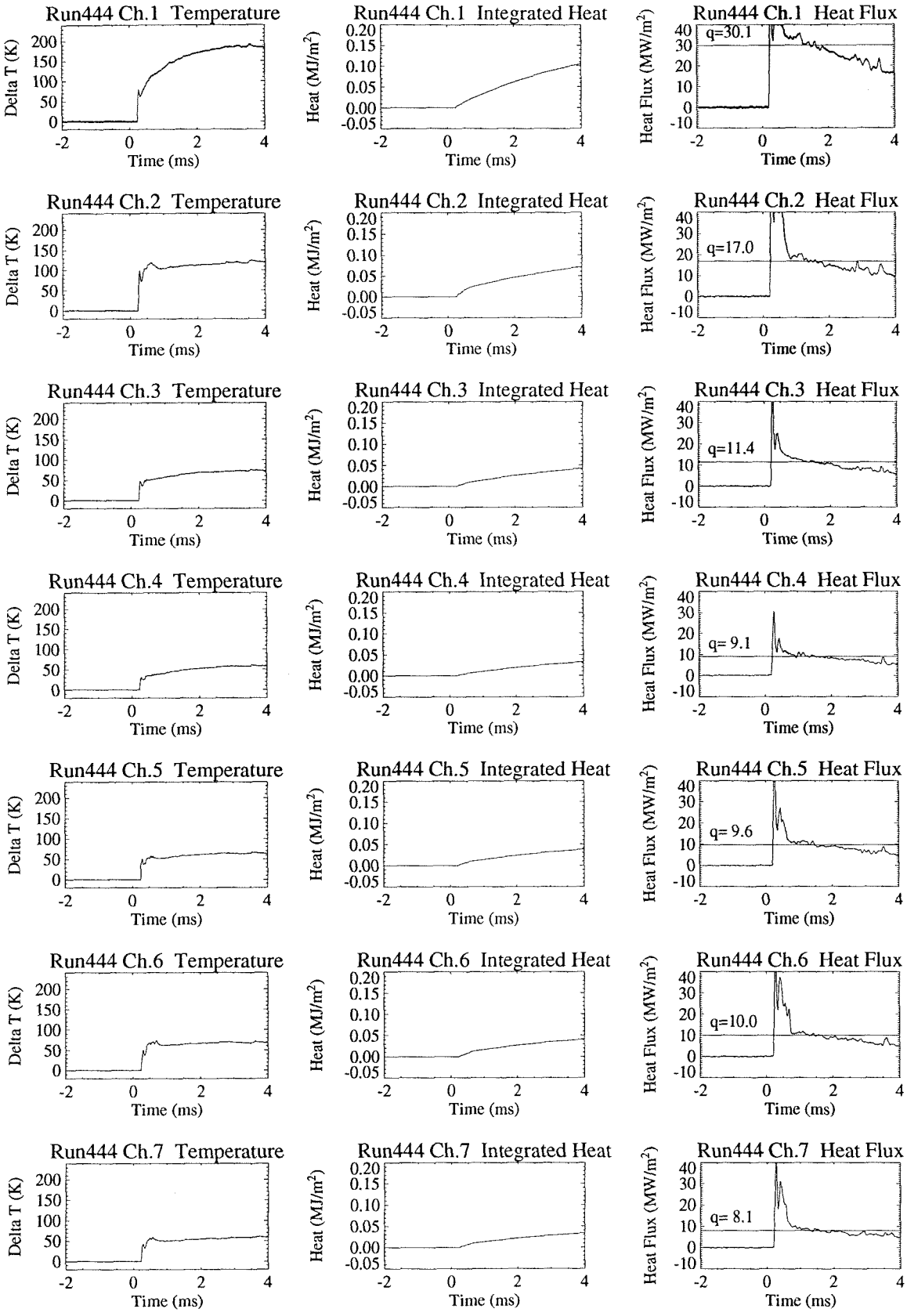

Fig. 5.29. Heat Flux Measurement Result in Carbon Dioxide (Run444)

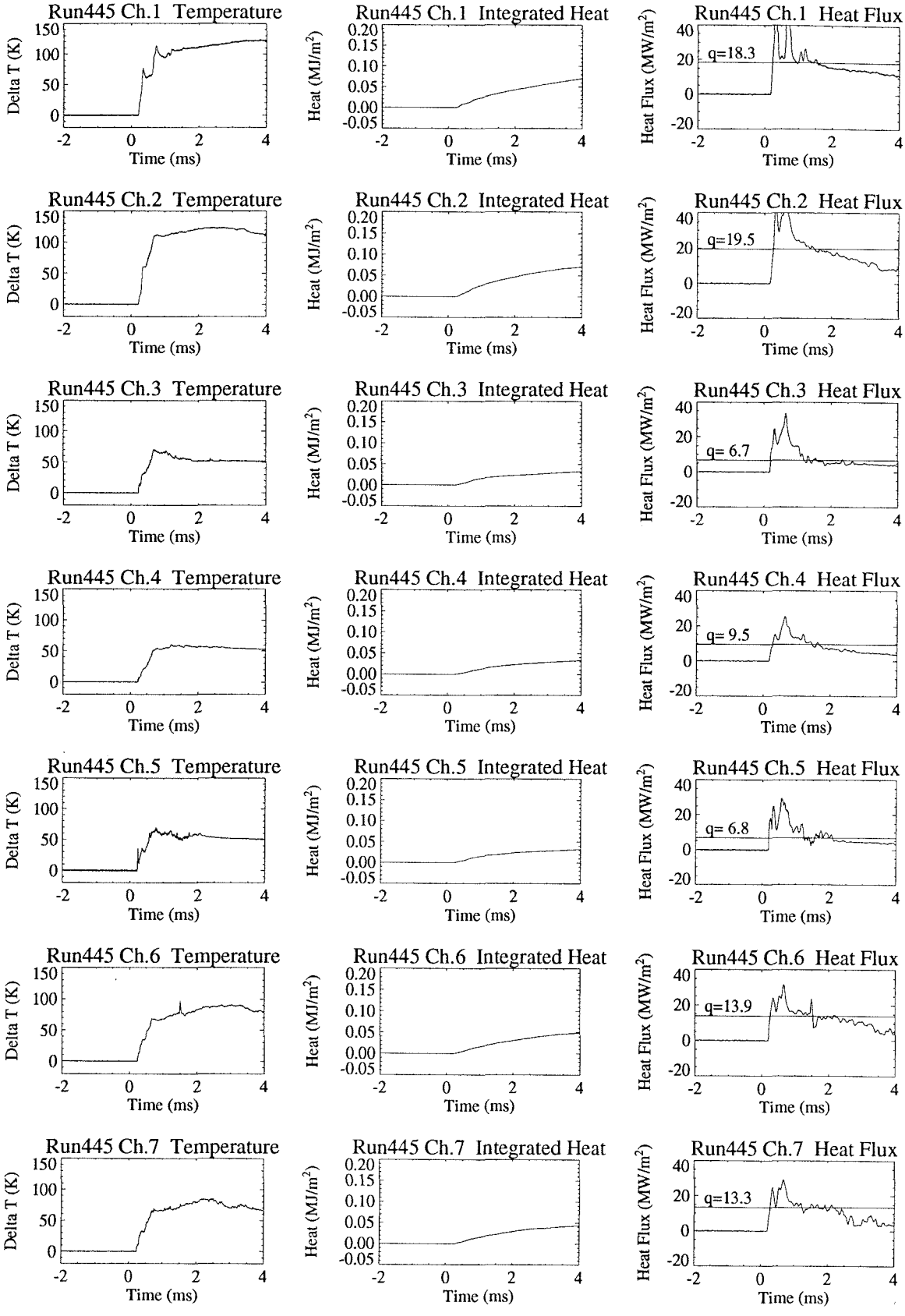

Fig. 5.30. Heat Flux Measurement Result in Carbon Dioxide (Run445)

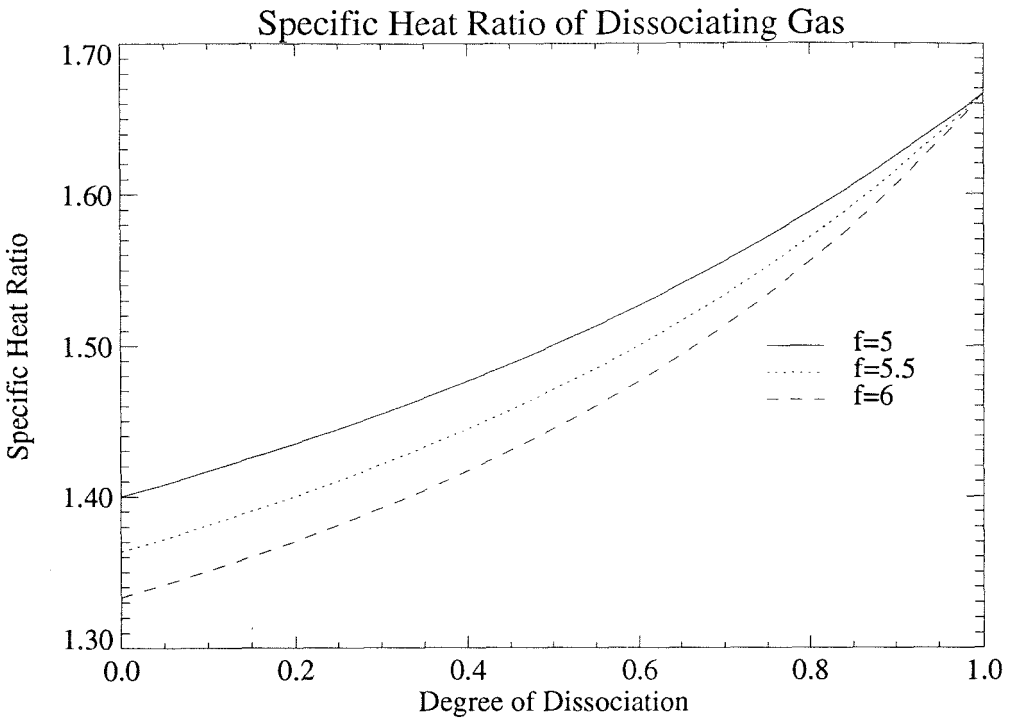

Fig. 5.31. Specific Ratio of Dissociating Gas

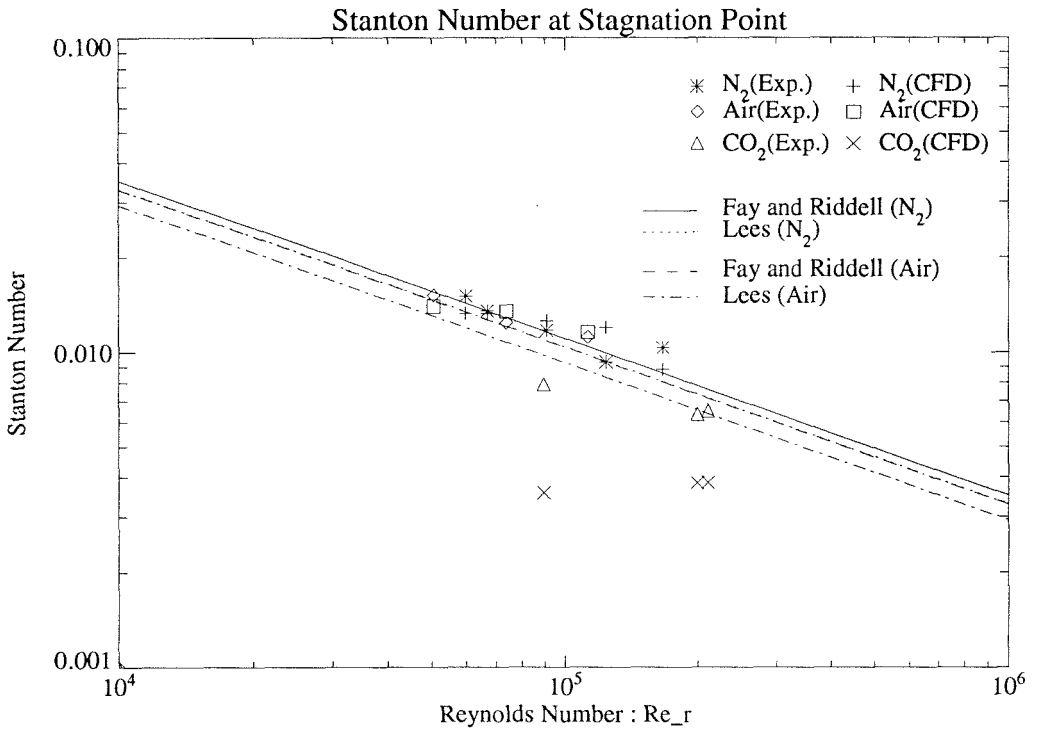

Fig. 5.32. Stagnation Point Heat Flux in Dimensionless Form

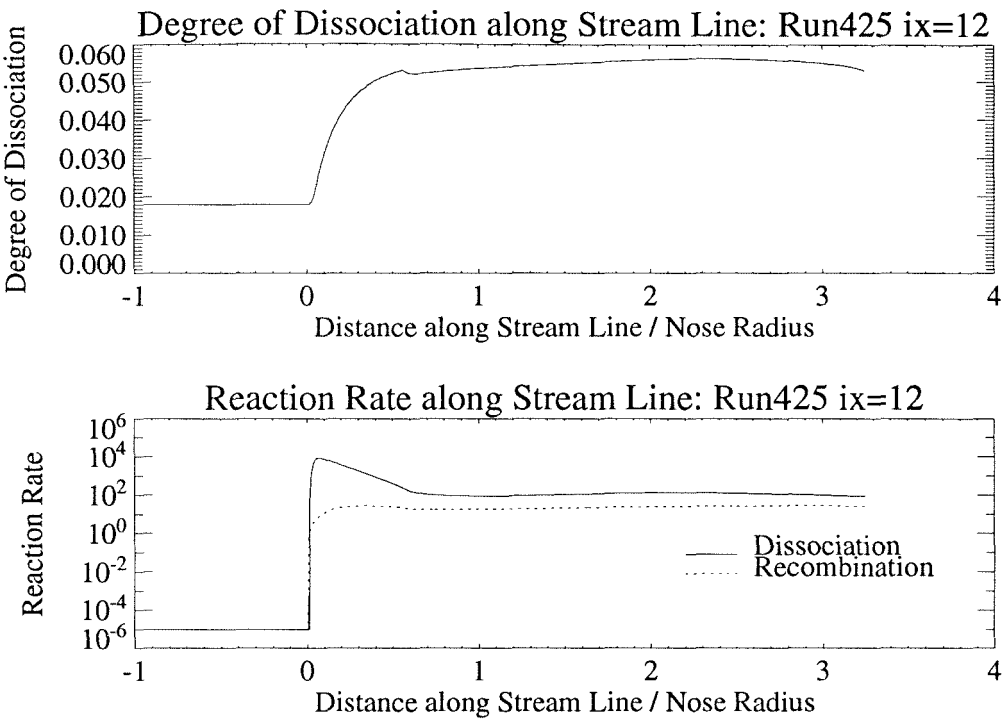

Fig. 5.33. Reaction Rate along Streamline (Run425,ix=12)

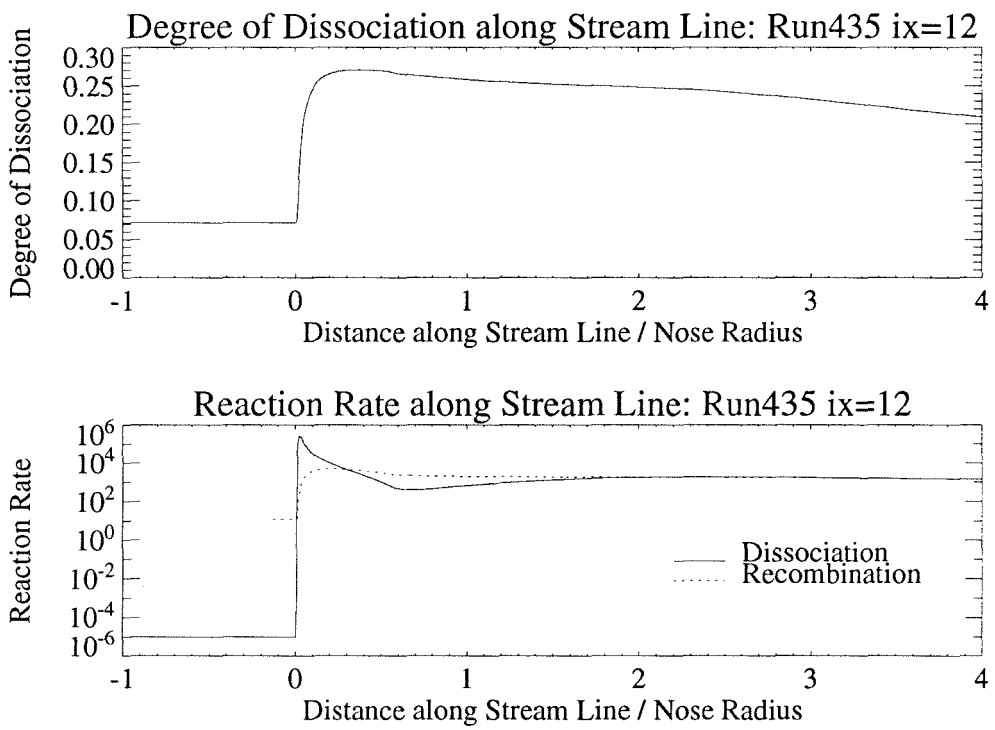

Fig. 5.34. Reaction Rate along Streamline (Run435,ix=12)

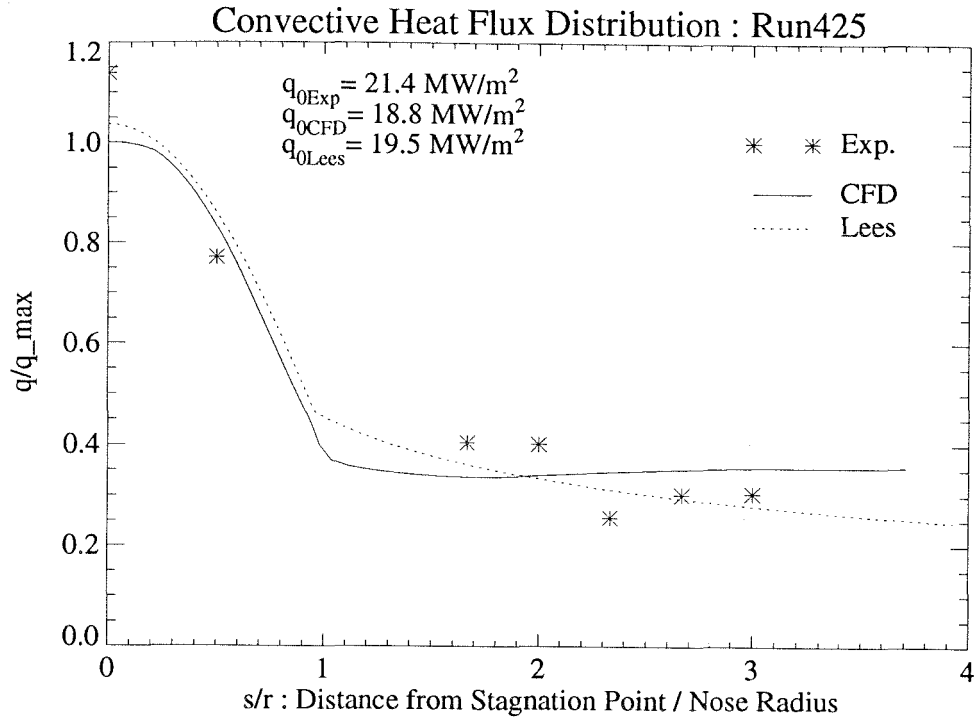

Fig. 5.35. Heat Flux Distribution (Run425)

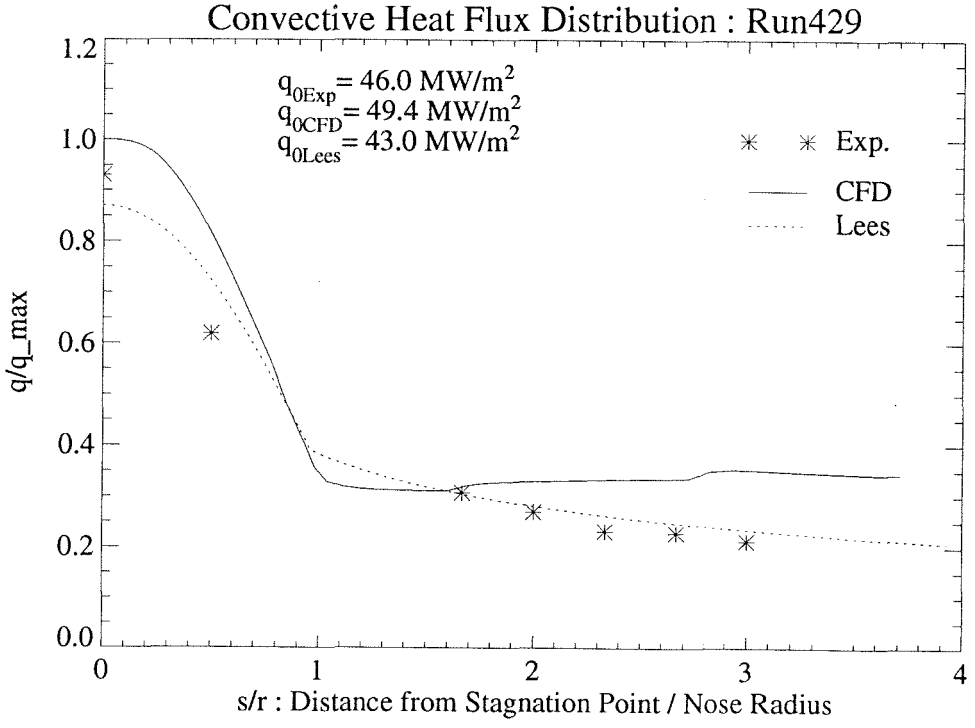

Fig. 5.36. Heat Flux Distribution (Run429

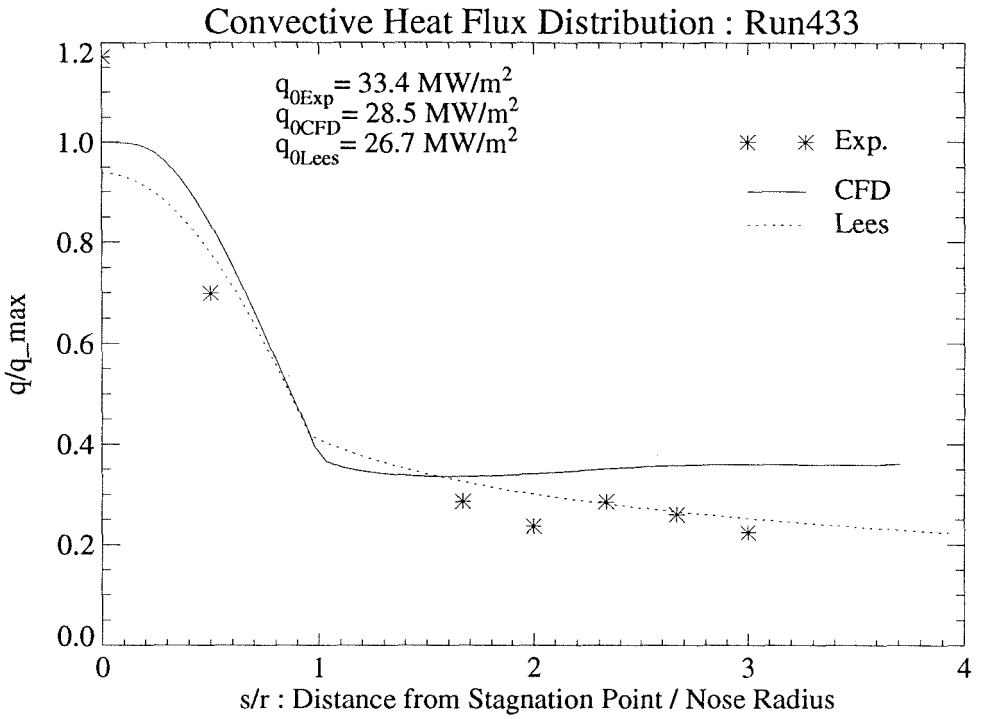

Fig. 5.37. Heat Flux Distribution (Run433)

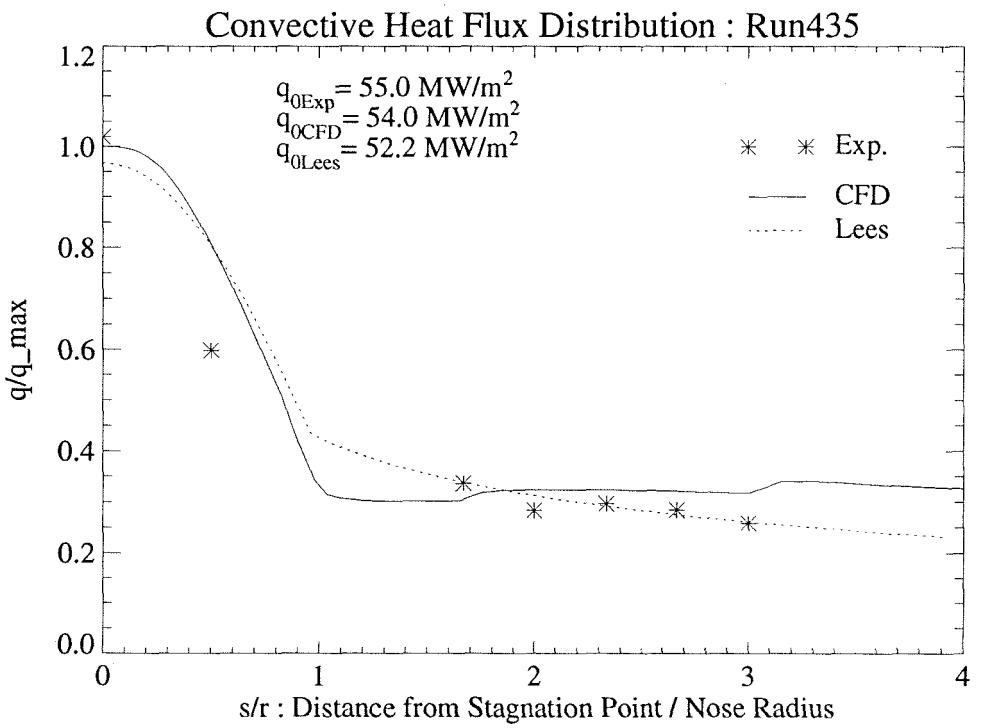

Fig. 5.38. Heat Flux Distribution (Run435)

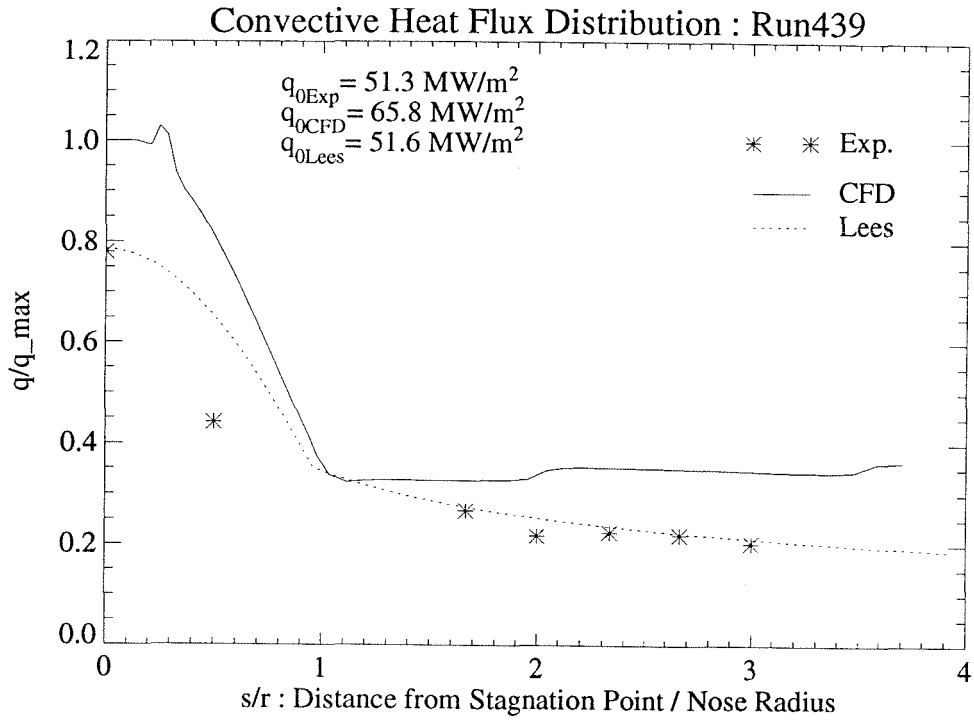

Fig. 5.39. Heat Flux Distribution (Run439)

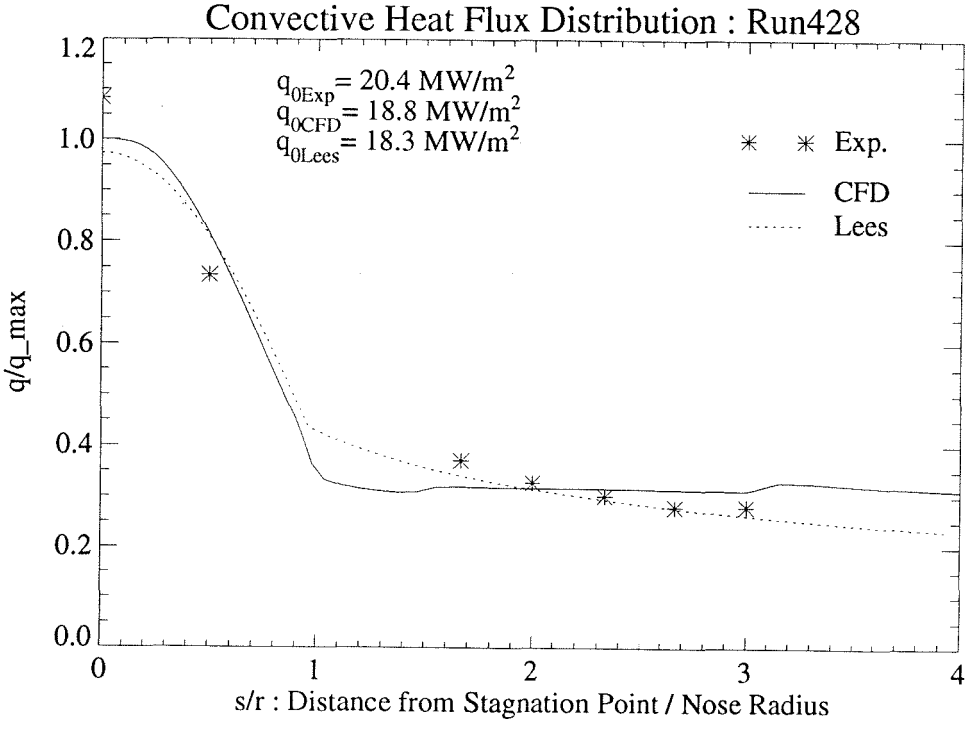

Fig. 5.40. Heat Flux Distribution (Run428)

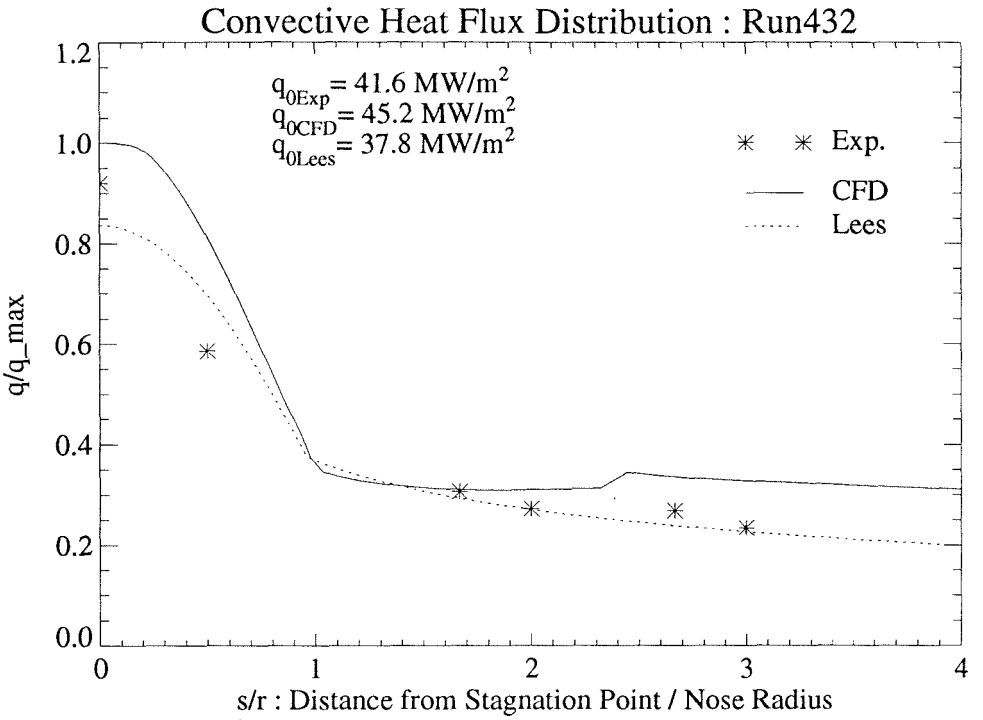

Fig. 5.41. Heat Flux Distribution (Run432)

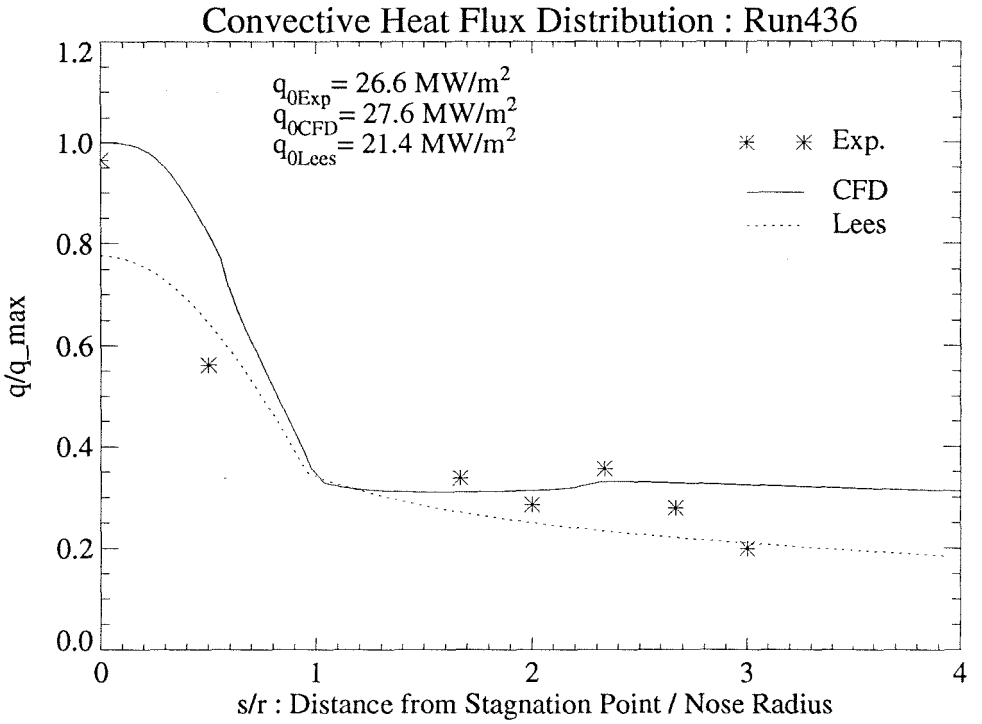

Fig. 5.42. Heat Flux Distribution (Run436)

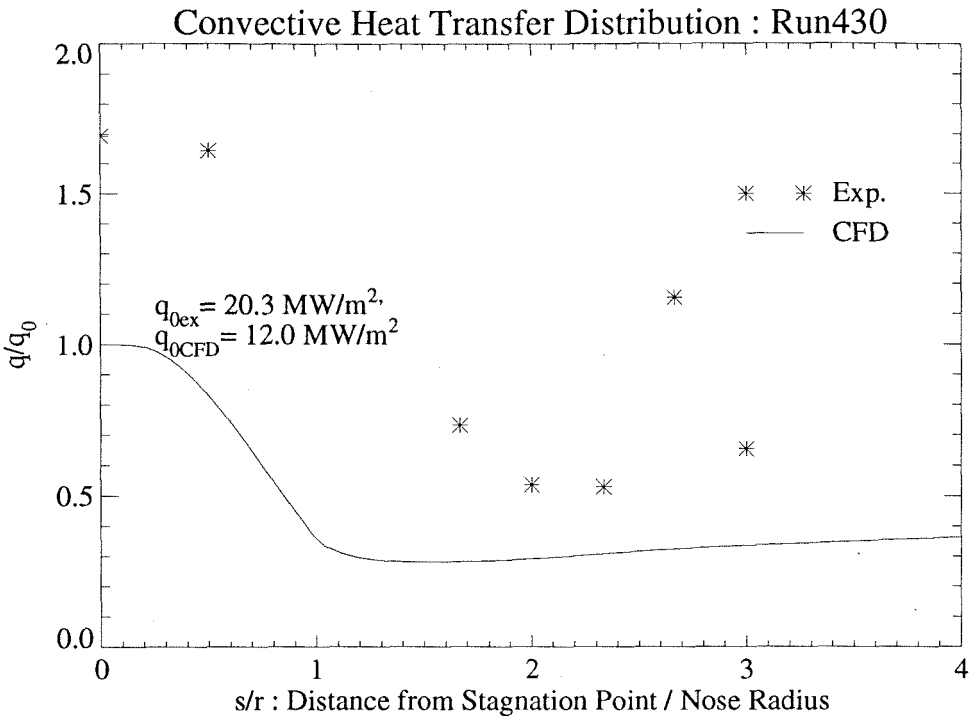

Fig. 5.43. Heat Flux Distribution (Run430)

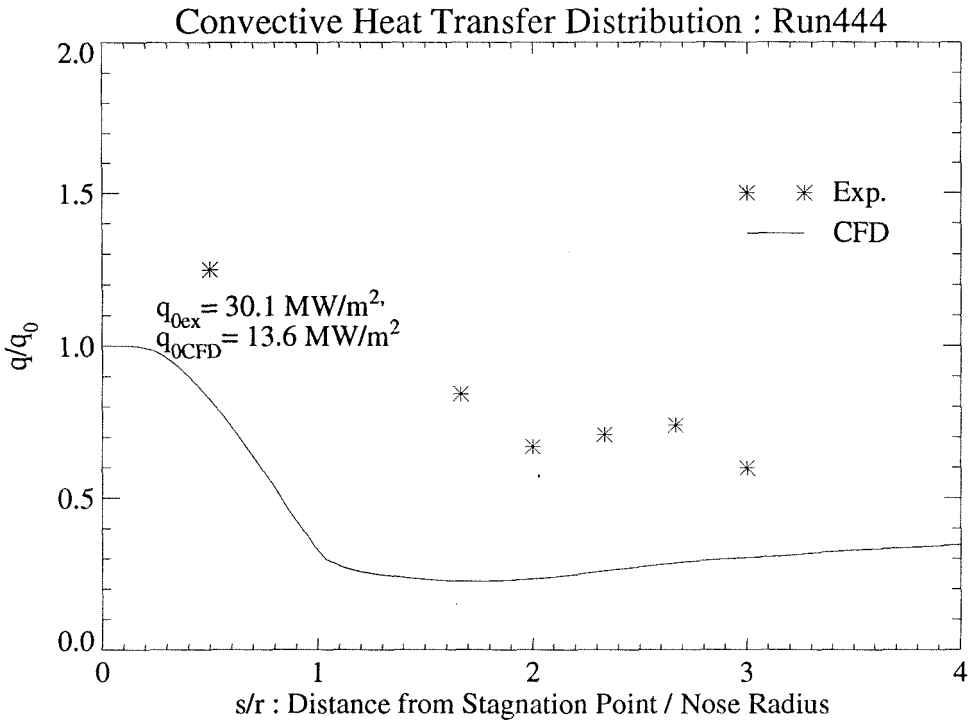

Fig. 5.44. Heat Flux Distribution (Run444)

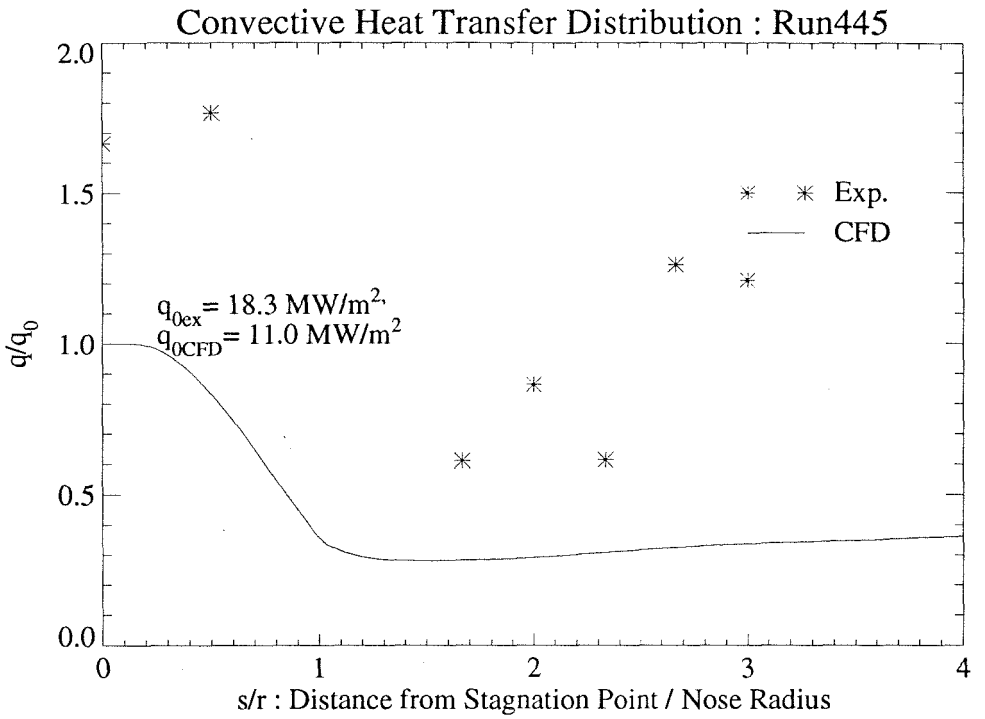

Fig. 5.45. Heat Flux Distribution (Run445)

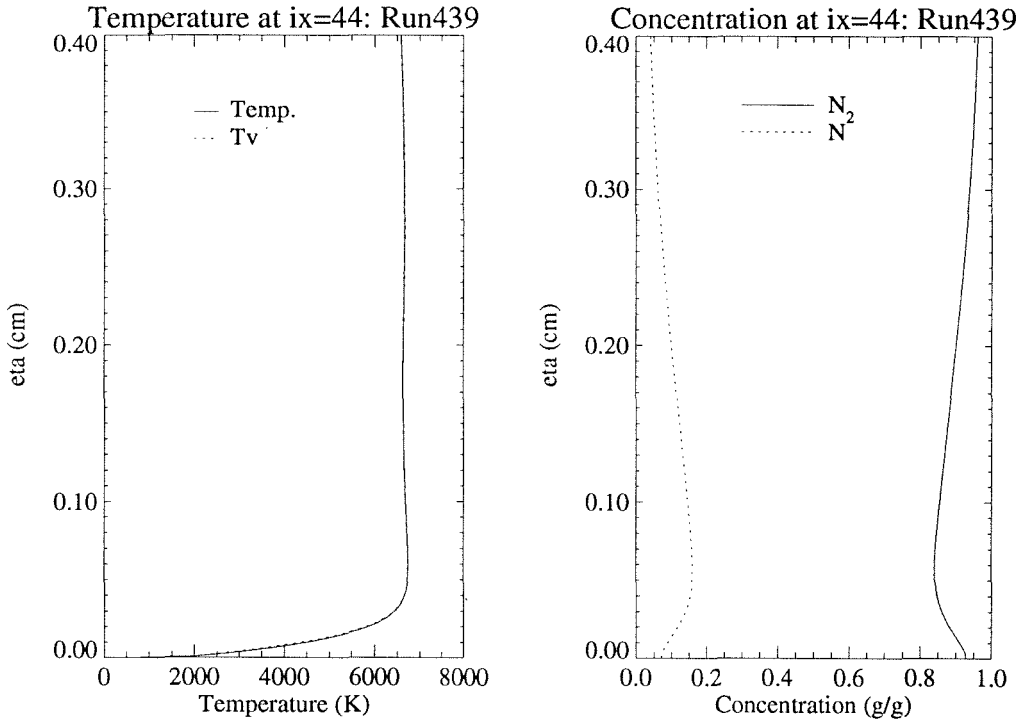

Fig. 5.46. Temperature and Concentration Profile Normal to Surface (Run439)

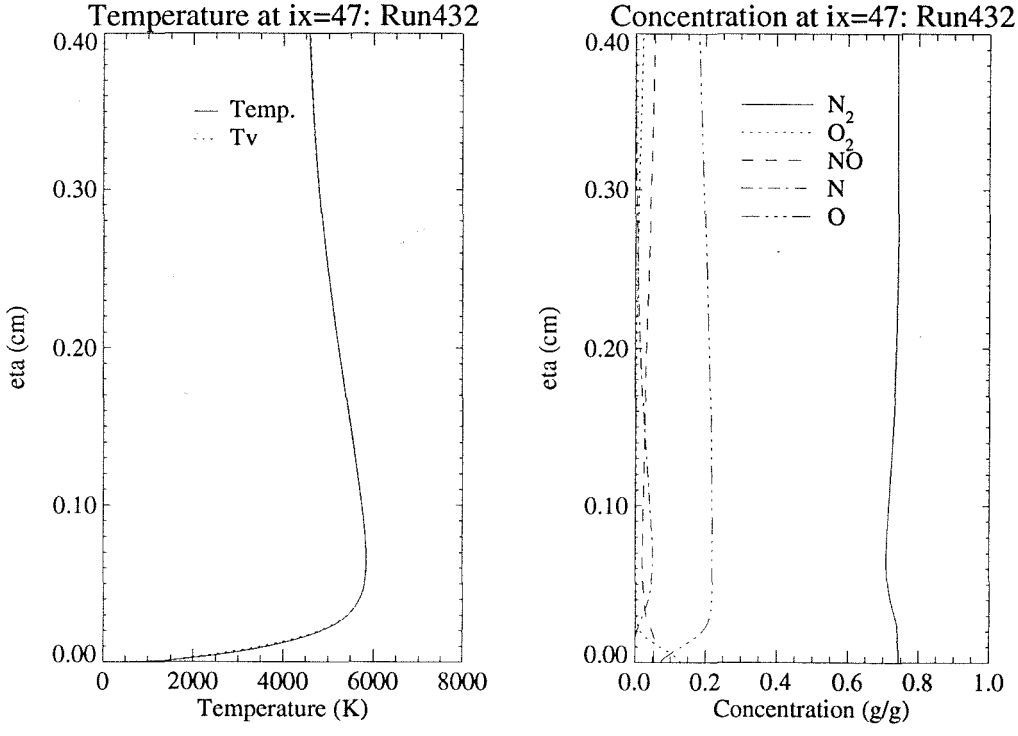

Fig. 5.47. Temperature and Concentration Profile Normal to Surface (Run432)

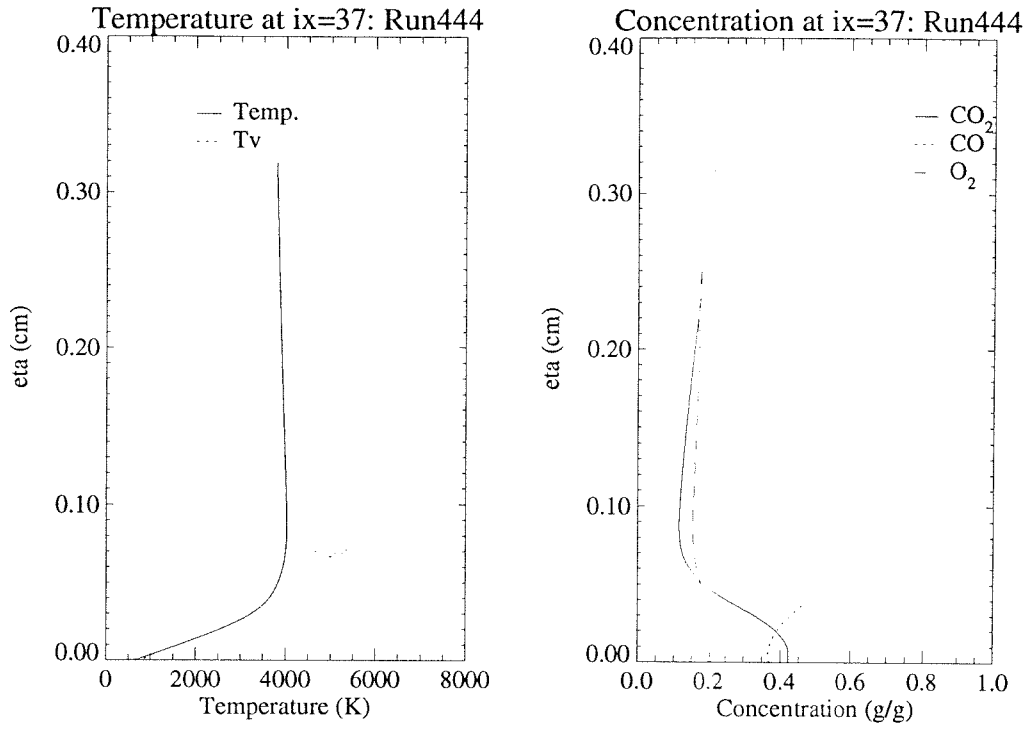

Fig. 5.48. Temperature and Concentration Profile Normal to Surface (Run444)

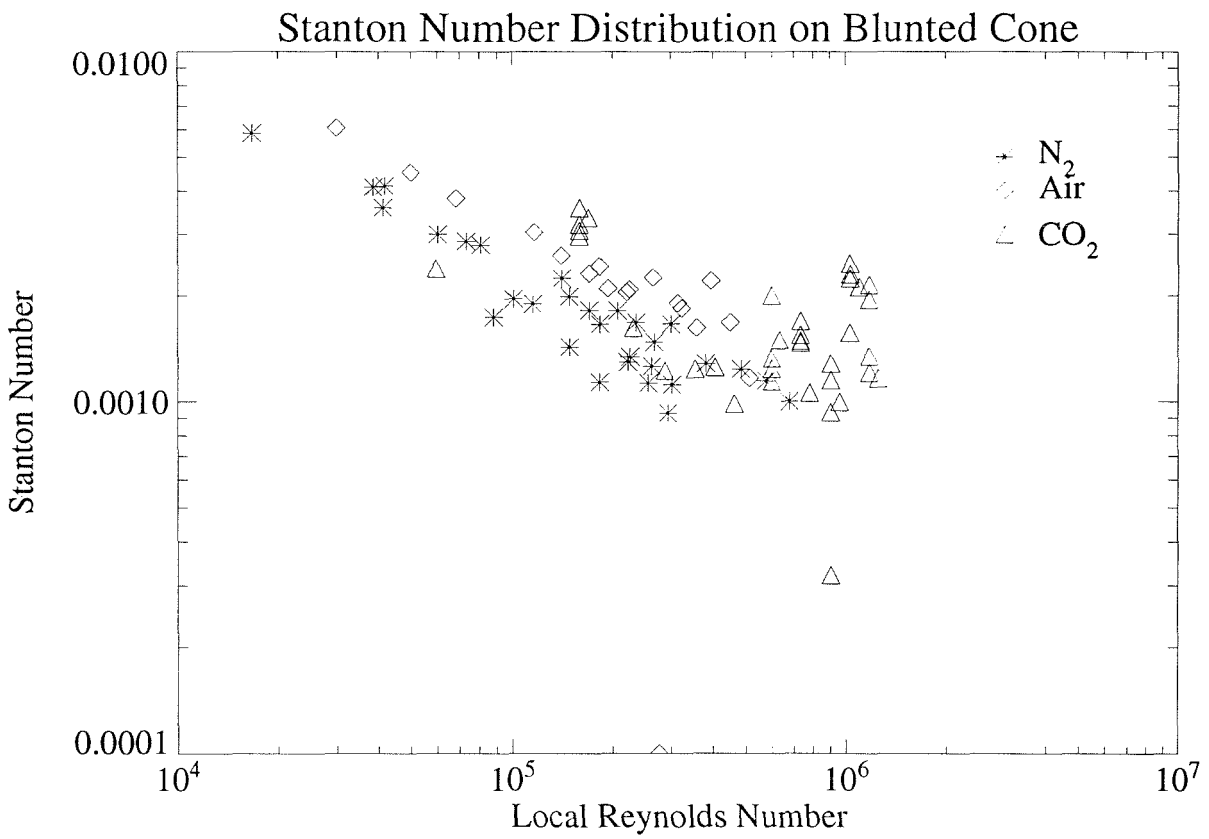

Fig. 5.49. After Body Heat Flux in Dimensionless Form

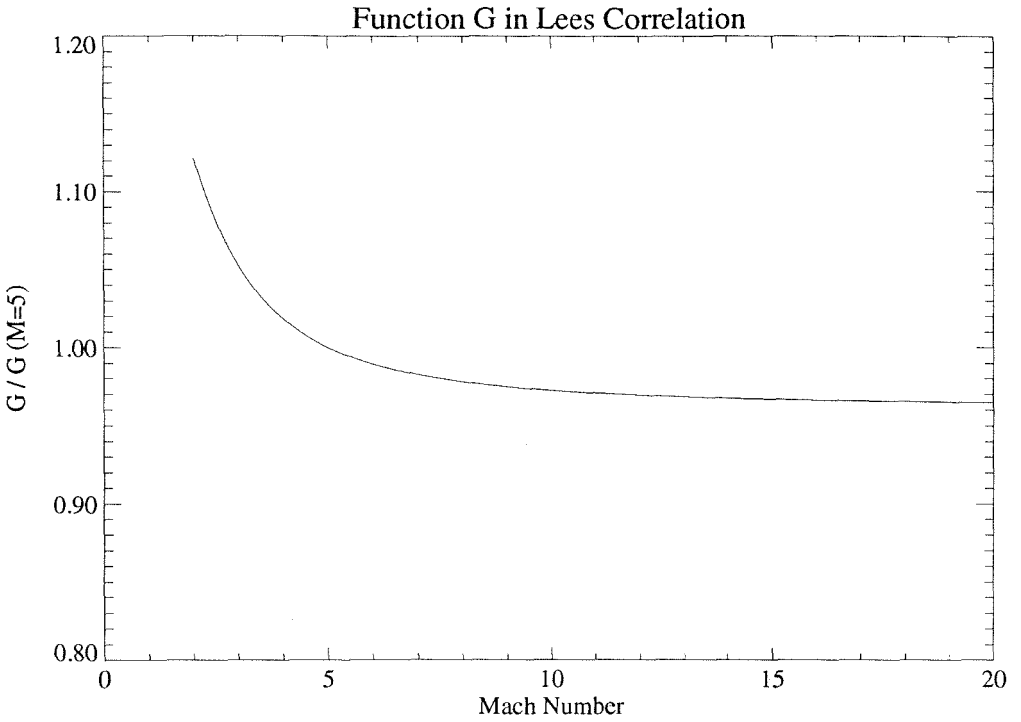

Fig. 5.50. Variation of G with Constant Effective Specific Heat Ratio

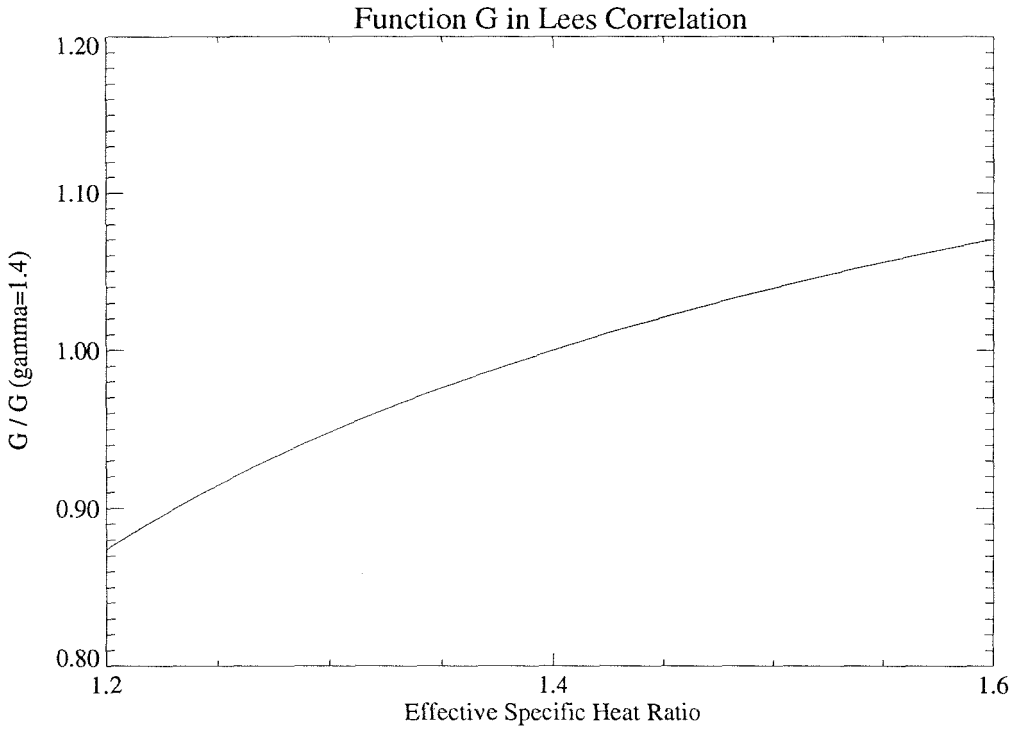

Fig. 5.51. Variation of G with Constant Free Stream Mach Number

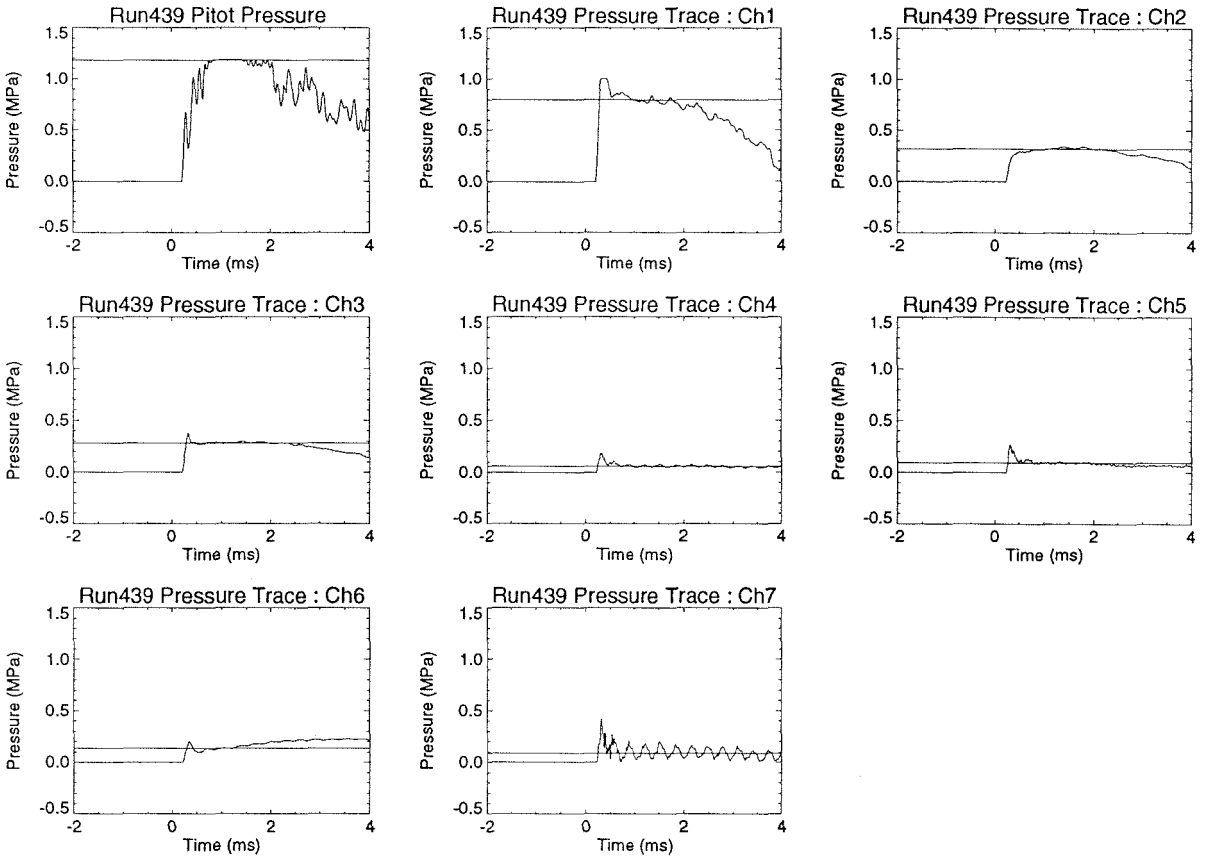

Fig. 5.52. Example of Output of Pressure Transducer

APPENDIX A
DRAWINGS

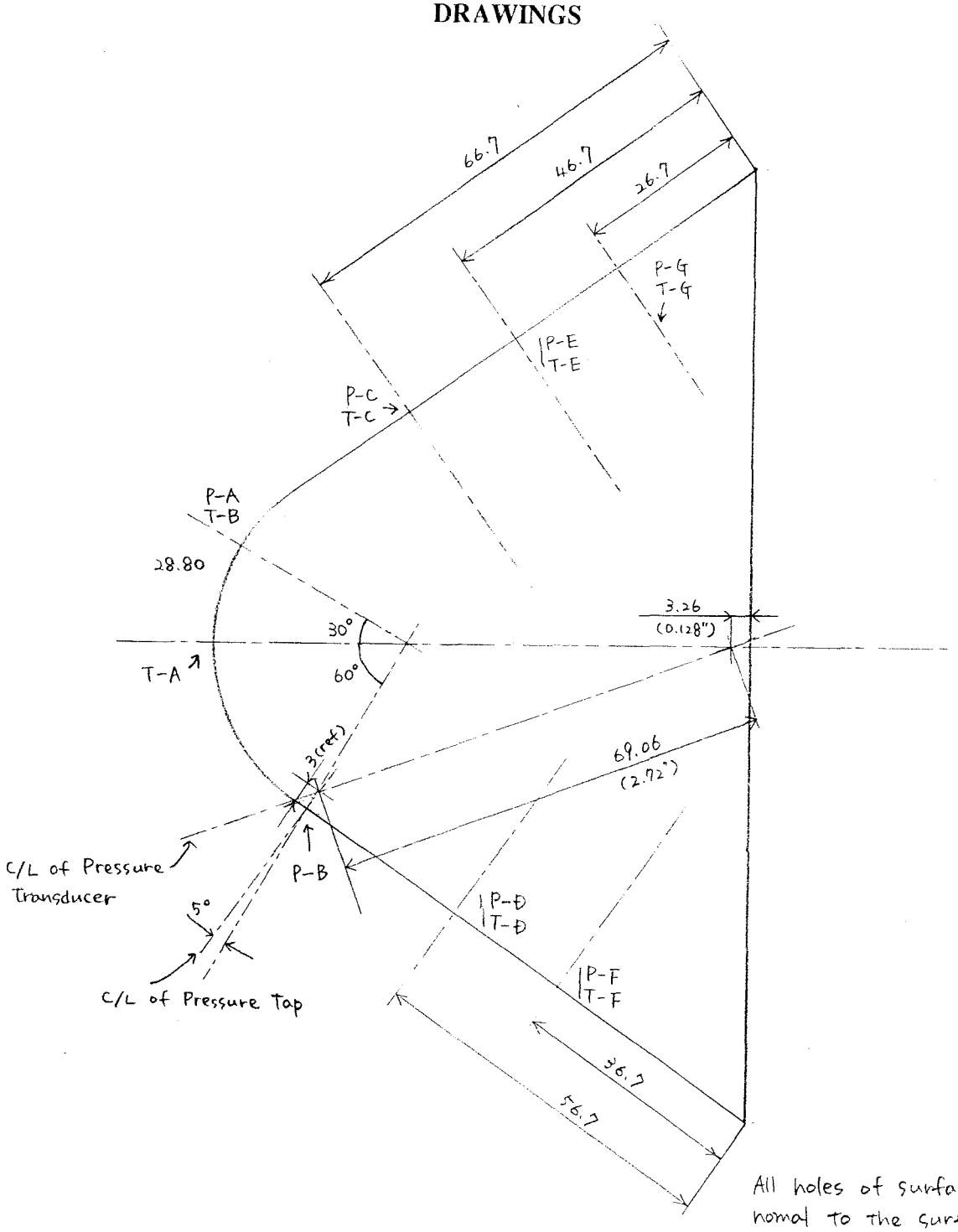

All holes of surface is nomal to the surface.

1/1 Model
Location of Transducers

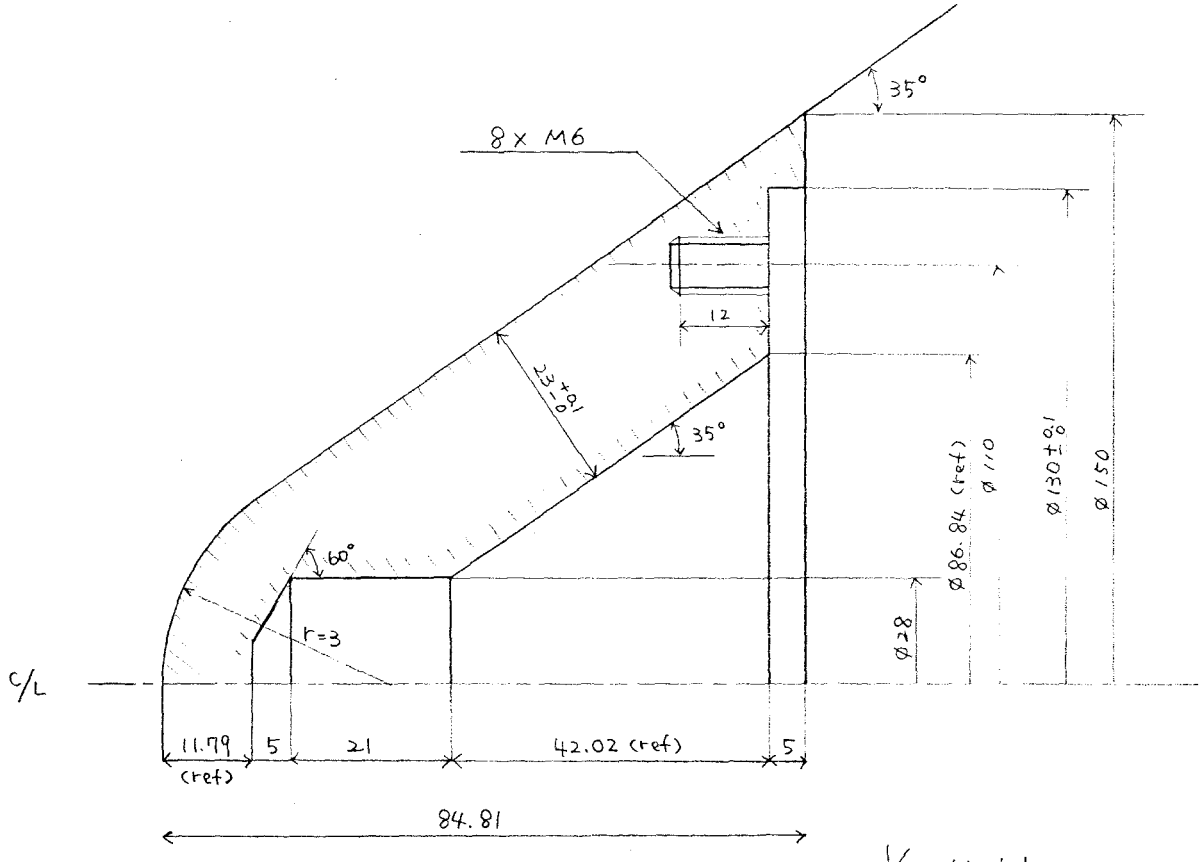

1/1 Model Cross Section

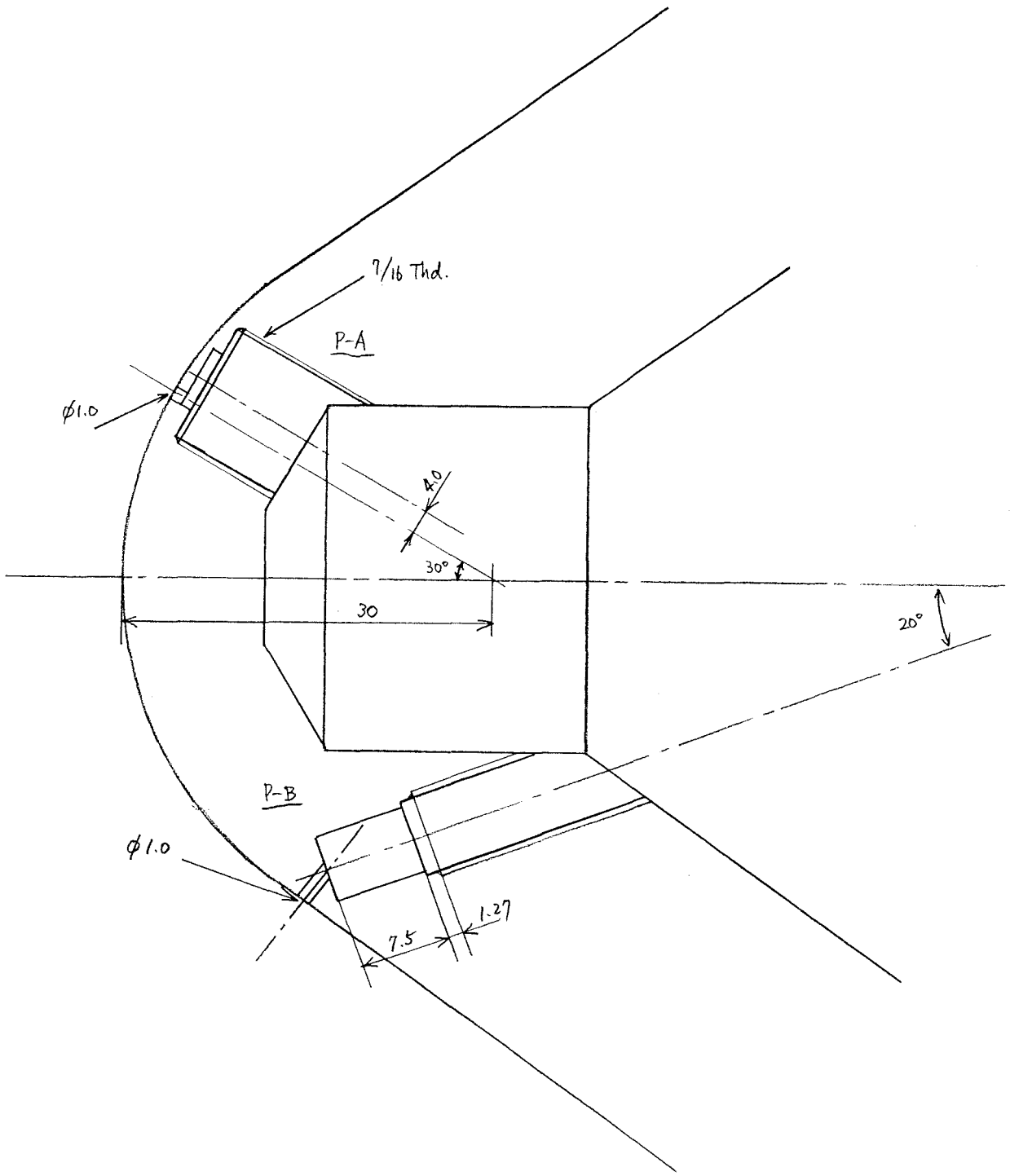

Port P-A & P-B

Scale 2/1

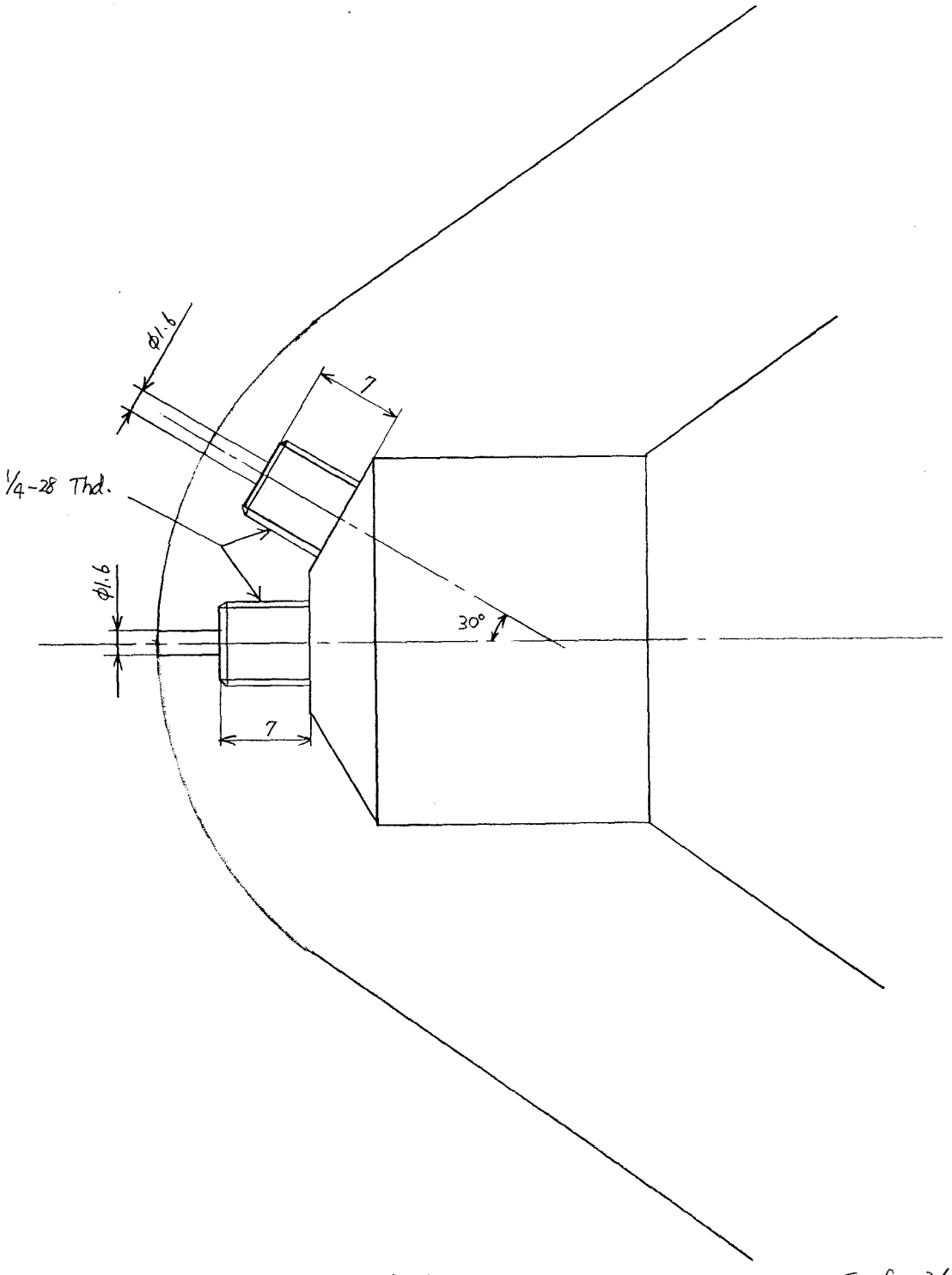

Port T-A & T-B

Scale 2/1

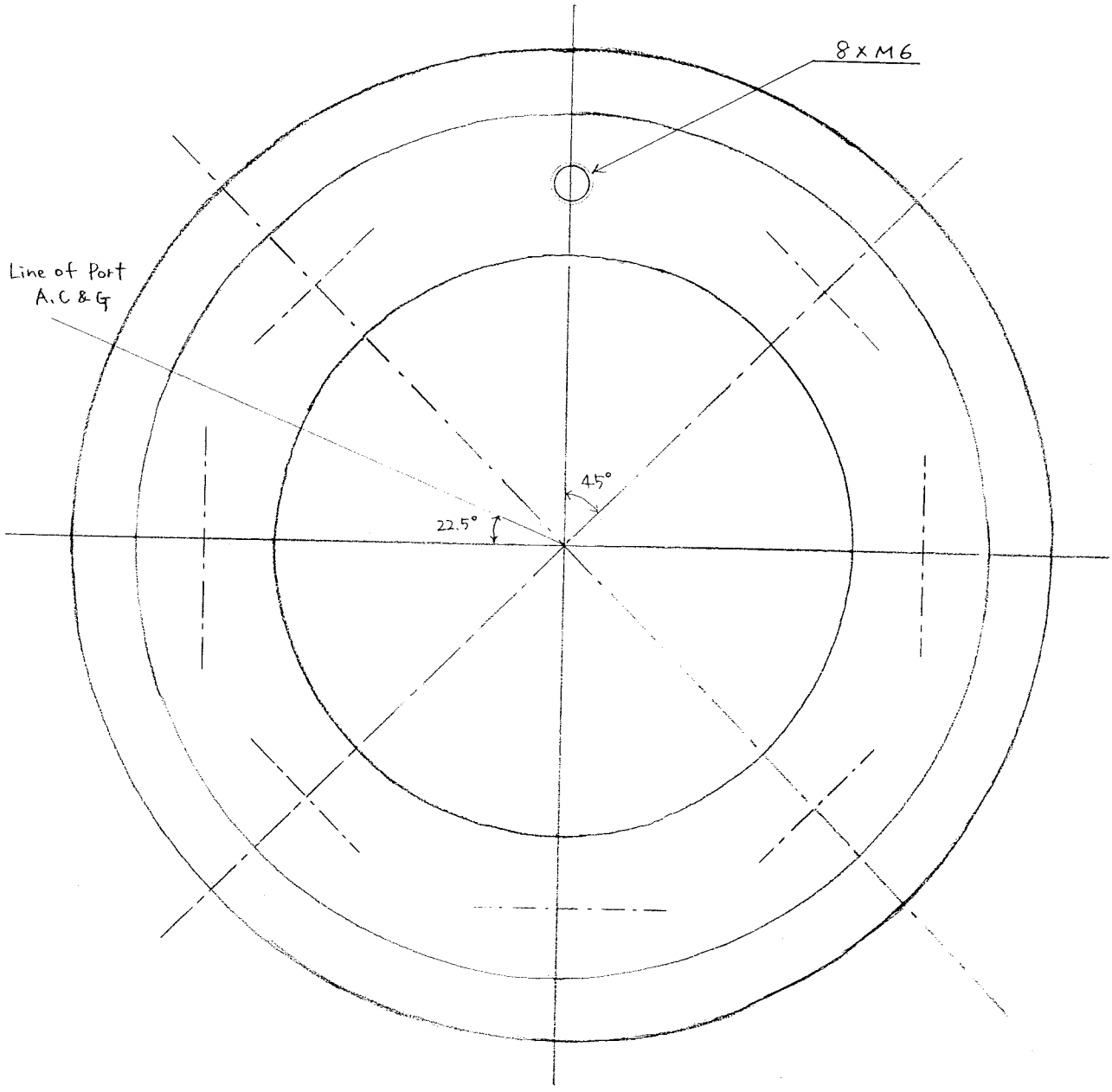

1/1 Model Bottom View

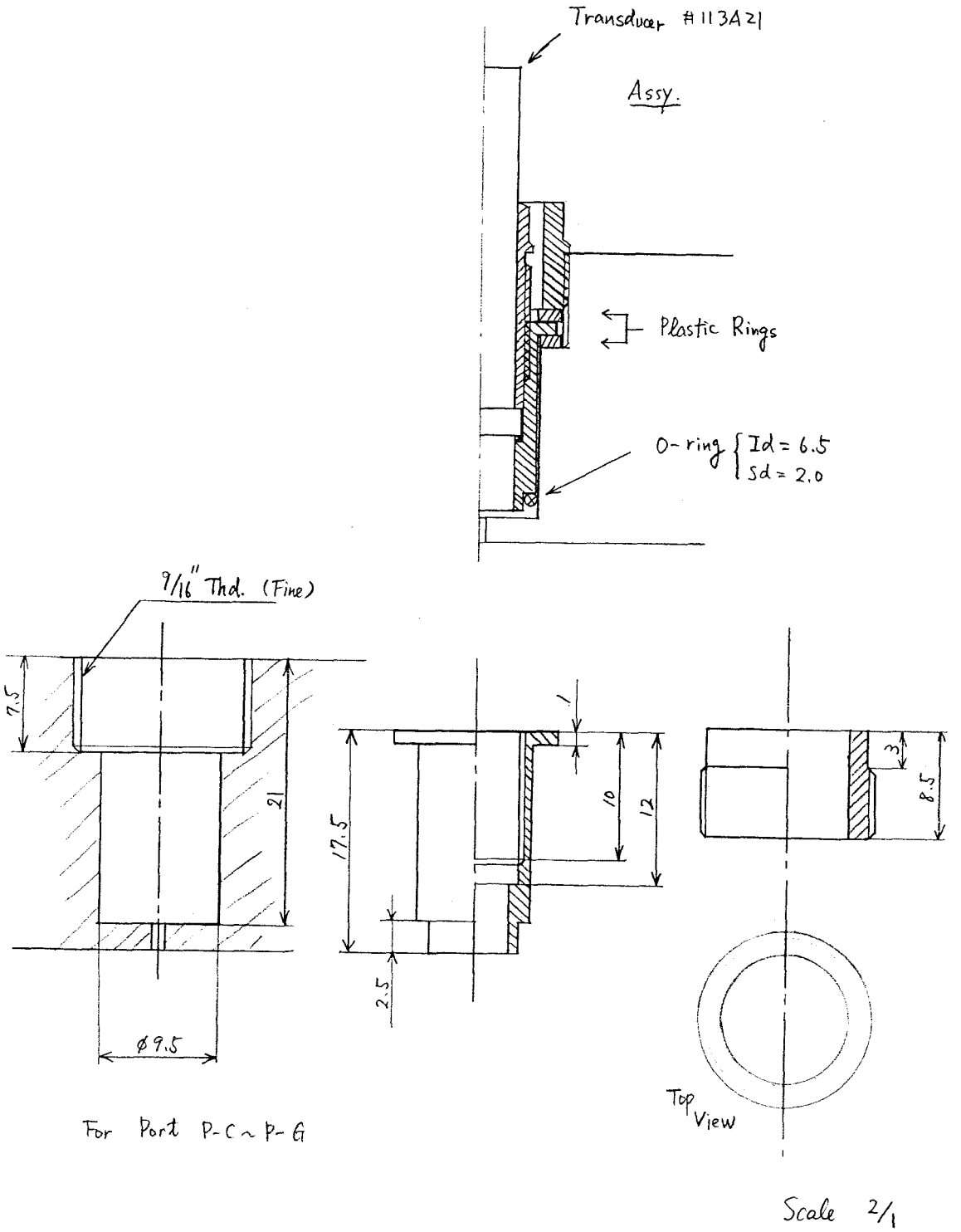
Transducer #113A21
Assy.
Plastic Rings
O-ring { Id = 6.5
Sd = 2.0
9/16" Thd. (Fine)
7.5
21
ø9.5
17.5
1
10
12
2.5
3
8.5
Top View
For Port P-C ~ P-G
Scale 2/1

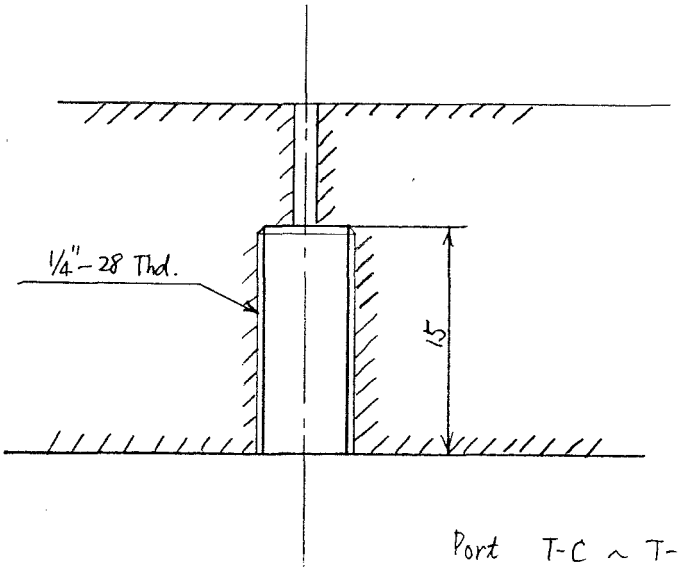

Port T-C ~ T-G

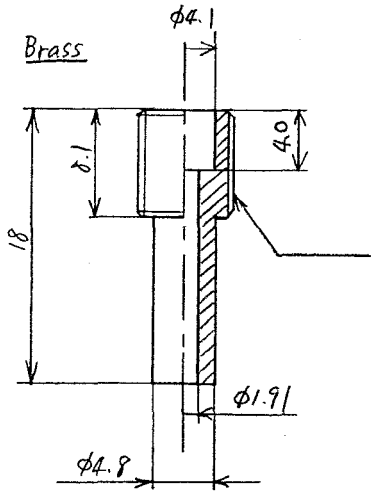

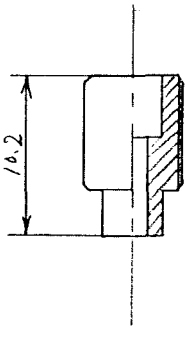

All Other Dimensions are Same.

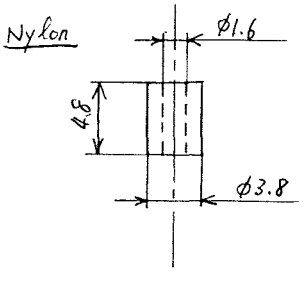

Appendix B
The Constants Used in Computation

Table B.1 Heat of Formation and Characteristic Temperature

(1) Nitrogen

Species	h_{0s} (J/kg)	θ_{vs} (K)
N_2	0.0	3395.0
N	2.996123×10^6	0.0

(2) Air

Species	h_{0s} (J/kg)	θ_{vs} (K)
N_2	0.0	3395.0
O_2	0.0	2239.0
NO	2.996123×10^6	2817.0
N	3.362161×10^7	0.0
O	1.543119×10^7	0.0

(3) CO_2

Species	h_{0s} (J/kg)	θ_{vs} (K)
CO_2	-8.924350×10^6	1903.0 945.0 945.0
CO	-4.062926×10^6	3074.0
O_2	0.0	2239.0
C	5.907274×10^7	0.0
O	1.543119×10^7	0.0

The forward reaction rate coeffecient is calculated by following equation with the constants summarized in following tables.

$$k_{fs} = C_{fs} T^{\eta_s} \exp\left(\frac{\theta_s}{T}\right) \qquad \text{(B.1)}$$

Table B.2 Arrehenius Coefficients for Forward Reactions

(1) Nitrogen

Reaction	Partner	C_{fs} (m^3/kg s)	η_s	θ_s (K)
(4.9)	N_2	3.70×10^{18}	-1.6	113200
	N	1.66×10^{19}	-1.6	113200

(2) Air

Reaction	Partner	C_{fs} (m^3/kg s)	η_s	θ_s (K)
(4.10-1)	N_2	3.70×10^{18}	-1.6	113200
	O_2	3.70×10^{18}	-1.6	113200
	NO	3.70×10^{18}	-1.6	113200
	N	3.70×10^{18}	-1.6	113200
	O	3.70×10^{18}	-1.6	113200
(4.10-2)	N_2	2.75×10^{16}	-1.0	59500
	O_2	2.75×10^{16}	-1.0	59500
	NO	2.75×10^{16}	-1.0	59500
	N	8.25×10^{16}	-1.0	59500
	O	8.25×10^{16}	-1.0	59500
(4.10-3)	N_2	2.30×10^{14}	-0.5	75500
	O_2	2.30×10^{14}	-0.5	75500
	NO	2.30×10^{14}	-0.5	75500
	N	4.60×10^{14}	-0.5	75500
	O	4.60×10^{14}	-0.5	75500
(4.10-4)	-	3.18×10^{10}	0.10	37700
(4.10-5)	-	2.16×10^{5}	1.29	19220

(3) Carbon Dioxide

Reaction	Partner	C_{fs} (m^3/kg s)	η_s	θ_s (K)
(4.11-1)	CO_2	6.90×10^{18}	-1.5	63275
	CO	6.90×10^{18}	-1.5	63275
	O_2	6.90×10^{18}	-1.5	63275
	C	1.40×10^{19}	-1.5	63275
	O	1.40×10^{19}	-1.5	63275
(4.11-2)	CO_2	2.30×10^{16}	-1.0	129000
	CO	2.30×10^{16}	-1.0	129000
	O_2	2.30×10^{16}	-1.0	129000
	C	2.30×10^{16}	-1.0	129000
	O	2.30×10^{16}	-1.0	129000
(4.11-3)	CO_2	2.00×10^{18}	-0.5	59750
	CO	2.00×10^{18}	-0.5	59750
	O_2	2.00×10^{18}	-0.5	59750
	C	1.00×10^{19}	-0.5	59750
	O	1.00×10^{19}	-0.5	59750
(4.11-4)	-	3.90×10^{10}	-0.18	69200
(4.11-5)	-	2.10×10^{10}	0.0	27800

The equilibrium reaction constant $K_{eq\,s}$ is evaluated by the flollowing equation.

$$K_{eqs} = \exp\left(C_{s1} + C_{s2}Z + C_{s3}Z^2 + C_{s4}Z^3 + C_{s5}Z^4\right) \qquad \text{(B.2)}$$

where

Z=10000/T, (T in Kelvin).

Table B.3 Coefficients of the Equation of Equilibrium Reaction Constants

(1) Nitrogen

Reaction	C_{s1}	C_{s2}	C_{s3}	C_{s4}	C_{s5}
(4.9)	3.898	-12.611	0.683	-0.118	0.006

(2) Air

Reaction	C_{s1}	C_{s2}	C_{s3}	C_{s4}	C_{s5}
(4.10-1)	3.898	-12.611	0.683	-0.118	0.006
(4.10-2)	1.335	-4.127	-0.616	0.093	-0.005
(4.10-3)	1.549	-7.784	0.228	-0.043	0.002
(4.10-4)	2.349	-4.828	0.455	-0.075	0.004
(4.10-5)	0.215	-3.652	0.843	-0.136	0.007

(3) Carbon Dioxide

Reaction	C_{s1}	C_{s2}	C_{s3}	C_{s4}	C_{s5}
(4.11-1)	3.172	-0.174	-5.058	-0.187	0.009
(4.11-2)	4.366	1.157	-13.829	0.116	-0.006
(4.11-3)	2.289	0.469	-5.734	-0.056	0.003
(4.11-4)	2.077	0.687	-8.094	0.172	-0.009
(4.11-5)	0.884	-0.643	0.676	-0.132	0.006

Table B.4 Coefficients for Blottner's Viscosity Model

(1) Nitrogen

Species	A_s	B_s	C_s
N_2	0.0268142	0.3177838	-11.3155513
N	0.0115572	0.6031679	-12.4327495

(2) Air

Species	A_s	B_s	C_s
N_2	0.0268142	0.3177838	-11.3155513
O_2	0.044929	-0.0826158	-9.2019475
NO	0.0436378	-0.0335511	-9.5767430

N	0.0115572	0.6031679	-12.4327495
O	0.0203144	0.4294404	-11.6031403

(3) Carbon Dioxide

Species	A_s	B_s	C_s
CO_2	-0.019527387	1.047818	-14.32212
CO	-0.019527394	1.013295	-13.97873
O_2	0.044929	-0.0826158	-9.2019475
C	-0.0115572	0.6031679	-12.4327495
O	0.0203144	0.4294404	-11.6031403

Table B.5 summarizes the value of the Gladstone-Dale constants for the chemical species considered in the computations. These values are taken from Merzkirch (1974), Alpher et al. (1959) and Kaye and Laby (1986).

Table B.5. Gladstone-Dale Constants

Species	κ_s (m^3/kg)
N_2	0.241×10^{-3}
O_2	0.190×10^{-3}
NO	0.246×10^{-3}
N	0.310×10^{-3}
O	0.182×10^{-3}
CO_2	0.230×10^{-3}
CO	0.270×10^{-3}
C	0.404×10^{-3}